

FIRST PRINCIPLES COMPUTATIONAL MODELING OF THE SURFACE  
PROPERTIES OF URANIUM DIOXIDE

by

MEGAN HOOVER

Presented to the Faculty of the Graduate School of  
The University of Texas at Arlington in Partial Fulfillment  
of the Requirements  
for the Degree of

MASTERS OF SCIENCE IN PHYSICS

THE UNIVERSITY OF TEXAS AT ARLINGTON

May 2014

Copyright © by Megan Hoover 2014

All Rights Reserved

## Acknowledgements

I would like to thank everyone who supported me throughout this thesis work. To Dr. Ray for giving me the opportunity to be a part of the Theoretical Condensed Matter Group and guiding me through my class work. Huge thanks to Dr. Raymond Atta-Fynn, I cannot put into words how thankful I am to have you in my corner. My appreciation to Dr. Qiming Zhang for stepping in and guiding me through the last semester. Thank you to the members of the Theoretical Condensed Matter group who gave advice and criticism to improve my project; namely Dr. Adhikari, Dr. Chen, Dr. Wang, Mrs. Hernandez El-Darazi, Mr. Wanaguru, Ms. Duesman, Mrs. Morrison-Sherrell, Mrs. Moten, and Ms. Sterrett. To my parents Steve and Jeannine Lee, for keeping my dog(s) on late nights and cooking me dinner several nights a week. Also your support and guidance through all my years of school. You two are the most loving parents; I am truly blessed to have you. To my brother Nick Lee for the nights of playing video games when I needed to take a break. Last but surely not least, my husband Bobby Hoover. These last two years apart from one another have been hard, but I cannot wait to be together again. I love you with all my heart and look forward to our future together.

April 16, 2014

## Abstract

# FIRST PRINCIPLES COMPUTATIONAL MODELING OF THE SURFACE PROPERTIES OF URANIUM DIOXIDE

Megan Hoover, MS

The University of Texas at Arlington, 2014

Supervising Professor: Qiming Zhang

The interaction of uranium dioxide ( $\text{UO}_2$ ) with environmental elements occurs at its exposed surface and a fundamental understanding of this interaction process begins at the atomic scale. In this regard, atomic scale modeling of the properties of clean and adsorbate-covered uranium dioxide ( $\text{UO}_2$ ) surfaces can be used to elucidate  $\text{UO}_2$  surface mechanisms such as corrosion and the formation of complex species via environmental gas adsorption. In this thesis, structural and electronic properties of clean and adsorbate-covered low index  $\text{UO}_2$  surfaces were modeled using regular and hybrid density functional theory. Specifically, the properties of the clean (111) and (110) surfaces were modeled with hybrid density functional theory. To gain some insight into the surface oxidation of  $\text{UO}_2$ , we performed preliminary modeling studies on the interaction of atomic oxygen with the  $\text{UO}_2$  (111) surface using density functional theory and hybrid density functional theory.

For the clean surface, the evolution of the work function, surface energy, incremental energy, and band gap with respect to the system size was studied. We observed that at five formula units and beyond the surface properties of  $\text{UO}_2$  converge. The estimated work function, surface energy, and band gap of the (111) surface were 3.5 eV,  $0.97 \text{ J/m}^2$ , and 1.2 eV respectively; the corresponding values for the (110) surface

were 2.2 eV, 1.76 J/m<sup>2</sup>, and 0.65 eV respectively. The localization of the 5f electron states is pronounced at the top surface layer while bulk-like behavior is exhibited at and below the subsurface layer. The Mott-Hubbard type insulating behavior in the bulk is retained in the surfaces, albeit with a smaller band gap.

The adsorption of O in the UO<sub>2</sub> (111) surface indicates that UO<sub>2</sub> oxidation is a stable process. The top site is the preferred adsorption site with adsorption energy of 5.37 eV. The presence of the adsorbate results in the change of the electronic work function by 2.56 eV, implying charge transfer from U to O. The analysis of the electronic density of states indicates hybridization between the O adsorbate 2p electron states and the neighboring U 5f electron states. Furthermore, the presence of the adsorbate did not alter the Mott-Hubbard insulating behavior seen in the bulk crystal and clean surface.

## Table of Contents

Acknowledgements.....	iii
Abstract.....	iv
List of Illustrations .....	viii
List of Tables.....	xi
Chapter 1 Introduction .....	1
Chapter 2 Theory and Computational Formalism .....	14
2.1 Density Functional Theory.....	14
2.1.1 Many Electron Hamiltonian .....	15
2.1.2 Hohenberg-Kohn Theorem.....	16
2.1.3 The Kohn-Sham Method .....	18
2.1.4 Approximations to the Exchange Correlation Functional .....	23
2.1.5 Hybrid Density Functional Theory .....	25
2.2 Computational Approach .....	26
2.2.1 Linear Augmented Plane Wave Method: LAPW .....	27
2.2.2 Augmented Plane Wave Plus lo Method: APW+lo.....	28
2.2.3 Full Potential and Spin-Orbit Interaction.....	30
Chapter 3 Hybrid Density Functional Study of the UO <sub>2</sub> (111) and (110) Surfaces .....	32
3.1 Computational Details .....	33
3.2 Bulk properties .....	33
3.3 Surface properties .....	40
3.3.1 Surface Calculations on the (111) and (110) Slabs with SOC .....	44
Chapter 4 Preliminary Oxygen Adsorption Calculations on the UO <sub>2</sub> (111) surface .....	57
4.1 Computational Details .....	58
4.2 Results and Discussion .....	63

Chapter 5 Conclusion .....	69
Appendix A NSO (110) and (111) Surface Tables and Figures.....	71
References.....	78
Biographical Information .....	90

## List of Illustrations

Figure 1: The Nuclear Fuel Cycle. <sup>12</sup> .....	2
Figure 2: Pictorial representation of the ISL process. (Image courtesy Heathgate Resources) <sup>15</sup> .....	4
Figure 3: A bank of centrifuges at a Urenco plant. <sup>17</sup> .....	5
Figure 4: Storage pond for used fuel at the Thermal Oxide Reprocessing Plant at the UK's Sellafield site. (Sellafield Ltd) <sup>18</sup> .....	7
Figure 5: A spent-fuel-storage cask that can hold about 12 tons of spent fuel. <sup>28</sup> .....	8
Figure 6: Kohn Sham self-consistent loop. ....	22
Figure 7: Energy versus Volume optimization Hybrid DFT SOC calculations. The P-V plot was obtained from the Murnaghan EOS. The equilibrium volume is $V_0 = 83.58 \text{ \AA}^3$ .....	35
Figure 8: Electronic density of states and band structure of the bulk $\text{UO}_2$ crystal. The dash line denotes the Fermi level. ....	38
Figure 9: Depiction of the difference charge density plot, $\Delta\rho(r)$ . The yellow regions denote excess build-up, while the cyan regions denote charge deficiency. The U and O atoms are colored grey and red respectively. The iso-level surface is 0.02 e/a.u. <sup>3</sup> .....	39
Figure 10: (a) Top view and (b) side view depiction of the (110) and (111) seven layer slabs. The slabs have inversion symmetry about the center of the bulk layer. U atoms are colored grey and O atoms are colored red. ....	41
Figure 11: Variations of the energy per formula unit (that is, per $\text{UO}_2$ ) of the (111) and (110) SO surfaces as a function of slab thickness. The dashed line denotes the energy per formula unit for the bulk crystal. ....	45

Figure 12: Variations of the incremental energies of the (111) and (110) SO slabs as a function slab thickness.....	46
Figure 13: Linear least square fit with $E_{tot}(N)$ as the dependent variable and $N$ as the independent variable via equation (3.5) yields $E_B$ as the slope and $\ell$ as the intercept on the $E_{tot}(N)$ axis.....	48
Figure 14: Variations of the surface energies of the (111) and (110) SO slabs as a function of slab thickness. The dashed line denotes the surface energy of a slab of semi-infinite thickness.....	50
Figure 15: Variations of the electronic work function of the (111) and (110) SO slabs as a function of slab thickness.....	52
Figure 16: Plots of the SO surface electronic band gaps as a function of slab thickness. The dashed horizontal line denotes the band gap of the bulk crystal.....	54
Figure 17: Angular-momentum resolved electronic density of states of each unique O-U-O formula unit of the (110) SO slab with 7 formula units (cf. Figure 10 (b) for the (110) surface).....	55
Figure 18: Angular-momentum resolved electronic density of states of each unique O-U-O formula unit of the (111) SO slab with 7 formula units (cf. Figure 10 (b) for the (111) surface).....	56
Figure 19: Atomic O initially placed at the top site of the 5 layer $UO_2$ (111) $\sqrt{3} \times \sqrt{3} - R30^\circ$ surface. The O adsorbate coverage is 1/3 ML.....	60
Figure 20: Atomic O initially placed at the two-fold bridge site of the 5 layer $UO_2$ (111) $\sqrt{3} \times \sqrt{3} - R30^\circ$ surface. The O adsorbate coverage is 1/3 ML.....	61
Figure 21: Atomic O initially placed at the three-fold hollow site of the 5 layer $UO_2$ (111) $\sqrt{3} \times \sqrt{3} - R30^\circ$ surface. The O adsorbate coverage is 1/3 ML.....	62

Figure 22: A depiction of the difference charge density plot,  $\Delta\rho(r)$ , for O top site. The yellow regions denote electron density build-up, while the cyan regions denote charge electron density deficiency. The U and O atoms are colored grey and red respectively; the O adsorbate is colored blue. The iso-level surface is 0.01 e/a.u.<sup>3</sup> ..... 67

Figure 23: A depiction of the difference charge density plot,  $\Delta\rho(r)$ , for O bridge site. The atom color scheme and electron density color scheme is the same as in Figure 22. .... 67

Figure 24: Electronic density of states of the top site and bare slab. The dash line denotes the Fermi level..... 68

Figure 25: Variations of the energy per formula unit (that is, per UO<sub>2</sub>) of the (111) and (110) NSO surfaces as a function of slab thickness. The dashed line denotes the energy per formula unit for the bulk crystal..... 74

Figure 26: Variations of the incremental energies of the (111) and (110) NSO slabs as a function slab thickness..... 75

Figure 27: Variations of the surface energies of the (111) and (110) NSO slabs as a function of slab thickness. The dashed line denotes the surface energy of a slab of semi-infinite thickness..... 76

Figure 28: Plots of the NSO surface electronic band gaps as a function of slab thickness. The dashed horizontal line denotes the band gap of the bulk crystal..... 77

## List of Tables

<p>Table 1: Surface properties of <math>\text{UO}_2</math> (110) SO AFM films. <math>E_{tot}(N)</math> is the total energy, <math>\Delta E_N</math> is the slab incremental energy, <math>\gamma</math> is the surface energy, <math>\Phi</math> is the work function, and <math>\Delta_{gap}</math> is the band gap of the <math>N</math>-layer slab. <math>E_{tot}(N)</math> and <math>\Delta E_N</math> have been shifted by +56468 Ry. ....</p>	42
<p>Table 2: Surface properties of <math>\text{UO}_2</math> (111) SO AFM films. <math>E_{tot}(N)</math> is the total energy, <math>\Delta E_N</math> is the slab incremental energy, <math>\gamma</math> is the surface energy, <math>\Phi</math> is the work function, and <math>\Delta_{gap}</math> is the band gap of the <math>N</math>-layer slab. <math>E_{tot}(N)</math> and <math>\Delta E_N</math> have been shifted by +56468 Ry. ....</p>	43
<p>Table 3: Equilibrium energetic and geometry parameters of the optimized slab adsorbate configurations.....</p>	63
<p>Table 4: The U spin magnetic moments inside a muffin tin sphere for the bulk layer, subsurface layer (<math>\mu_2</math>), and top layer (<math>\mu_1</math>). <math>\delta\phi = \phi_{slab+adsorbate} - \phi_{slab}</math> is the change in work function due to adsorption, where the work function of the clean slab is <math>\delta\phi = 3.46</math> eV. ....</p>	64
<p>Table 5: Surface properties of <math>\text{UO}_2</math> (110) NSO AFM films. <math>E_{tot}(N)</math> is the total energy, <math>\Delta E_N</math> is the slab incremental energy, <math>\gamma</math> is the surface energy, <math>\Phi</math> is the work function, and <math>\Delta_{gap}</math> is the band gap of the <math>N</math>-layer slab. <math>E_{tot}(N)</math> and <math>\Delta E_N</math> have been shifted by +56468 Ry. ....</p>	72
<p>Table 6: Surface properties of <math>\text{UO}_2</math> (111) NSO AFM films. <math>E_{tot}(N)</math> is the total energy, <math>\Delta E_N</math> is the slab incremental energy, <math>\gamma</math> is the surface energy, <math>\Phi</math> is the work</p>	

function, and  $\Delta_{gap}$  is the band gap of the  $N$ -layer slab.  $E_{tot}(N)$  and  $\Delta E_N$  have  
been shifted by +56468 Ry ..... 73

## Chapter 1

### Introduction

Uranium dioxide ( $\text{UO}_2$ ) commonly known for extensive applications in military and commercial nuclear technology, particularly as a nuclear fuel, has another side that attracts scientific attention and environmental concerns. The primary concerns that arise come from the corrosion of  $\text{UO}_2$  surfaces and potential release of  $\text{UO}_2$ -based materials into the biosphere and the impact to the ground water system and atmosphere. Corrosion and weathering of  $\text{UO}_2$  upon the exposure to environmental elements lead to the breakdown of the material.<sup>1-5</sup> In fact, the oxidation of  $\text{UO}_2$  leads to a volume expansion up to 38%; therefore the corrosiveness of  $\text{UO}_2$  could impact the integrity of fuel rods in nuclear reactors and nuclear waste storage facilities.<sup>1, 6-8</sup> From an environmental perspective, it is possible for tiny particulates of uranium oxides to escape into the environment during mining of uranium ore, milling, and the final and reprocessing stages in nuclear fuel preparation before use in a reactor. The use of depleted uranium munitions as well as oxidative corrosion can result in the dispersal of large quantities of uranium oxide particles into the environment.<sup>4</sup> The presence (of oxide particulates and other complexes) in the biosphere, even at very low concentrations, could lead to unacceptable public health consequences.<sup>9</sup>

Currently, there are over 200 mineral species containing U.<sup>10</sup> The radiation signature of uranium's decay products allows the deposits to be recognized and mapped from the air, making it much easier to find than other minerals. Uranium in the Earth's crust and oceans is more abundant than gold and mercury, and almost the same as tin.<sup>11</sup> The life cycle of uranium (Figure 1) from a mineral form into fuel for a nuclear reactor is quite intricate.

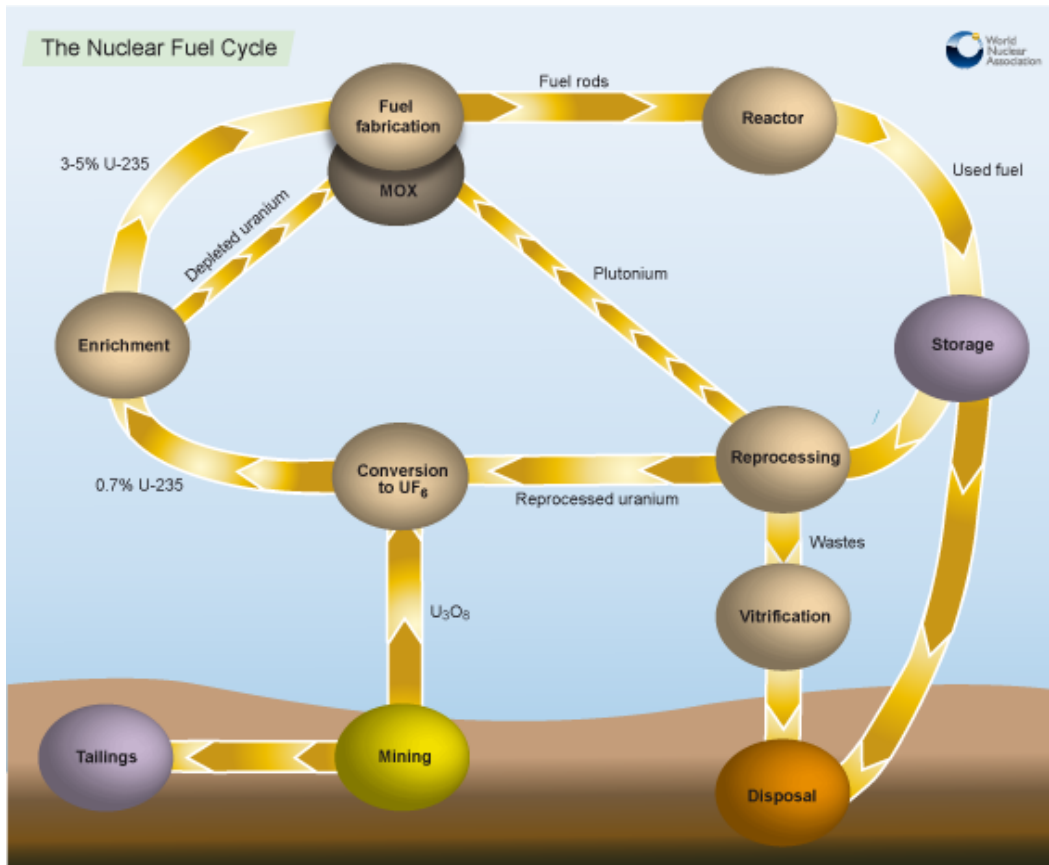


Figure 1: The Nuclear Fuel Cycle.<sup>12</sup>

First, uranium is mined, either by underground mining, open pit mining, or in situ leach (ISL) mining (the USA calls it in situ recovery or ISR). It is important to point out, although uranium itself is barely radioactive, the ore that is mined and crushed contains more radioactive elements such as radon and radium in the ore due to the radioactive decay of uranium over a few millions of years. Since radon, a radioactive inert gas, is airborne, precaution is needed to protect the workers from exposure, especially inadequately ventilated mines. Underground mining is used when the deposits are deep underground, whereas open pit mining is used when the deposits are close to the

surface. Safeguards should be taken when extracting the ore via underground mining, like a ventilation system, which prevents airborne radiation exposure into the atmosphere.<sup>13</sup>

The environmental impact from underground mining compared to open pit mining is less since there is not as much ground disturbance. The shafts and tunnels needed for underground mining can reach as deep as 600 meters below the surface. With ISL mining, weakly acidified or alkaline groundwater that is rich in oxygen is circulated within an enclosed underground aquifer. This underground aquifer holds the uranium ore in porous material such as gravel or sand. When it is ready to be accessed, a leaching solution dissolves the uranium before it is pumped to the treatment plant where uranium is recovered as a precipitate.<sup>13, 14</sup>

At the mill site, the uranium ore is ground to a fine substance, leached in sulfuric acid, allowing the separation of the uranium from waste rock, also called the tailings. This leach solution goes through a few more processes before it can be dried and heated. The final product is a uranium oxide ( $U_3O_8$ ) concentrate, sometimes referred to as “yellow cake,” which contains more than 80% of the uranium oxide concentrate. Note that the original uranium ore deposits contain around 0.1% uranium. This product is packed and sealed for shipment. ISL mills (Figure 2) follow a similar process minus the grinding into a fine substance part.<sup>13</sup>

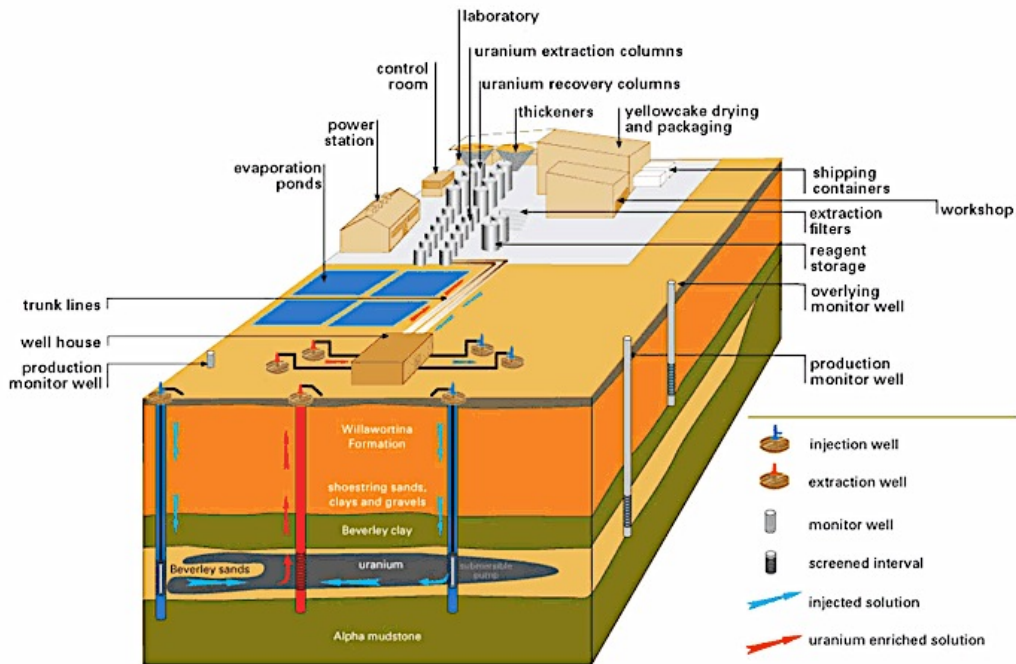


Figure 2: Pictorial representation of the ISL process.

(Image courtesy Heathgate Resources)<sup>15</sup>

In a uranium purification and conversion plant, there are two ways to enrich uranium on a commercial scale - diffusion process and centrifuge process. Both of these processes use uranium hexafluoride ( $UF_6$ ) as the feed material.<sup>16, 17</sup>

In the diffusion process, it forces  $UF_6$  gas under pressure through a string of porous membranes or what is called diaphragms. The  $UF_6$  gas molecules (with  $U^{234}$  and  $U^{235}$  atoms) are lighter therefore diffusing more quickly than the heavier  $UF_6$  gas molecules containing  $U^{238}$ . Some 1400 stages are needed before  $UF_6$  contains enough  $U^{235}$  to be used in a reactor.<sup>16, 17</sup>

In Figure 3 a bank of centrifuges is depicted. The centrifuge process takes the  $UF_6$  gas and feeds it through a series of vacuum tubes, each containing a rotor. The

rotors are then spun quickly, 50,000-70,000 rpms, heavier molecules with  $U^{238}$  increase in concentration to the outer edge of the cylinder and the lighter  $U^{235}$  molecules are concentrated near the center. Slightly enriched  $U^{235}$  is withdrawn and fed into the next higher stage, whereas the slightly depleted stream is recycled back into the next lower stage. For the centrifuge process, only 10 to 20 stages are needed, unlike in the diffusion process. The enriched  $UF_6$  is converted into  $UO_2$ , made into fuel pellets, and encased into metal tubes, which form the fuel rods. During the enrichment process it is important that  $UF_6$  is not exposed to moisture, or it forms an extremely corrosive material called hydrofluoric acid.<sup>16, 17</sup>

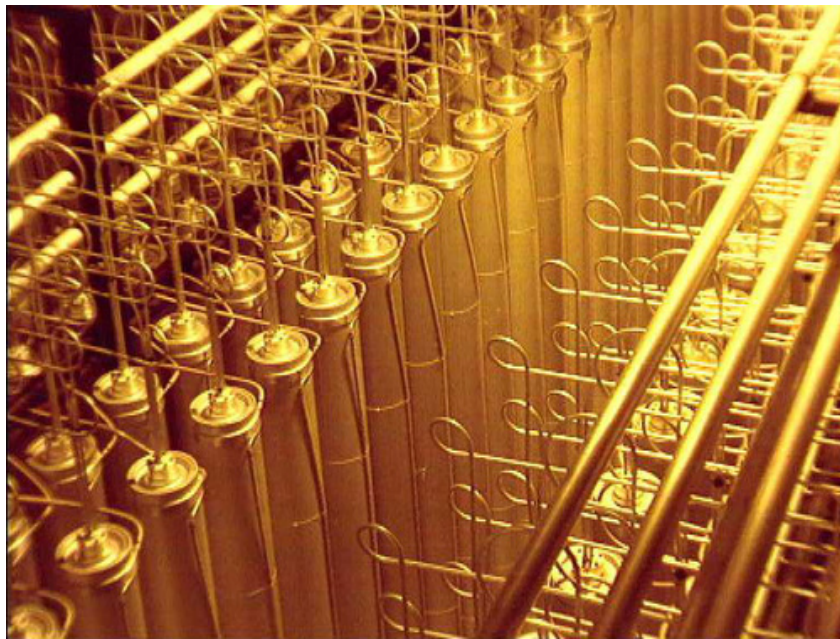


Figure 3: A bank of centrifuges at a Urenco plant.<sup>17</sup>

The amount of high level waste (HLW) stored in the world is about 270,000 tons. Approximately 90% of the HLW is stored in pools at the reactor sites and the remaining in

dry storage casks. Each year 12,000 tons of HLW is produced and only 3,000 tons get reprocessed.<sup>18, 19</sup> There are 434 nuclear reactors in operation worldwide. There are 72 under construction, another 173 on order or planned, and 309 proposed.<sup>20, 21</sup> Several countries are considering a geological depository for the future of HLW storage, but as of today, there is not a geological depository for HLW in the world.<sup>18, 19</sup>

There are 100 nuclear power plants in 31 different states in the United States, which produce 20% of the U.S. electricity.<sup>22</sup> Approximately 70% of the nuclear reactors could be taken offline by 2035, and all by 2050 if their licenses terminate due to required safety upgrades. Additional factors that could influence the decision to decommission the nuclear reactors are costly repairs and the competition of cheap natural gas.

The United States' contribution to HLW is nearing 70,000 metric tons. Each year the U.S. adds approximately 2,000-2,300 metric tons.<sup>23, 24</sup> The U.S. like many other countries stores HLW in spent fuel pools and dry casks. Of the 70,000 metric tons of HLW, 78% is in pools, with the remaining 22% in dry casks.<sup>25</sup>

Spent fuel pools are located inside the plant's protected area with thick reinforced-steel concrete walls, lined with stainless steel. Figure 4 is an example of a storage pond for used fuel. The pools are built to code for seismic activity and other natural phenomena. Above the tops of the fuel is at least 20 feet of water. This water helps keep the temperature regulated and protects the fuel rods if debris fell into the pool.<sup>26</sup> The spent fuel will stay inside the pools for at least 5 years before transferred into a dry cask.<sup>25</sup> It is important to note, water is crucial for nuclear reactors, because without water it would cause chaos to the cooling of these plants. In drought states, this could pose a problem if the reactor sites do not have their own water source and must pull from a water source cities use for its residents.



Figure 4: Storage pond for used fuel at the Thermal Oxide Reprocessing Plant at the UK's Sellafield site. (Sellafield Ltd)<sup>18</sup>

Dry casks surround the cooled spent fuel with inert gas inside a container or cask. These casks (cf. Figure 5) are steel cylinders sealed by bolting or welded shut. Then additional steel, concrete, and other material is used to encompass the dry casks to shield the radiation from workers and the public.<sup>27</sup> The dry casks are built to be resistant to natural phenomena, projectiles, and temperature extremes.

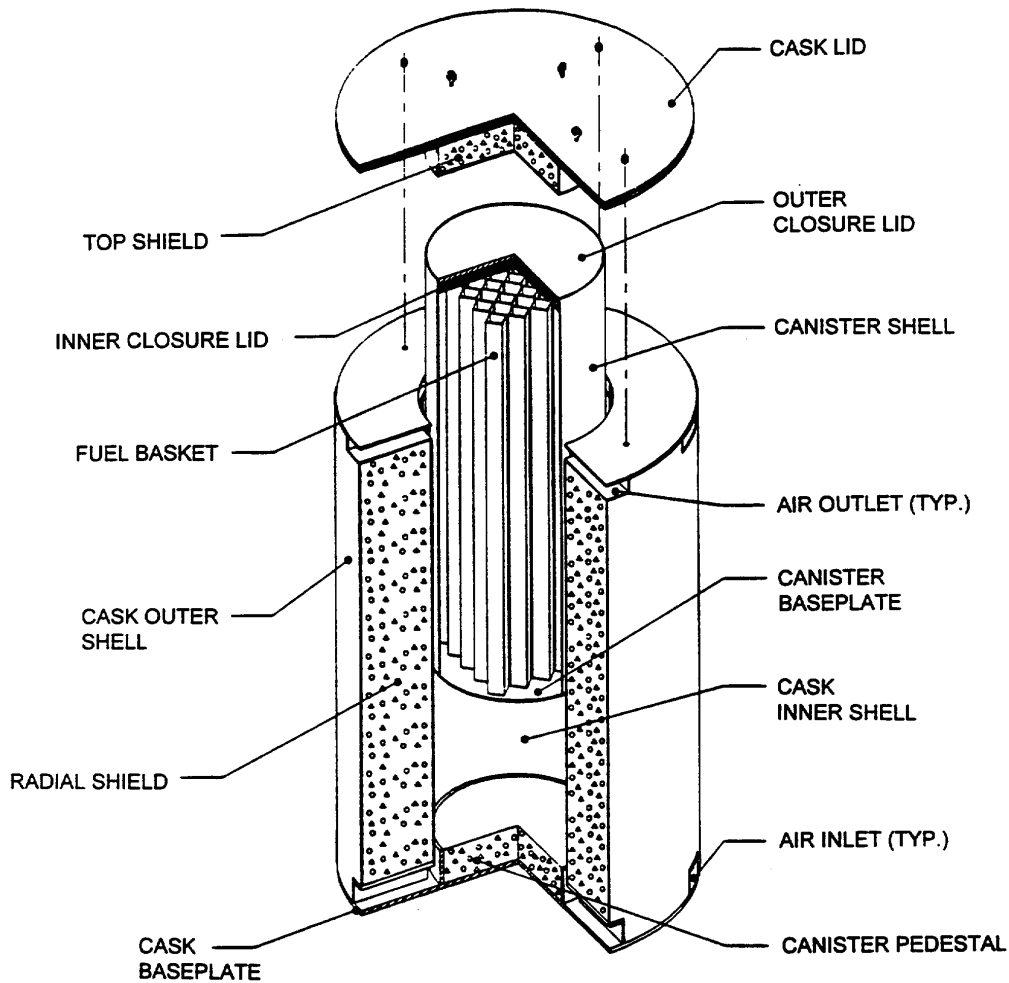


Figure 5: A spent-fuel-storage cask that can hold about 12 tons of spent fuel.<sup>28</sup>

Whether the spent fuel is stored in a pool or dry cask, many concerns can arise, from the leakage of nuclear waste into ground water or the atmosphere and hundreds of years of natural phenomena possibly leading to a breakdown of the structural integrity of the dry casks. Whether a permanent resting place for HLW is needed or a place where the waste is retrievable, we need to be responsible and take in all the factors if geological

depository is the direction to take. The alternative is to advance our knowledge in technology such that the HLW can be utilized as fuel inside a nuclear reactor.

In this thesis work, a theoretical approach is taken to understand the surface properties of  $\text{UO}_2$  using hybrid Density Functional Theory (DFT). Significant experimental efforts have been made to understand the processes and mechanisms involved with the interactions of  $\text{UO}_2$  and other nuclear materials with the environment.<sup>4, 29-35</sup> However, difficulties encountered in experimental studies can be attributed to the hazardous nature of these materials. In this regard, theoretical studies can supplement experimental efforts to understand the mechanisms via which  $\text{UO}_2$  materials interact with the biosphere. The theoretical approach to tackling the interactions of  $\text{UO}_2$  with common environmental species (e.g. water and oxygen gas) begin at the atomic and molecular scales. It is important to note, in general, the interactions of materials with other species are initiated at the material's surface. Specifically, the interactions of  $\text{UO}_2$  with environmental species begin on its surfaces. For example, to model the mechanisms through which other oxides of uranium form, one could begin with the adsorption and dissociation of molecular oxygen or water on  $\text{UO}_2$ . The implication here is that a thorough understanding of the properties of  $\text{UO}_2$  surfaces is a necessary step to understand the surface interactions with environmental species.

The physical and chemical properties of the actinides—the group of elements in the last row of the periodic table—to which uranium belongs, are largely dictated by their 5f electrons. The chemical complexities of the 5f electrons, particularly in condensed phases, require an accurate, parameter-free, first principles method. Experimental studies have shown  $\text{UO}_2$  to be an anti-ferromagnetic insulator below 30.8 K otherwise it is paramagnetic.<sup>36-41</sup> Experimental works also indicate that  $\text{UO}_2$  is a Mott insulator with a band gap of 2.1 eV.<sup>42-47</sup> However, the *de facto* theoretical method for modeling materials,

namely Density Functional Theory (DFT)<sup>48, 49</sup>, within the local density approximation (LDA)<sup>50, 51</sup> or generalized gradient approximation (GGA)<sup>52</sup> to the exchange-correlation functional, predicts UO<sub>2</sub> to be a ferromagnetic conductor.<sup>53-56</sup> The shortcomings of DFT-LDA or DFT-GGA to describe UO<sub>2</sub> can be remedied by hybrid density functional theory (hybrid DFT)<sup>57-59</sup>, DFT plus the Hubbard *U* (DFT+*U*)<sup>60</sup> method, self-interaction correction (SIC)<sup>61</sup>, or DFT plus dynamical mean-field theory (DFT+DMFT)<sup>62, 63</sup>. A plethora of calculations employing these methods have succeeded in sufficiently describing the properties of bulk UO<sub>2</sub>,<sup>46, 53, 54, 64-89</sup> particularly its magnetic character and electronic band gap.

Although the DFT+*U* and DFT+DMFT methods work for UO<sub>2</sub>, they require the introduction of material-specific parameters. For example, in most DFT+*U* calculations for UO<sub>2</sub>, the value of the parameter *U* is continuously adjusted until the band gap matches the experimental value. By doing so, the integrity of an important property of the system (e.g. lattice constant) can be compromised. On the other hand, hybrid DFT is a fully first principles method since it differs from DFT-LDA and DFT-GGA only in the formulation of the electron exchange interaction. This work is thus focused on the application of hybrid DFT to model the properties of clean and adsorbate-covered low index UO<sub>2</sub>, namely the (110) and (111) surfaces and the interaction of atomic oxygen with the (111) surface. All calculations were done with spin-orbit coupling. The goal is to study the variation in surface properties with the thickness of each surface structure and predict important surface properties such as the electronic work function and surface energy. We shall summarize the previous experimental and theoretical studies on UO<sub>2</sub> surfaces.

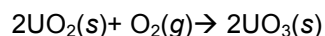
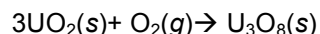
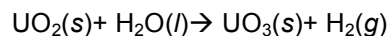
Regarding experimental studies, Hall and Mortimer reported experimental surface energies,  $\gamma = 0.85 - 1.40 \times 10^{-4} T \text{ Jm}^{-2}$  ( $273 < T < 3123 \text{ K}$ ), of UO<sub>2</sub>, albeit with a large uncertainty of 70%.<sup>90</sup> Other high temperature experimental data yielded surface

energies ranging from  $0.48 \text{ Jm}^{-2}$  at 1450 K to  $1.032 \text{ Jm}^{-2}$  at 1375 K.<sup>91,92</sup> Experimental measurements by Page and Wooley yielded a work function of  $3.5 \pm 0.5 \text{ eV}$  for  $\text{UO}_2$ .<sup>93</sup>

Only a few first principles DFT-based studies have been done on clean  $\text{UO}_2$  surfaces.<sup>88,94-97</sup> There are also a few calculations in which empirical<sup>94,98</sup> and semi-empirical<sup>99</sup> methods were employed. Regarding DFT-based works, Chaka and co-workers<sup>88</sup> used DFT-GGA and *ab initio* thermodynamics to delineate the initial stages of surface and subsurface oxidation of  $\text{UO}_2$  at the (111) surface as a function of temperature and oxygen pressure. Weck *et al.*<sup>95</sup> used GGA+*U* to study the DFT properties of the (111)  $\text{UO}_2$  surface and the work is in good agreement with experimental values for the surface energy and work function. Evarestov *et al.*<sup>96</sup> studied the properties of  $\text{UO}_2$  (111) surface with 9, 15, and 21 atomic planes using Hartree-Fock theory and DFT with linear combination atomic orbitals; they computed the surface energies and other surface properties for antiferromagnetic surface structures. Rák *et al.*<sup>97</sup> used the DFT+*U* (with several values of *U* employed) to calculate the properties of low index surfaces of  $\text{UO}_2$  from 2-6 formula units. However, their work was focused on the ferromagnetic spin configuration, even though  $\text{UO}_2$  is anti-ferromagnetic. Rabone *et al.*<sup>100</sup> used DFT+*U* with mixed Gaussian/plane waves basis to study low index  $\text{UO}_2$  surfaces. Their work resulted in a novel method that can be employed to bypass metastable surface states. Skomurski *et al.*<sup>94</sup> used empirical and DFT-based quantum mechanical methods to study low index surfaces of  $\text{UO}_2$  and observed the (111) surface had the lowest surface energy.

As mentioned earlier, the stability of  $\text{UO}_2$  waste disposal conditions in the long-term is of crucial importance since its corrosion can yield a wide range of complexes, which could result in serious health and environmental consequences. The corrosion of  $\text{UO}_2$  is initiated when the  $\text{UO}_2$  surface is oxidized by moist air (water) or dry air (molecular

oxygen). Understanding the atomic scale processes, which dictate the oxidation mechanism, begins with the molecular scale modeling of reactions such as



As simple as these reactions seem, experimental works<sup>2, 101-122</sup> indicate that the oxidation process is quite complicated because the formation of the intermediate oxides  $\text{UO}_{2+x}$  is not well understood. In an effort to gain some fundamental atomic scale understanding of the oxidation process, we studied atomic adsorption on the  $\text{UO}_2$  (111) surface. We summarize below, prior theoretical modeling of atomic and molecular adsorptions on the  $\text{UO}_2$  surfaces.

Boettger, *et al.*<sup>123</sup> did linear combinations of Gaussian-type orbitals-fitting function (LCGTO-FF) to investigate the cohesive properties of clean and hydroxylated  $\text{UO}_2$  (111) surfaces within DFT-GGA. Chaka, *et al.*<sup>88</sup> did GGA-DFT and ab initio thermodynamics to determine degree of oxidation of the uranyl 7 formula unit  $\text{UO}_2$  (111) surface as a function of temperature and oxygen pressure. Skomurski, *et al.*<sup>124</sup> did quantum mechanical DFT, as implemented in CASTEP, adsorption of molecular water on a 4 formula unit  $\text{UO}_2$  (111) slab with half-monolayer coverage, single and double sided full monolayer coverage. Tan, *et al.*<sup>125</sup> did atomic scale computer simulation using MARVIN. They did low index relaxed surface hydroxide surfaces with 50% and 100% coverage. Weck, *et al.*<sup>95</sup> did GGA+U AFM relaxed  $\text{UO}_2$  (111) half-monolayer coverage of molecular water, dissociated water, and atomic oxygen. That study also did full monolayer coverage of molecular water and co-adsorbed atomic oxygen. Rák, *et al.*<sup>97</sup> did DFT+U adsorption of water molecules in dissociated configurations on a 6 formula unit relaxed  $\text{UO}_2$  low index slabs.

The computational modeling presented in this thesis are in two parts: (i) We have used periodic slab model representations of the  $\text{UO}_2$  (110) and (111) surfaces to model the clean surface properties and electronic structure using all-electron hybrid DFT. Specifically we examined the convergence of the surface properties with respect to system size. The clean surface properties of interest were the slab incremental energies, surfaces energies and work functions. We also probed electronic properties such as the band gap and U  $5f$  electron localization/delocalization behavior at the surface. (ii) We used density functional theory and hybrid DFT to probe the adsorption of atomic oxygen on the  $\text{UO}_2$  (111) surface. This is a simplified version of the precursor to  $\text{UO}_2$  oxidation and preliminary results from on-going calculations will be presented. Specifically, we will present a few results on the strength of the binding of O to the surface, the preferred adsorption site, and the adsorbate-induced effects on the electronic work function and the electronic structure.

The remainder of this thesis is organized as follows. In chapter 2, density functional theory and the computational formalism will be described. In chapter 3, the results of the  $\text{UO}_2$  surface properties using hybrid DFT will be presented. Chapter 4 will touch on the ongoing work of adsorption of atomic Oxygen on the 5 formula unit  $\text{UO}_2$  (111) slab. Finally in chapter 5, a summary of the work will be presented.

## Chapter 2

### Theory and Computational Formalism

#### 2.1 Density Functional Theory

Since the seminal work on density functional<sup>a</sup> theory (DFT) by Hohenberg, Kohn and Sham,<sup>48, 49</sup> many electronic structure calculations for solids, liquids, and gases have employed DFT as a method of choice. In this chapter we describe the density functional method for electronic structure calculations. We first present, albeit briefly, the underlining concepts of DFT. In a nutshell DFT provides an elegant way of reducing the complex many electron system problem via the total electron density, there by significantly reducing the computational cost in comparison to the traditional *ab initio* theories such as Hartree-Fock<sup>126, 127</sup> (HF) theory, while retaining the computational accuracy. In principal, DFT is an 'exact' theory and is applicable to any interacting system with an external potential. The holy grail of DFT is the exact representation of the exchange-correlation functional. Exchange correlation functionals based on the local density (LDA), semi-local density (GGA), and recently exchange correlation functionals with dynamic effects (meta-GGA) have been developed for a wide variety of systems. There is also a class of exchange correlation functionals in which a fraction of approximate DFT exchange is replaced with exact HF exchange; these are the so called hybrid exchange correlation functionals. In the following we will present a short description of DFT based on the reviews of Lieb<sup>128</sup>, Parr and Yang<sup>129, 130</sup>, Capelle<sup>131</sup> and Nagy and Andrejkovics<sup>132-134</sup>.

---

<sup>a</sup> In very simple terms, a functional maps a function to another function. A functional is distinguished from a function by [ ] brackets. A functional  $f : A \rightarrow B$  is defined as  $f[y(x)] \in B$ , where  $y(x) \in A$ . In DFT the energy is the functional of the electron density.

### 2.1.1 Many Electron Hamiltonian

Within the Born-Oppenheimer<sup>b</sup> approximation<sup>135</sup>, the many electron Hamiltonians are defined as:

$$H = T + V_{ee} + V_{ne} \quad (2.1)$$

where  $T$  is the kinetic energy operator,  $V_{ee}$  is the electron-electron repulsion operator, and  $V_{ne}$  is the electron-nuclei interaction operator. In atomic units<sup>c</sup>, these operators are defined as:

$$T = -\frac{1}{2} \sum_i^N \nabla_i^2 \quad (2.2)$$

$$V_{ee} = \sum_{i < j}^N \frac{1}{r_{ij}} \quad (2.3)$$

$$V_{ne} = \sum_{i \in \text{electron}} \sum_{I \in \text{nuclei}} \frac{1}{|r_i - R_I|} \quad (2.4)$$

The goal of DFT is to determine the ground state energy  $E$  of a many electron system by solving the time independent Schrödinger equation,  $H\Psi = E\Psi$ , without explicitly knowing  $\Psi$ , where  $\Psi$  is the many electron wave function and  $E$  is the corresponding eigenvalue. This is achieved by expressing  $E$  as a functional of the electron density  $\rho(\vec{r})$  ( $\vec{r}$  is an arbitrary point in space). For a system of  $N$  electrons, we define  $\rho(\vec{r})$  as:

---

<sup>b</sup> The approximation states that the electronic mass is greatly smaller (1/1821) than the mass of the nucleus. Hence their wave functions can be decoupled.

<sup>c</sup> In atomic units,  $e = \hbar = m_e = 1$ , where  $e$  is the electronic charge,  $\hbar$  is Plank's constant,  $m_e$  is the electron mass, the unit of energy is given in Hartrees (H),  $1 \text{ a.u. (energy)} = 1H = 27.2116 \text{ eV}$ , and the unit for distance is in Bohrs,  $1 \text{ a.u. (distance)} = 1 \text{ Bohr} = 0.529 \text{ \AA}$ .

$$\rho(\vec{r}) = N \int \Psi^*(\vec{x}_1, \vec{x}_2, \dots, \vec{x}_N) \Psi(\vec{x}_1, \vec{x}_2, \dots, \vec{x}_N) d\vec{x}_1 d\vec{x}_2 \dots d\vec{x}_N . \quad (2.5)$$

Here  $\Psi$  is assumed to be normalized to unity; and  $\vec{x}_i$ 's include both spin and spatial variables, in equation (2.5), that are integrated over the N spatial and spin coordinates. Once the electronic density is known in DFT, all ground state electronic properties can in principle be computed.  $\rho(\vec{r})$  satisfies the following constraints:

$$N = \int \rho(\vec{r}) d\vec{r} . \quad (2.6)$$

Another quantity of key importance in DFT is the external potential,  $v(\vec{r})$ , felt by the electrons due to the presence of the nuclei. The theorems to follow signifies importance of  $v(\vec{r})$ .

### 2.1.2 Hohenberg-Kohn Theorem

The foundation of modern DFT rests on two theorems by Hohenberg and Kohn.<sup>48</sup> Here we will state the theorems and the reader is referred to the original paper for the proofs of the theorems.<sup>48</sup>

Theorem I: *The external potential  $v(\vec{r})$  is (to within a trivial additive constant) uniquely determined by the ground state electron density  $\rho(\vec{r})$ .*

Theorem II: *A universal function of the density  $\rho(\vec{r})$  for the energy  $E[\rho]$  can be defined for all electron systems. Furthermore, for any trial electron density  $\tilde{\rho}(\vec{r})$  associated with some external potential  $v$ , the ground state electron density*

$\rho(\vec{r})$  minimizes  $E[\tilde{\rho}]$  and the corresponding minimum energy is the ground state energy.

The first theorem guarantees the existence of a bijection from  $\rho(\vec{r}) \rightarrow v(\vec{r})$ . The second theorem suggest that the energy functional,  $E[\rho]$ , is sufficient to determine all the ground state properties.

In DFT the total energy functional is written as,

$$\begin{aligned} E_v[\rho] &= T[\rho] + V_{ne}[\rho] + V_{ee}[\rho] \\ &= \int \rho(\vec{r})v(\vec{r})d\vec{r} + F_{HK}[\rho] \\ F_{HK}[\rho] &= T[\rho] + V_{ee}[\rho]. \end{aligned} \tag{2.7}$$

Here  $V_{ee}$  includes both the classical and non-classical (for example, Coulomb and exchange interactions) contributions and  $F_{HK}$  is the Hohenberg-Kohn functional, which does not depend on the external potential. If the exact form of the functional  $F_{HK}$  is known, then equation (2.7) in principle is exact.

The variation of the total energy with the constraint that the total electrons are fixed, results in,

$$\delta \left\{ E_v[\tilde{\rho}] - \mu \left[ \int \tilde{\rho}(\vec{r}) d\vec{r} - N \right] \right\} = 0. \tag{2.8}$$

This leads to the Euler-Lagrange equation

$$\mu = \frac{\delta E_v[\tilde{\rho}]}{\delta \tilde{\rho}(\vec{r})} = v(\vec{r}) + \frac{\delta F_{HK}}{\delta \tilde{\rho}(\vec{r})}. \tag{2.9}$$

In the above equation the Lagrange multiplier  $\mu$  is the chemical potential.

### 2.1.3 The Kohn-Sham Method

The exact form of the Hohenberg-Kohn functional,  $F_{HK}[\rho]$ , is not known.

$$F_{HK}[\rho] = T[\rho] + V_{ee}[\rho]. \quad (2.10)$$

The first road block in determining the functional is how to compute the kinetic energy functional. The Kohn-Sham method provides a simple way to compute a portion of the kinetic energy functional and the remaining component is determined by other means. The Kohn-Sham method is briefly described below.

Let us consider a system of non-interacting electrons moving independently in a common local potential  $v$ , where the electronic density  $\rho(\vec{r})$  is the same as the interacting electronic system. The Hamiltonian is:

$$H_s = \sum_i^N \left( -\frac{1}{2} \nabla_i^2 \right) + \sum_i^N v(\vec{r}_i). \quad (2.11)$$

In the above Hamiltonian there is no electron-electron repulsion term. For this system we can write the non-interacting wave-function as the Slater<sup>127</sup> determinant:

$$\Psi = \frac{1}{\sqrt{N!}} \det[\psi_1 \psi_2 \dots \psi_N] \quad (2.12)$$

where  $\psi_i$  are the  $N$  lowest eigenstates of the one-electron Hamiltonian  $h$ :

$$h\psi_i = \left[ -\frac{1}{2} \nabla_i^2 + v(\vec{r}_i) \right] \psi_i = \varepsilon_i \psi_i. \quad (2.13)$$

The Kohn-Sham kinetic energy of this non-interacting system,

$$T_{KS}[\rho] = \left\langle \Psi \left| \sum_{i=1}^N \left( -\frac{1}{2} \nabla_i^2 \right) \right| \Psi \right\rangle = \sum_i^N \left\langle \psi_i \left| -\frac{1}{2} \nabla_i^2 \right| \psi_i \right\rangle \quad (2.14)$$

while the density of the non-interacting system

$$\rho(\vec{r}) = \sum_i^N |\psi_i(\vec{r})|^2 \quad (2.15)$$

is equal to that of an interacting one.

The kinetic energy functional  $T[\rho]$  in equation (2.10), as mentioned before, is unknown, simply take the kinetic energy functional  $T_{KS}[\rho]$  of the non-interacting system instead of  $T[\rho]$ . Let the difference between these two functional be  $\Delta T = T - T_{KS}$ , and substituting this in equation (2.10):

$$F_{HK}[\rho] = T_{KS}[\rho] + V_{ee}[\rho] + \Delta T[\rho]. \quad (2.16)$$

The last two terms on the right hand side of equation (2.17) represent the electron-electron interaction which can be rewritten as the Coulomb and exchange-correlation terms, respectively:

$$\begin{aligned} V_{ee}[\rho] + \Delta T[\rho] &= J[\rho] + \text{non-classical } e-e \text{ interaction} + \Delta T[\rho] \\ &= J[\rho] + E_{xc}[\rho] \end{aligned} \quad (2.17)$$

$E_{xc}[\rho] = \Delta T[\rho] + \text{non-classical } e-e \text{ interaction}$  is the exchange correlation functional and the accuracy of DFT depends on its representation. To be more specific, if  $E_{xc}[\rho]$  is exactly known then the DFT ground state energy is exact. Later on we will discuss approximations of  $E_{xc}[\rho]$ .

Use equation (2.17) and substitute it into equation (2.16):

$$F_{HK}[\rho] = T_{KS}[\rho] + J[\rho] + E_{xc}[\rho] \quad (2.18)$$

Using the above function the total energy of equation (2.17) can be written as:

$$E[\rho] = T_{KS}[\rho] + J[\rho] + E_{xc}[\rho] + \int \rho(\vec{r}) v(\vec{r}) d\vec{r}. \quad (2.19)$$

The variation of equation (2.19) give the Euler-Lagrange equation:

$$\begin{aligned}\mu &= \frac{\delta E[\rho]}{\delta \rho} = \frac{\delta}{\delta \rho} \int \rho(\vec{r}) v(\vec{r}) d\vec{r} + \frac{\delta T_{KS}[\rho]}{\delta \rho} + \frac{\delta J[\rho]}{\delta \rho} + \frac{\delta E_{xc}[\rho]}{\delta \rho} \\ &= v(\vec{r}) + \frac{\delta T_{KS}[\rho]}{\delta \rho} + \frac{\delta J[\rho]}{\delta \rho} + \frac{\delta E_{xc}[\rho]}{\delta \rho}\end{aligned}\quad (2.20)$$

$$= v_{eff}(\vec{r}) + \frac{\delta T_{KS}[\rho]}{\delta \rho}\quad (2.21)$$

where the Kohn-Sham effective potential is defined by:

$$\begin{aligned}v_{eff}(\vec{r}) &= v(\vec{r}) + \frac{\delta J[\rho]}{\delta \rho} + \frac{\delta E_{xc}[\rho]}{\delta \rho} \\ &= v(\vec{r}) + \int \frac{\rho(\vec{r}')}{|\vec{r} - \vec{r}'|} d\vec{r}' + v_{xc}(\vec{r})\end{aligned}\quad (2.22)$$

here we also defined the exchange-correlation potential as:

$$v_{xc}(\vec{r}) = \frac{\delta E_{xc}[\rho]}{\delta \rho}\quad (2.23)$$

From here, rewrite equation (2.19) in terms of one electron orbitals:

$$E[\rho] = \sum_i^N \int \psi_i^* \left( -\frac{1}{2} \nabla^2 \right) \psi_i d\vec{r} + J(\rho) + E_{xc}[\rho] + \int v(\vec{r}) \rho(\vec{r}) d\vec{r}\quad (2.24)$$

and the electron density is, as in equation (2.15):

$$\rho(\vec{r}) = \sum_i^N |\psi_i|^2$$

So, in equation (2.24) the energy is expressed in terms of N orbitals.

Now, taking the variation of energy in equation (2.24) with respect to the one-electron orbital  $\psi_i$ , along with the constraint that these orbitals are orthonormal to each other:

$$\int \psi_i^* \psi_j d\vec{x} = \delta_{ij} \quad (2.25)$$

We get,

$$\delta \left[ E[\rho] - \sum_i^N \sum_j^N \varepsilon_{ij} \int \psi_i^*(\vec{x}) \psi_j(\vec{x}) d\vec{x} \right] = 0 \quad (2.26)$$

In equation (2.26)  $\varepsilon_{ij}$  are the Lagrange multipliers. Let us now consider the variation in the energy  $E[\rho]$  given by the equation (2.24),

$$\delta E[\rho] = \left[ \frac{\delta}{\delta \psi_i^*} \sum_i^N \int \psi_i^* \left( -\frac{1}{2} \nabla^2 \right) \psi_i d\vec{r} + \frac{\delta J}{\delta \psi_i^*} + \frac{\delta E_{xc}}{\delta \psi_i^*} + \frac{\delta}{\delta \psi_i^*} \int v(\vec{r}) \left( \sum_i^N |\psi_i|^2 \right) d\vec{r} \right] \delta \psi_i^* \quad (2.27)$$

Using chain rule for functional derivative, the first term in the right hand side gives,

$$\begin{aligned} \frac{\delta}{\delta \psi_i^*} \sum_i^N \int \psi_i^* \left( -\frac{1}{2} \nabla^2 \right) \psi_i d\vec{r} &= \frac{\partial \psi_i^*}{\partial \psi_i^*} \left( -\frac{1}{2} \nabla^2 \right) \psi_i + \psi_i^* \frac{\partial}{\partial \psi_i^*} \left\{ \left( -\frac{1}{2} \nabla^2 \right) \psi_i \right\} \\ &= -\frac{1}{2} \nabla^2 \psi_i \end{aligned} \quad (2.28)$$

where derivative in the second term is zero. Similarly the last term in the variation of energy in equation (2.27) gives,

$$\frac{\delta}{\delta \psi_i^*} \int v(\vec{r}) \left( \sum_i^N |\psi_i|^2 \right) d\vec{r} = v(\vec{r}) \psi_i \quad (2.29)$$

From equation (2.26), for any arbitrary variation of  $\delta \psi_i^*$ , we get using equations (2.28)

and (2.29),

$$\begin{aligned} h_{\text{eff}} \psi_i &= \left[ -\frac{1}{2} \nabla^2 + \frac{\delta J[\rho]}{\delta \rho} + \frac{\delta E_{xc}[\rho]}{\delta \rho} + v(\vec{r}) \right] \psi_i = \sum_j^N \varepsilon_{ij} \psi_j \\ \Rightarrow h_{\text{eff}} \psi_i &= \left[ -\frac{1}{2} \nabla^2 + v_{\text{eff}}(\vec{r}) \right] \psi_i = \sum_j^N \varepsilon_{ij} \psi_j \end{aligned} \quad (2.30)$$

where  $v_{eff}(\vec{r})$  is defined by equation (2.22). In equation (2.30) the Hamiltonian  $h_{eff}$  is a Hermitian operator, hence  $\varepsilon_{ij}$  is a Hermitian matrix which can be diagonalized by unitary transformation, which leads to the Kohn-Sham equations:

$$\left[ -\frac{1}{2}\nabla^2 + v_{eff}(\vec{r}) \right] \psi_i = \varepsilon_i \psi_i \quad (2.31)$$

Equation (2.31) (or equation (2.30)) is the central equation in the application of density functional theory. These equations are usually solved by self-consistent methods which can be represented by the flow-chart in Figure 6.

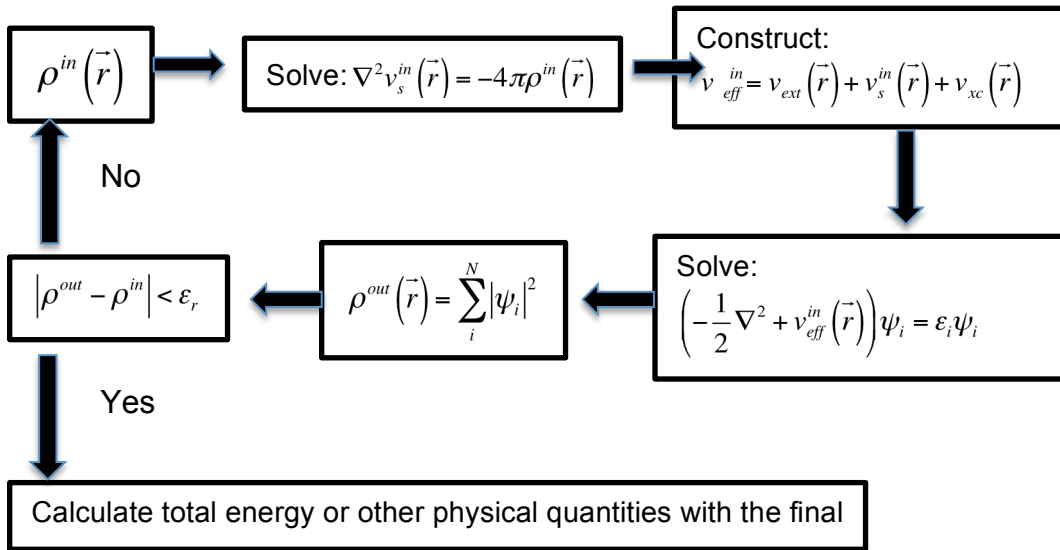


Figure 6: Kohn Sham self-consistent loop.

The solution of Kohn-Sham equation is in principle exact, but as can be seen from the above discussion of the Kohn-Sham procedure, it does not give any prescription for obtaining the exchange-correlation functionals. Depending on the system at hand,

different levels of approximations were made to deal with this functional. In the following we will describe the local and generalized density approximations to these functionals.

#### 2.1.4 Approximations to the Exchange Correlation Functional

The well-known approximations to  $E_{xc}[\rho]$  are the local density approximation (LDA) and the generalized-gradient approximation (GGA). We describe briefly below the underlying concepts of each approximation. Later on we will also describe hybrid density functions which is closely tied to this work.

Within LDA  $E_{xc}[\rho]$  is constructed based on the assumption that the exchange correlation energy per electron  $\varepsilon_{xc}(\rho)$  at point  $\vec{r}$  in the electron gas is the same as that of an electron gas with uniform density.  $\varepsilon_{xc}(\rho)$  can be further broken into two parts:

$$\varepsilon_{xc}(\rho) = \varepsilon_x(\rho) + \varepsilon_c(\rho) \quad , \quad (2.32)$$

where  $\varepsilon_x(\rho)$  is the exchange part and  $\varepsilon_c(\rho)$  is the correlation part. For a homogeneous electron gas  $\varepsilon_x(\rho)$  has an analytic form<sup>136</sup> given by

$$\varepsilon_x^{LDA}(\rho) = -C_x \rho^{1/3}(\vec{r}), \quad C_x = \frac{3}{4} \left( \frac{3}{\pi} \right)^{1/3} \quad (2.33)$$

Within LSDA, it can be shown that

$$\varepsilon_x^{LSDA}(\rho_\alpha, \rho_\beta) = 2^{1/3} C_x \left( \left( \rho_\alpha(\vec{r}) \right)^{4/3} + \left( \rho_\beta(\vec{r}) \right)^{4/3} \right), \quad (2.34)$$

where  $\rho_\alpha, \rho_\beta$  respectively denote the electron up spin and down spin densities.<sup>130</sup> LSDA is particularly useful for systems with non-zero net spin and non-collinear spins.

The correlation part  $\varepsilon_c(\rho)$  cannot be derived analytically. However, it has been calculated numerically with high accuracy using quantum Monte Carlo simulations by

Ceperly and Alder.<sup>50</sup> These numerical values have been fitted to derive analytic forms for  $\varepsilon_c(\rho)$  by Vosko *et al.*<sup>51</sup>

LDA assumes a homogeneous electron gas approximation. However, for systems with rapidly changing densities, this approximation may not be valid. In such situations the first step to improve upon the LDA is to take into account the spatial change in electronic density, i.e. the gradient density,  $\nabla\rho(\vec{r})$ , to take into account the non-homogeneity of the true electron density. This method is named as the gradient expansion approximation (GEA) commonly known as the generalized-gradient approximation (GGA). This can be done by a Taylor series expansion of the exchange-correlation functional,

$$E_{xc}^{GEA}[\rho_\alpha, \rho_\beta] = \int \rho(\vec{r}) \varepsilon_{xc}(\rho_\alpha, \rho_\beta) d\vec{r} + \sum_{\sigma, \sigma'} \int C_{xc}^{\sigma, \sigma'}(\rho_\alpha, \rho_\beta) \frac{\nabla\rho_\alpha}{\rho_\alpha^{2/3}} \frac{\nabla\rho_\beta}{\rho_\beta^{2/3}} d\vec{r} + \dots \quad (2.35)$$

The coefficient  $C_{xc}^{\sigma, \sigma'}$  in equation (2.35) was found to be proportional to  $\frac{1}{\rho^{4/3}}$ .

Unfortunately, GEA did not give a systematic improvement to LDA approximation. The reason is that the exchange correlation interaction was not found physically meaningful in this definition. In addition, higher order corrections of  $\nabla\rho$  are exceedingly difficult to calculate. However, a more sophisticated approach to include the gradient of densities was proposed by Perdew and others<sup>137-139</sup>, the generalized gradient approximation (GGA), which defines the exchange-correlation functional in the following manner,

$$E_{xc}^{GGA}[\rho_\alpha, \rho_\beta] = \int f(\rho_\alpha, \rho_\beta, \nabla\rho_\alpha, \nabla\rho_\beta) d\vec{r} \quad (2.36)$$

In practice,  $E_{xc}^{GGA}$  is divided into its exchange and correlation contributions,

$$E_{xc}^{GGA} = E_x^{GGA} + E_c^{GGA} \quad (2.37)$$

and the approximations for the functionals are usually made individually.

There are several flavors of GGA functionals in literature.<sup>137-139</sup> In this work all DFT (and hybrid DFT calculations which will be discussed below) were based on the PBE96 formulation of the GGA functional.<sup>138</sup>

### *2.1.5 Hybrid Density Functional Theory*

In narrow band systems with localized d and f electrons, such as the transition metal, rare-earth and actinide compounds, where strong electron correlations are predominant, DFT does not perform well. This is due in part to the so called 'self-interaction error' (SIE), a term arising from the mean-field coulomb interaction of an electron density with itself, a consequence of the partial cancellation of the Hartree self-repulsion energy by the self-exchange energy.<sup>140</sup> On the other hand, the Hartree-Fock (HF) theory provides an exact treatment of the exchange functional and produces no self-interaction error because the Hartree self-repulsion energy is exactly cancelled by the Fock exchange interaction but it is deficient in describing chemical bonding, neglects the correlation between electrons and represents solids poorly due to the nonlocal nature of the exchange potential.

By combining DFT and Hartree-Fock (HF) theories, the strengths of each could be exploited to obtain a proper description of highly correlated chemical systems while also being computationally inexpensive.<sup>58</sup> This approach led to the design of the Hybrid density functional theory (HYB-DFT)<sup>57, 58, 141</sup>, in which the exchange-correlation functional is represented as a combination of the exact non-local HF exchange with the approximate local DFT exchange and retaining the DFT correlation functional. Hence, the self-interaction error in DFT functional is reduced due to the addition of HF exchange and consequently, significant improvements compared to LDA/GGA in electronic structure properties, for example, band gaps and magnetism of localized d and f electron systems, can be expected.

In its simplest form, a hybrid XC functional,  $E_{xc}^{HYB}$  containing a fraction,  $\lambda$ , of HF exchange is expressed by:

$$E_{xc}^{HYB} = \lambda E_x^{HF} + (1 - \lambda) E_x^{DFT} + E_c^{DFT}$$

where the subscripts x and c denote the exchange and correlation terms, respectively. Several different types of hybrid density functional have been developed over the years. In addition to the B3LYP hybrid functional mentioned previously, other widely used hybrid functionals are the PBE0<sup>142</sup> and HSE<sup>59</sup>. In this work, the hybrid DFT approach that was adopted is known as the exact exchange for correlated electrons (EECE) method. In short the hybrid DFT is implemented only for the f electrons because they dictate the magnetic and electronic properties of UO<sub>2</sub>.

## 2.2 Computational Approach

We have performed regular DFT and hybrid DFT calculations using the WIEN2k<sup>143</sup> code. The regular DFT calculations were performed with the generalized gradient approximation (GGA) to DFT with the Perdew-Burke-Ernzerhof exchange-correlation functional of 96 (PBE96). All hybrid DFT calculations were performed with the PBE96 correlation, 75% PBE96 exchange, and 25% Hartree-Fock exchange (exchange swap used carried out only for the U 5f electrons inside a muffin tin sphere). WIEN2k is a full-potential linearized/augmented plane waves + local orbitals (L/APW + lo method). Full potential in WIEN2k implies no shape approximation to the potential or density and uses DFT for the treatment of electron exchange and correlation. Based on Slater's augmented plane wave (APW) method<sup>144</sup>, the unit cell is divided into non-overlapping atom-centered muffin tin spheres  $S_\alpha$  with radius  $R_{MT}^\alpha$  and an interstitial region  $I$ , where  $\alpha$  is the atomic index. The Kohn-Sham wave function is expanded in terms of atomic-like orbitals inside the muffin tin spheres and plane waves in the interstitial region. Two types

of basis functions are implemented in WIEN2k. These are the LAPW basis functions and APW+lo basis functions, each with local orbitals (LO) extension, which, as will be explain later, is not the same as lo. The difference between the LAPW and APW+lo methods arises from the linearization of the basis functions inside the atomic spheres. We briefly describe the underlying formalism below.<sup>143</sup>

### 2.2.1 Linear Augmented Plane Wave Method: LAPW

In the LAPW method, originally proposed by Anderson<sup>145</sup>, the energy of the radial solution to the Schrödinger equation  $u_l^\alpha(r', E)$  is expanded by performing a Taylor series expansion up to a linear term about a fixed energy  $E_l$ :

$$u_l^\alpha(r', E) = u_l^\alpha(r', E_l) + (E - E_l) \dot{u}_l^\alpha(r', E_l) + O((E - E_l)^2) \quad (2.38)$$

where  $\dot{u}_l^\alpha(r', E_l) = \left. \frac{\partial u_l^\alpha(r', E)}{\partial E} \right|_{E=E_l}$  and  $\vec{r}' = \vec{r} - \vec{r}_\alpha$ , with  $\vec{r}_\alpha$  being the position of the atom

$\alpha$  in the unit cell.

The LAPW basis function is then written as

$$\phi_{\vec{k}_n}(\vec{r}) = \begin{cases} \frac{1}{\sqrt{V}} e^{i\vec{k}_n \cdot \vec{r}} & \vec{r} \in I \\ \sum_{lm} \left[ A_{lm, \vec{k}_n} u_l^\alpha(r', E_l) + B_{lm, \vec{k}_n} \dot{u}_l^\alpha(r', E_l) \right] Y_{lm}(\hat{r}') & r' < R_{MT}^\alpha \end{cases} \quad (2.39)$$

where  $Y_{lm}$  are the spherical harmonics,  $V$  is the volume of the unit cell, and  $\vec{k}_n = \vec{k} + \vec{K}_n$  with  $\vec{k}$  being the wave vector in the first Brillouin zone and  $\vec{K}_n$  being the reciprocal lattice vectors. The expansion coefficients  $A_{lm, \vec{k}_n}$  and  $B_{lm, \vec{k}_n}$ , which are functions of  $\vec{k}_n$ , are obtained by requiring the value and slope of the basis function inside the sphere to match

the plane wave at the boundary of the sphere, where a particular energy  $E_l$  is chosen for each  $l$ . In certain materials, it is difficult to find a single  $E_l$  that will provide a good description for atoms with a high-lying core state (semi-core state) and a high-lying valence state that have different principal quantum numbers  $n$  but the same orbital quantum number  $l$ . For this, another type of basis function, known as a local orbital (LO), is added to the LAPW basis function.<sup>146</sup>

An LO (which is  $\vec{k}_n$ -independent) consists of a linear combination of two radial functions at two different energies  $E_{1,l}$  and  $E_{2,l}$  and one energy derivative at one of these energies and is given by

$$\phi_{LAPW}^{LO}(\vec{r}) = \begin{cases} 0 & \vec{r} \in I \\ \left[ A_{lm}^{LO} u_l^\alpha(r', E_{1,l}) + B_{lm}^{LO} u_l^\alpha(r', E_{2,l}) + C_{lm}^{LO} \dot{u}_l^\alpha(r', E_{1,l}) \right] Y_{lm}(\hat{r}') & r' < R_{MT}^\alpha \end{cases} \quad (2.40)$$

The coefficients  $A_{lm}^{LO}$ ,  $B_{lm}^{LO}$ , and  $C_{lm}^{LO}$  are obtained by requiring the value and derivative of the LO to vanish at the boundary of the sphere and is normalized.

### 2.2.2 Augmented Plane Wave Plus lo Method: APW+lo

It was shown by Sjöstedt, Nordström, and Singh<sup>146</sup> that the standard method in LAPW requiring that the plane waves of the interstitial region match in value and slope to the solution inside the muffin tin sphere is not the most resourceful way to linearize Slater's APW. Therefore, they proposed the APW+lo method, for which linearization is achieved by adding a local orbital (lo) to Slater's original APW. To clarify, the APW+lo basis function is defined in two parts. The first part of the APW+lo basis function is Slater's original APW:

$$\phi_{\vec{k}_n}(\vec{r}) = \begin{cases} \frac{1}{\sqrt{V}} e^{i\vec{k}_n \cdot \vec{r}} & \vec{r} \in I \\ \sum_{lm} a_{lm, \vec{k}_n} u_l^\alpha(r', E_l) Y_{lm}(\hat{r}') & r' < R_{MT}^\alpha \end{cases} \quad (2.41)$$

where  $a_{lm, \vec{k}_n}$  are obtained by matching only the value of the inside the sphere with the plane wave outside the sphere at the surface of the sphere. The second part of the APW+lo basis function is the lo part which is defined as:

$$\phi^{lo}(\vec{r}) = \begin{cases} 0 & \vec{r} \in I \\ \left[ b_{lm} u_l^\alpha(r', E_l) + c_{lm} u_l^\alpha(r', E_l) \right] Y_{lm}(\hat{r}') & r' < R_{MT}^\alpha \end{cases} \quad (2.42)$$

Unlike the LAPW basis function inside the sphere given in equation (2.40), the coefficients  $b_{lm}$  and  $c_{lm}$  in the expression for  $\phi^{lo}$  does not depend on the wave vector  $\vec{k}_n$ . In this case,  $b_{lm}$  and  $c_{lm}$  are obtained by requiring that lo vanishes at the boundary of the sphere and is normalized. Just like the LAPW basis function, it is not possible in the APW+lo method to use the same  $E_l$  to treat two states with different principal quantum numbers  $n$  but with the same orbital quantum number  $l$  inside the sphere. Again, the problem is remedied by adding local orbitals (LO), which consist of a linear combination of two radial functions at two different energies. In the APW+lo method LO is defined as follows:

$$\phi_{APW+lo}^{LO}(\vec{r}) = \begin{cases} 0 & \vec{r} \in I \\ \left[ a_{lm}^{LO} u_l^\alpha(r', E_{1,l}) + b_{lm}^{LO} u_l^\alpha(r', E_{2,l}) \right] Y_{lm}(\hat{r}') & r' < R_{MT}^\alpha \end{cases} \quad (2.43)$$

The coefficients  $\vec{k}_n$ -independent coefficients  $a_{lm}^{LO}$  and  $b_{lm}^{LO}$  are obtained by requiring the value of the LO to vanish at the boundary of the sphere and is normalized. It

should be noted in equation (2.44) that unlike the LO for the LAPW basis in equation (2.41), equation (2.44) contains no derivatives of the radial functions.

For a given interstitial plane wave cut-off, the dimension of the APW+lo Hamiltonian matrix is slightly larger than LAPW, but APW+lo converges faster and reaches the same accuracy compared to LAPW with a smaller plane wave cut-off, *i.e.*, the additional numerical effort is greatly compensated for by faster convergence with respect to the number of basis functions. Madsen, Blaha, Schwarz, Sjöstedt, and Nordström<sup>147</sup> have demonstrated that using a mixed basis set of LAPW/APW+lo for different angular momentum,  $l$  of radial functions centered on the same atom yields a particularly accurate and efficient description. For our group's work on Pu metal for example, we have used APW+lo basis (with the addition of LOs to appropriate semi-core and valence states) to describe all s, p, d, and f ( $l=0, 1, 2, 3$ ) states and LAPW basis to describe all higher angular momentum states in the expansion of the wave function.

### *2.2.3 Full Potential and Spin-Orbit Interaction*

The “muffin-tin” approximation used in early band structure calculations approximated the potential inside the muffin tin sphere to be spherically symmetric and, in many implementations, the interstitial potential was set constant. This is known as the “shape approximation” to the potential (and subsequently the charge density). WIEN2k relaxes the shape approximation by adding non-spherical terms to the potential inside the muffin-tin and expanding the potential in the interstitial region as a Fourier series, and therefore makes no “shape approximation” to the potential or charge density. Core states are treated at the fully relativistic level while valence states are treated at the scalar (no spin-orbit interaction) or fully relativistic level (spin-orbit interaction included). Spin-orbit effects are treated perturbatively using the scalar relativistic eigenstates as the basis

within a given energy window, where all eigenstates with energies below a chosen energy cutoff were included, with the so-called  $p_{1/2}$  extension, which accounts for the finite character of the wave function at the nucleus for the  $p_{1/2}$  state.<sup>148</sup>

### Chapter 3

#### Hybrid Density Functional Study of the UO<sub>2</sub> (111) and (110) Surfaces

This chapter is focused on the hybrid DFT description of the UO<sub>2</sub> (111) and (110) surface properties. The (111) and (110) surfaces were employed because they are the most stable surfaces for FCC metals and UO<sub>2</sub> has an FCC structure. The surface properties of interest are the total energies, incremental energies, surface energies, and work function. The convergence of the surface properties will be gauged via the variation with respect to the number of UO<sub>2</sub> formula units. We will also exam the electronic properties such as the electronic band gap, the localized nature of the U 5f electronic states, and the U 5f – O 2p hybridizations. Due to the importance of spin-orbit coupling in the actinides, calculations were performed with the inclusion of spin-orbit coupling. Convergence could not be achieved for the scalar relativistic calculations (i.e. non spin-orbit coupling calculations (NSO)). The reader is referred to Appendix A for the summary of NSO results. It can be seen that NSO UO<sub>2</sub> (110) and (111) total slab energies  $E_{tot}(N)$  show a good trend and convergence in Figure 25 in Appendix A. However, no convergence is seen for the slab incremental energy  $\Delta E_N$ , surface energy  $\gamma$ , work function  $\Phi$ , and the electronic band gap  $\Delta_{gap}(N)$  (Appendix A). This reiterates the importance of including SOC into UO<sub>2</sub> surface calculations.

The remainder of this chapter is organized as follows. First, we will elucidate the computational parameters, followed by the construction of the surface slab models. Then the results and discussions will be presented. Furthermore our results will be compared to past theoretical and experimental data.

### 3.1 Computational Details

The all-electron hybrid DFT-GGA calculations were based on the full-potential (linearized) augmented plane-wave plus local basis (FP-L/APW+lo) method as implemented in the WIEN2k code.<sup>143</sup> The parameters for the calculations are as follows. The wave functions in the muffin tin spheres were expanded up to  $l_{\max} = 10$ . The radii of the muffin tin spheres were  $R_{MT}(U) = 2.3 \text{ a.u.}$  for U and  $R_{MT}(O) = 1.6 \text{ a.u.}$  for O. The quality of the APW+lo basis set was determined by  $R_{MT}^{\min} K_{\max} = 8.0$ , where  $R_{MT}^{\min}$  is the smallest muffin-tin sphere and  $K_{\max}$  is the truncation of the modulus of the reciprocal lattice vectors. In the WIEN2k implementation of hybrid DFT<sup>149, 150</sup>, a fraction,  $\alpha$ , of DFT exchange is replaced by Fock exchange but only to a restricted subspace formed by the correlated electrons, which in this work are the U 5f electrons. Following the recommendation in previous literature, we used  $\alpha = 25\%$ , though in principle, one can use a larger value.<sup>71</sup> Spin-orbit coupling was included via a second variational method, where the scalar relativistic eigenstates with energies below 5 Ry were used as basis functions. Relativistic  $p_{1/2}$  orbitals were also included to account for the finite character of the wave functions at the nucleus.

### 3.2 Bulk properties

Bulk  $\text{UO}_2$  has a  $\text{CaF}_2$  structure. The bulk structure is constructed by transforming the cubic unit cell,  $(a \times a \times a)$ , into a tetragonal unit cell,  $\left(\frac{a}{\sqrt{2}} \times \frac{a}{\sqrt{2}} \times a\right)$ , where  $a$  is the lattice constant. This work has already been published in Li, *et al.*<sup>71</sup> but before starting the surface calculations some bulk calculations were performed to verify their validity. In this work we verified the lattice constant and bulk modulus with an antiferromagnetic

arrangement. As an example we depict in Figure 7 the optimized crystal volume with the inclusion of spin-orbit coupling. The computed data was fitted to the Murnaghan equation of state (EOS) given by

$$E(V) = E_0 + \frac{B_0 V}{B_0'} \left[ \frac{(V_0/V)^{B_0}}{B_0' - 1} + 1 \right] - \frac{V_0 B_0}{B_0' - 1} \quad (3.1)$$

where  $E$  and  $V$  is the total energy and volume respectively,  $E_0$  and  $V_0$  is the equilibrium total energy and equilibrium volume respectively,  $B_0$  is the bulk modulus computed at the equilibrium volume, and  $B_0'$  is the pressure derivative of the bulk modulus computed at the equilibrium.  $B_0$  and  $B_0'$  are defined as:

$$B_0 = -V \left. \frac{dP}{dV} \right|_{V=V_0}, \quad B_0' = \left. \frac{dB}{dP} \right|_{V=V_0}$$

From equation (3.1) we obtained the pressure as  $P(V) = -\frac{dE}{dV}$ .

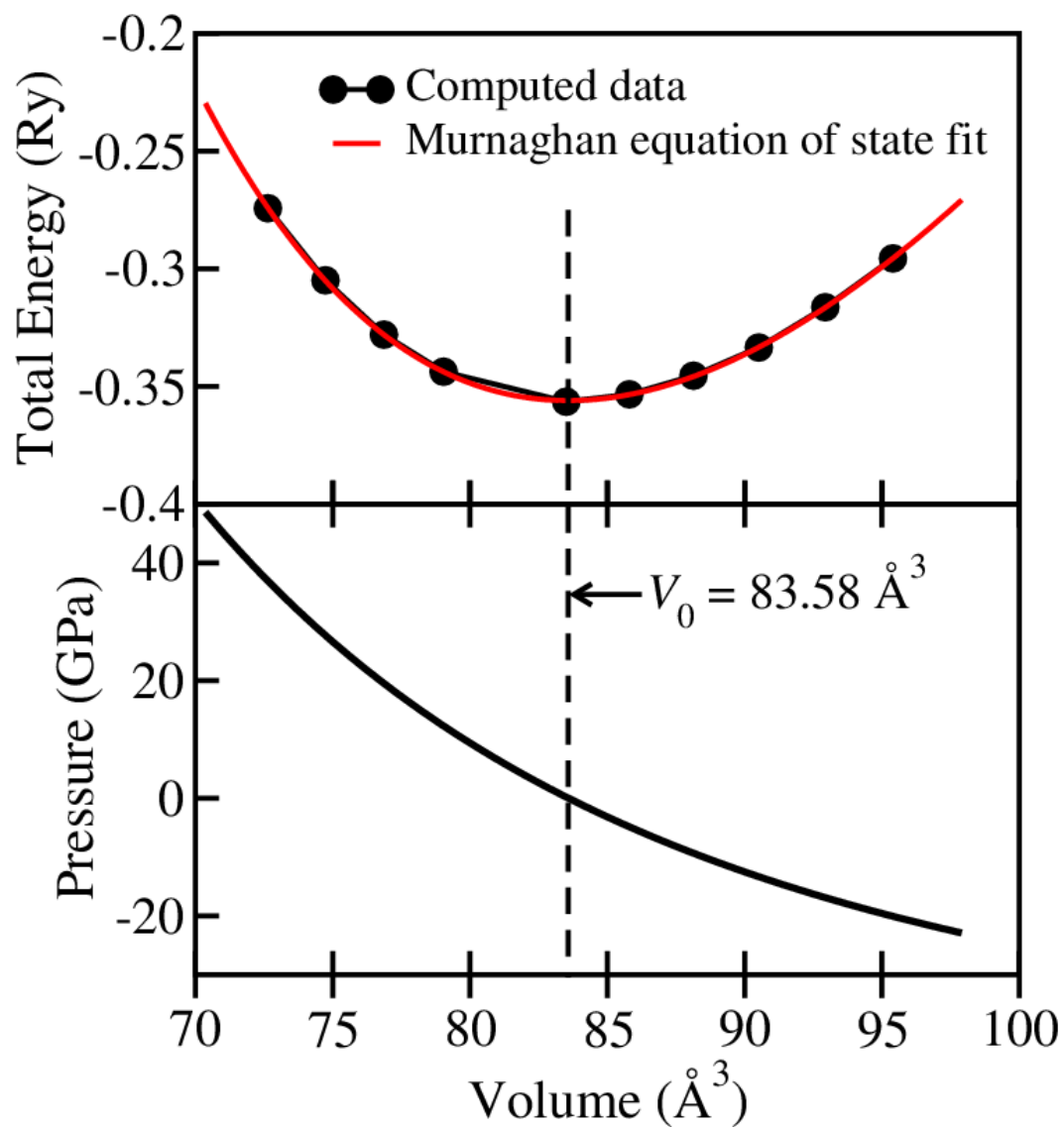


Figure 7: Energy versus Volume optimization Hybrid DFT SOC calculations. The P-V plot was obtained from the Murnaghan EOS. The equilibrium volume is  $V_0 = 83.58 \text{ \AA}^3$ .

Clearly the equilibrium volume obtained from the EOS fit is  $V_0 = 83.58 \text{ \AA}^3$ . This yields an equilibrium lattice constant  $a_0 \equiv (2V_0)^{1/3} = 5.507 \text{ \AA}$ . This lattice constant is in agreement with previous calculation by Li, *et al.*<sup>71</sup> (5.507 \AA) and the experimental data by Schoenes<sup>45</sup> (5.470 \AA). Similarly the zero pressure bulk modulus,  $B_0 = 196 \text{ GPa}$ , is in good agreement with Li, *et al.*<sup>71</sup> ( $B_0 = 199 \text{ GPa}$ ) and fair agreement with Idiri, *et al.*<sup>151</sup> ( $B_0 = 207 \text{ GPa}$ ). As expected the graph at the bottom panel of Figure 7 shows that the equilibrium volume occurs exactly at zero pressure.

In the formal ionic limit, the U valence is +4 and the O valence is -2, implying a U  $5f^2$  valence. Since the properties of elemental actinides and actinide compounds depend significantly on the nature of the 5f electrons in  $\text{UO}_2$ . In addition we are interested in the degree of hybridization between O valence and U valence. In Figure 8, we depict the single particle Kohn-Sham electronic Density of States (DOS) and energy dispersion (i.e., band structure). Clearly, the valence states close to the Fermi level are dominated by U 5f states. While the lower sub-bands are dominated by the O 2p states, with the U 6d states delocalized over the relevant valence region. The valence bands near the Fermi level are sufficiently flat, implying that the U 5f states are fairly localized; this can be seen in the DOS curve for the U 5f states. The nature of the bands confirm experimental assertions that bulk  $\text{UO}_2$  is a Mott-Hubbard type insulator since the band gap is associated with a U 5f  $\rightarrow$  5f transition and the valence O 2p band lies below the U 5f band. The computed band gap from the band structure is 1.4 eV and it is an indirect gap ( $\Gamma \rightarrow R$ ). This is smaller than the experimental band gap of 2.1 eV. In principle, we could achieve a similar band gap by using a higher fraction of Hartree-Fock exchange, say 40% (see Ma *et al.*<sup>71</sup>). Therefore, we deem the presence of the gap to be more important than

the actual value of the gap. Past theoretical studies have suggested that the U–O bond is partially ionic and partially covalent, though their respective degrees are not clearly known.<sup>84</sup> From Figure 8, it can be seen that the overlap, although small, between the U 5f, 6d states and the O 2p states is a signature of covalency.

To further probe the degree of ionicity or covalency in the U–O chemical bond, we computed the difference charge density  $\Delta\rho(r)$ :

$$\Delta\rho(r) = \rho(UO_2) - \rho(U) - \rho(O_2) \quad (3.2)$$

where  $\rho(UO_2)$  is the total electron charge density of  $UO_2$ ,  $\rho(U)$  is the total charge density of the U atoms (the anti-ferromagnetic spin structure was preserved), and  $\rho(O_2)$  is the total charge density of the two O atoms. We must point out that  $\rho(UO_2)$  and  $\rho(U)$  were computed with hybrid DFT (since the Fock exchange was applied only to the U 5f electrons), while  $\rho(O_2)$  was computed with regular GGA-DFT. Furthermore in the computation of  $\rho(U)$  and  $\rho(O_2)$ , the U and O atoms were fixed at exactly the same positions as they were in the  $UO_2$  crystal.

The difference charge density plot is shown in Figure 9. We employed the visualization software VESTA to generate the picture.<sup>152</sup> Regions of excess charge around O can be seen, implying charge transfer from U to O. Around the U ions, regions of partial excess charge and partial charge depletion can be seen. The shape of the density around O is clearly a p-like character, while that of U indicates an admixture of U 5f and 6d states. Overall, the plot indicates there is very little charge density between the atoms. Thus the U–O chemical bond is significantly ionic in character, consistent with the observations in the electronic DOS and band structure.

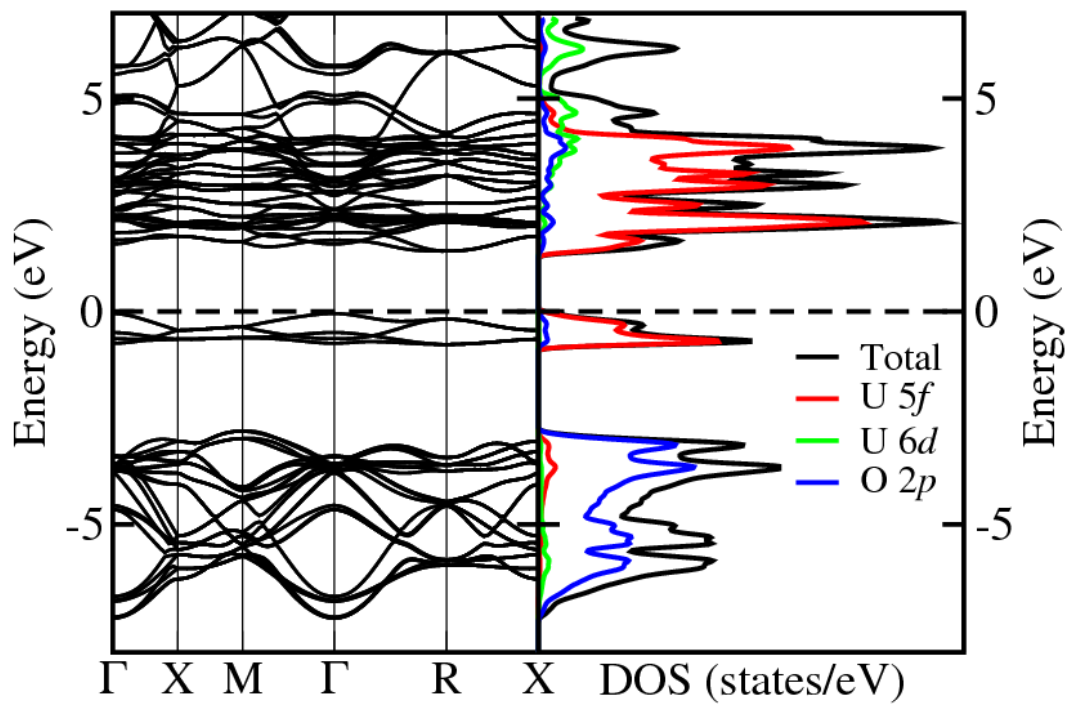


Figure 8: Electronic density of states and band structure of the bulk UO<sub>2</sub> crystal. The dash line denotes the Fermi level.

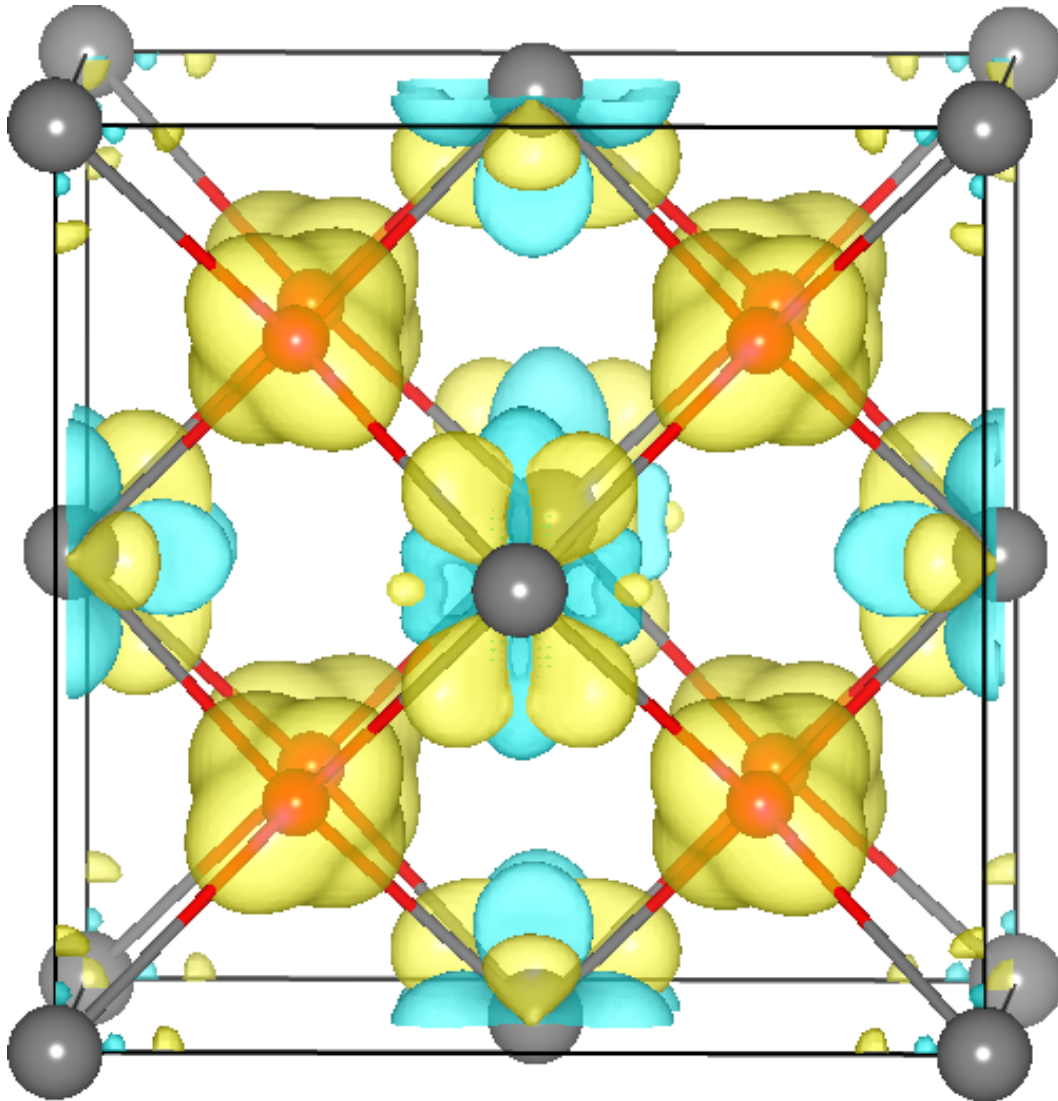


Figure 9: Depiction of the difference charge density plot,  $\Delta\rho(r)$ . The yellow regions denote excess build-up, while the cyan regions denote charge deficiency. The U and O atoms are colored grey and red respectively. The iso-level surface is  $0.02 \text{ e/a.u.}^3$ .

### 3.3 Surface properties

The (110) and (111) surfaces were represented by periodic slabs of  $N$  stacked formula units ( $N=1-7$ ) with a  $1 \times 1$  surface unit cell (cf. Figure 10 (a) and (b) for the (110) and (111) slabs) and a large vacuum region of  $20 \text{ \AA}$  to avoid any interaction between the faces of the slab. The slabs were constructed by cleaving the bulk structure in the proper direction, i.e. the (110) and (111) directions. We must mention that the (110) slabs were non-dipolar, with each formula unit lying in a single layer (cf. Figure 10 (a) and (b) for the (110) slab). For the (111) surface, several slab facial terminations are possible and a net non-zero dipole along the surface may exist based on how the slab faces are terminated. If the net dipole along the surface is not zero, the surface energy will diverge. Following a prescription by Tasker<sup>153</sup>, we terminated the faces of the (111) slab with O; this way the net dipole along the surface direction was zero (cf. Figure 10 (a) and (b) for the (111) surface). Furthermore, test calculations have shown that the anti-ferromagnetic (AFM) U spin arrangements, consisting of alternating spin-up and spin-down U atoms along the  $c$ -axis is the most energetically favorable. Hence all calculations were performed using an AFM spin configuration. The Brillouin zone was sampled by  $k$ -point meshes of  $5 \times 7 \times 1$  for the (110) surface and  $7 \times 7 \times 1$  for the (111) surface. Mesh densities were checked to ensure total energies were sufficiently accurate. The total energy and charge density convergence criteria were  $0.01 \text{ mRy}$  and  $0.0001$  respectively. Calculations were done with the inclusion of SOC for both surfaces. All slabs were fixed at the bulk positions. Slab relaxations were not performed since recent results by Evarestov *et al.*<sup>96</sup> and Tasker<sup>98</sup> have shown that relaxation effects on the properties of  $\text{UO}_2$  surfaces are quite small.

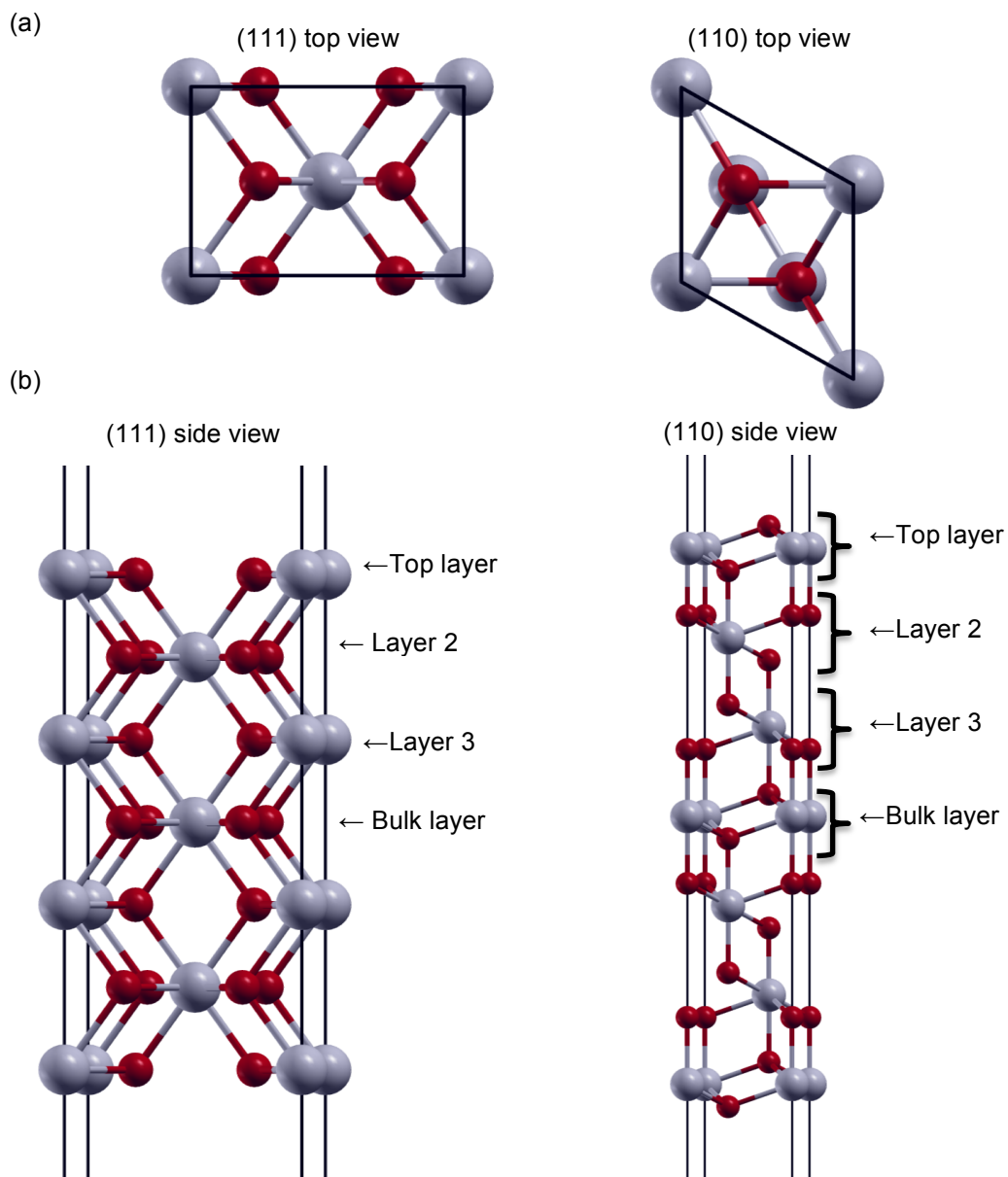


Figure 10: (a) Top view and (b) side view depiction of the (110) and (111) seven layer slabs. The slabs have inversion symmetry about the center of the bulk layer. U atoms are colored grey and O atoms are colored red.

Table 1: Surface properties of  $\text{UO}_2$  (110) SO AFM films.  $E_{tot}(N)$  is the total energy,  $\Delta E_N$  is the slab incremental energy,  $\gamma$  is the surface energy,  $\Phi$  is the work function, and  $\Delta_{gap}$  is the band gap of the  $N$ -layer slab.  $E_{tot}(N)$  and  $\Delta E_N$  have been shifted by +56468 Ry.

N	$E_{tot}(N)$ (Ry/f.u.)	$\Delta E_N$ (Ry)	$\gamma$ (J/m <sup>2</sup> )	$\Phi$ (eV)	$\Delta_{gap}(N)$ (eV)
1	0.7037479		2.04	3.49	0.70
2	0.4557089	0.2076699	1.55 (0.85 <sup>97</sup> )	2.85	1.22
3	0.4110026	0.3215899	1.64 (1.01 <sup>94</sup> , 1.13 <sup>97</sup> )	2.15	0.55
4	0.3862900	0.3121524	1.69 (0.85 <sup>94</sup> , 1.01 <sup>97</sup> )	2.23	0.64
5	0.3718005	0.3138424	1.74 (0.83 <sup>94</sup> , 1.07 <sup>97</sup> )	2.20	0.60
6	0.3618458	0.3120726	1.79 (0.73 <sup>94</sup> , 1.05 <sup>97</sup> )	2.22	0.65
7	0.3549599	0.3136445	1.84	2.21	0.65
Bulk	0.3187097				1.41
Fitted Bulk	0.3031510				
Semi-infinite			1.76		

Table 2: Surface properties of  $\text{UO}_2$  (111) SO AFM films.  $E_{tot}(N)$  is the total energy,  $\Delta E_N$  is the slab incremental energy,  $\gamma$  is the surface energy,  $\Phi$  is the work function, and  $\Delta_{gap}$  is the band gap of the  $N$ -layer slab.  $E_{tot}(N)$  and  $\Delta E_N$  have been shifted by +56468 Ry.

N	$E_{tot}(N)$ (Ry/f.u.)	$\Delta E_N$ (Ry)	$\gamma$ (J/m <sup>2</sup> )	$\Phi$ (eV)	$\Delta_{gap}(N)$ (eV)
1	0.4336196		0.99	3.16	0.65
2	0.3684415	0.3032634	0.91 (0.59 <sup>94</sup> , 0.72 <sup>97</sup> )	3.45	1.10
3	0.3533252	0.3230926	0.98 (0.95 <sup>96</sup> , 0.51 <sup>94</sup> , 0.74 <sup>97</sup> )	3.44	1.00
4	0.3447609	0.3190680	1.03 (0.46 <sup>94</sup> , 0.79 <sup>97</sup> )	3.43	0.85
5	0.3368152	0.3050322	0.95 (0.89 <sup>88</sup> , 0.96 <sup>96</sup> , 0.33 <sup>94</sup> , 0.76 <sup>97</sup> )	3.45	1.01
6	0.3329225	0.3134592	0.95 (0.92 <sup>88</sup> , 0.27 <sup>94</sup> , 0.78 <sup>97</sup> )	3.50	1.18
7	0.3306808	0.3172304	0.98 (0.89 <sup>88</sup> , 0.97 <sup>96</sup> , 0.78-0.76 <sup>95</sup> )	3.50 (3.5-3.6 <sup>95</sup> , 3.5 <sup>93</sup> )	1.18
Bulk	0.3187097				1.41
Fitted Bulk	0.3138877				
Semi-infinite			0.97		

The key properties of the (110) and (111) surfaces are respectively summarized in Table 1 and Table 2. Reported in each table are the total energy  $E_{tot}(N)$  per  $N$ -formula unit for each unit slab, slab incremental energy  $\Delta E_N$ , surface energy  $\gamma$ , work function  $\Phi$ , and the electronic band gap  $\Delta_{gap}(N)$ .

To better facilitate the discussions, we plotted the aforementioned quantities versus  $N$  (Figure 11-Figure 16).

### 3.3.1 Surface Calculations on the (111) and (110) Slabs with SOC

According to Figure 11, the slab total energy per formula unit,  $E_{tot}(N)$ , for each surface decreases with respect to layer thickness  $N$  and exhibits rapid convergence toward the bulk energy. On the basis of  $E_{tot}(N)$ , it is obvious to see the (111) surface is lower in energy, and thus more stable than the (110) surface.

The slab incremental energy,  $\Delta E_N$ , which is depicted in Figure 12, is defined as

$$\Delta E_N = E_{tot}(N) - E_{tot}(N-1) \quad (3.3)$$

$\Delta E_N$  is interpreted as the change in total energy as more “bulk” is added; in the limit of infinite  $N$ ,  $\Delta E_N$  should converge exactly to the bulk total energy. Examining the plot of  $\Delta E_N$  for the (111) surface in Figure 12, there is sufficiently large oscillations up to  $N=5$  and slight weakening thereafter. This is the so-called Quantum Size Effect (QSE), which is the dependence/oscillations of thin film properties on its characteristic geometric dimensions. For the (110) surface, QSE is small as the fluctuations in  $\Delta E_N$  is small for  $N=3$  and beyond.

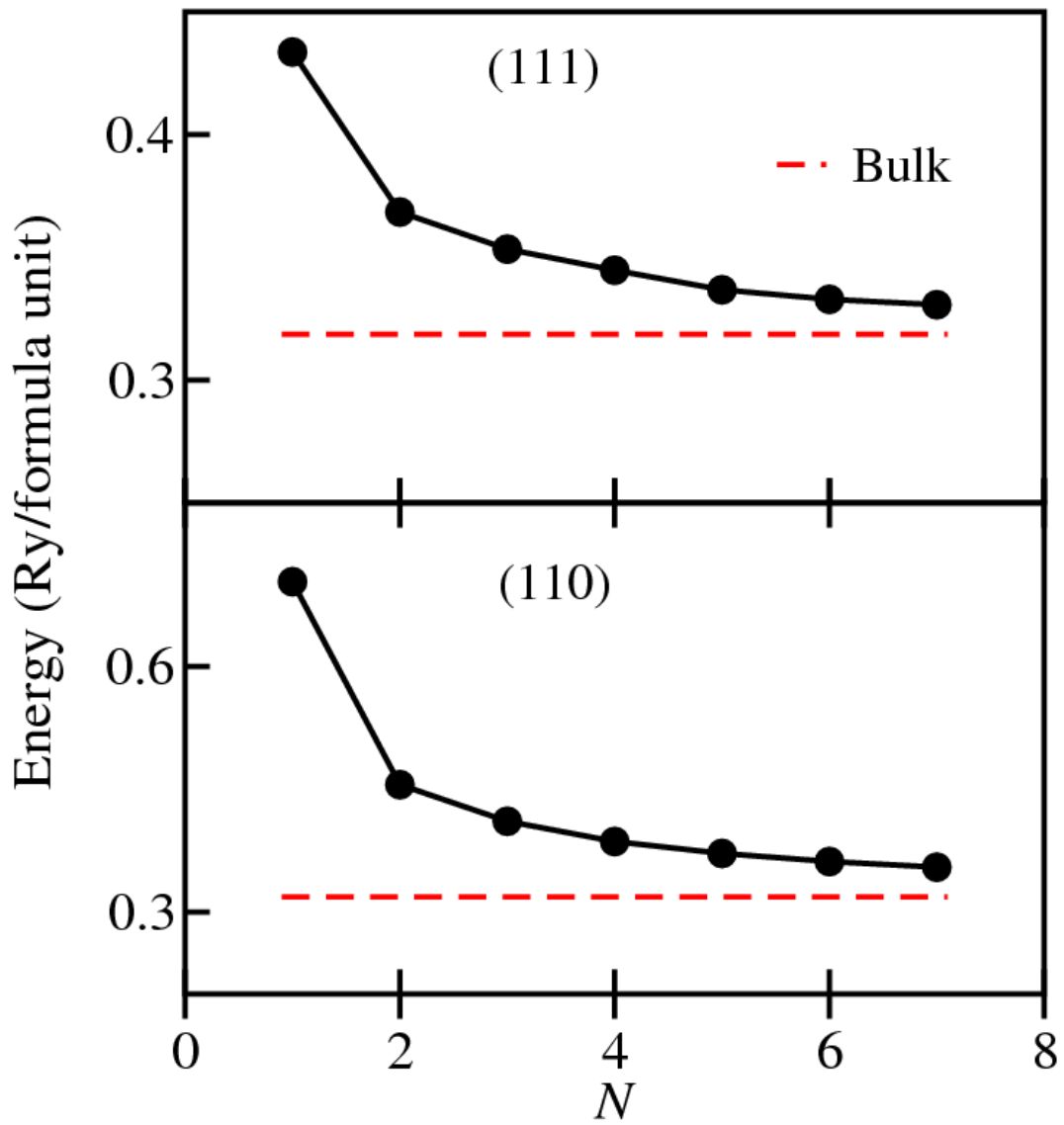


Figure 11: Variations of the energy per formula unit (that is, per  $\text{UO}_2$ ) of the (111) and (110) SO surfaces as a function of slab thickness. The dashed line denotes the energy per formula unit for the bulk crystal.

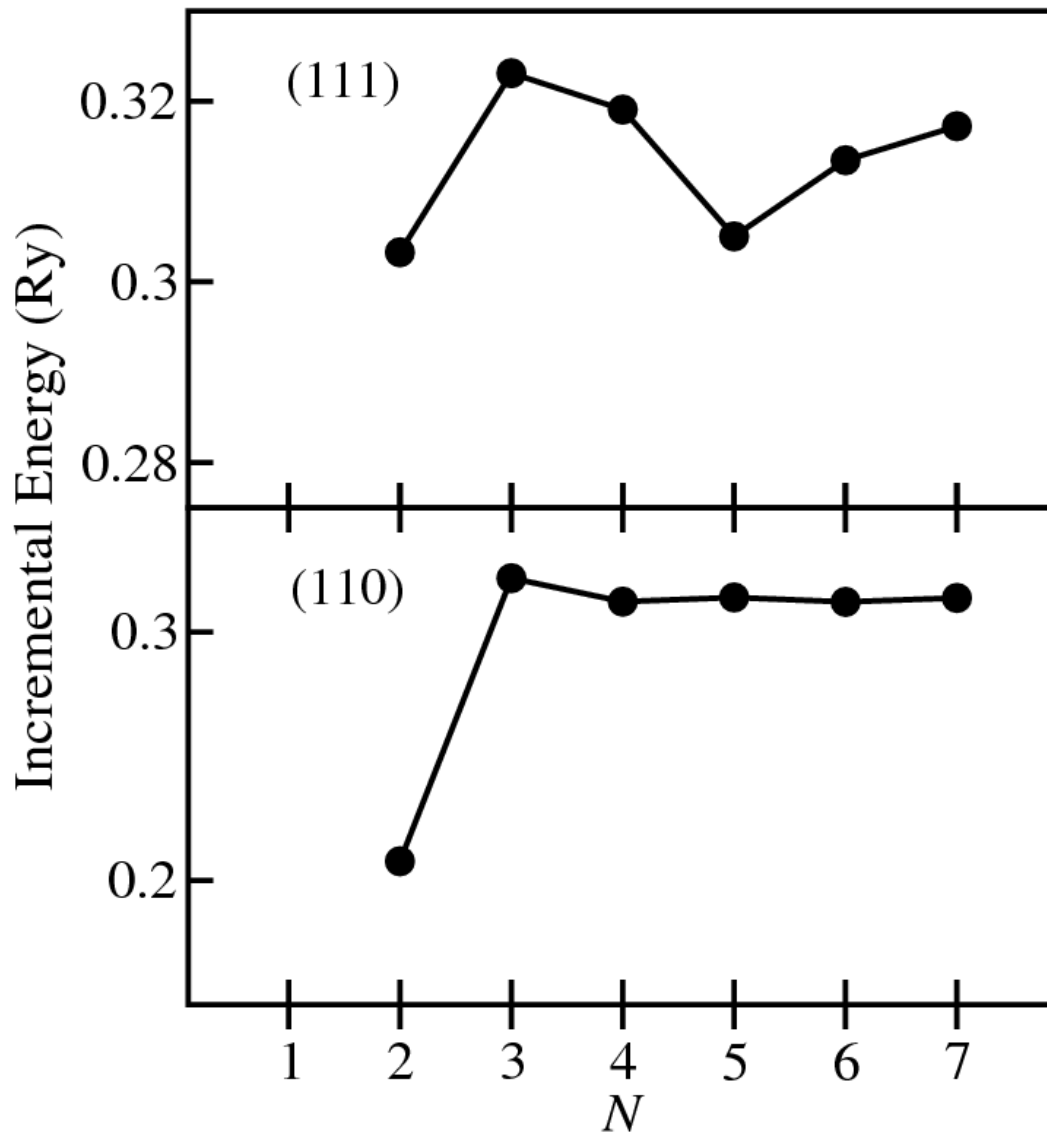


Figure 12: Variations of the incremental energies of the (111) and (110) SO slabs as a function slab thickness.

The surface energy,  $\gamma$ , is one of the most important quantities for characterizing the stability of a surface. Given a set of surfaces along different orientations, the most stable surface is the one with the lowest  $\gamma$ . Formally,  $\gamma$  is defined as the work done to cleave a surface of area  $A$  along a given orientation and it is computed as

$$\gamma = \frac{1}{2A} [E_{tot}(N) - NE_B] \quad (3.4)$$

where  $E_{tot}(N)$  is the total energy of a  $N$ -layer slab and  $E_B$  is the total energy per formula unit of the bulk crystal. The factor  $1/2$  accounts for the two faces of the slab. Equation (3.4) is exact if  $N$  is sufficiently large and the energies required are known to infinite precision. The textbook way of computing  $\gamma$  is to compute  $E_{tot}(N)$  and  $E_B$  separately and substitute them into equation. It has been shown that if the calculations of  $E_{tot}(N)$  and  $E_B$  are not entirely consistent with each other (e.g. the bulk and surface calculations have different plane-wave basis elements and different  $k$ -mesh densities),  $\gamma$  will diverge linearly with increasing  $N$ .<sup>154-156</sup> A more reliable, and perhaps self-consistent, approach for determining  $\gamma$  is as follows: (i) Re-write equation (3.4) as

$$E_{tot}(N) = NE_B + \ell \quad (3.5)$$

where

$$\ell = 2A\gamma \quad (3.6)$$

(ii) Perform slab calculations for different values  $N$  to obtain a set of slab energies  $E_{tot}(N)$ . Finally, a linear least square fit (cf. Figure 13) with  $E_{tot}(N)$  as the dependent variable and  $N$  as the independent variable via equation (3.5) yields  $E_B$  as the slope and  $\ell$  as the intercept on the  $E_{tot}(N)$  axis. In essence, this simple scheme yields a value of  $E_B$  that is internally consistent with slab energies as opposed to using a value of  $E_B$

from a separate bulk calculation. Once the fitted  $E_B$  is obtained,  $\gamma$  is computed for each  $N$  using equation (3.4). Using the value of  $\ell$  from the fit, equation (3.6),  $\gamma = \ell/2A$ , is interpreted as the surface energy of the slab with “semi-infinite thickness.” The scheme outlined above was used to compute the slab surface energies.

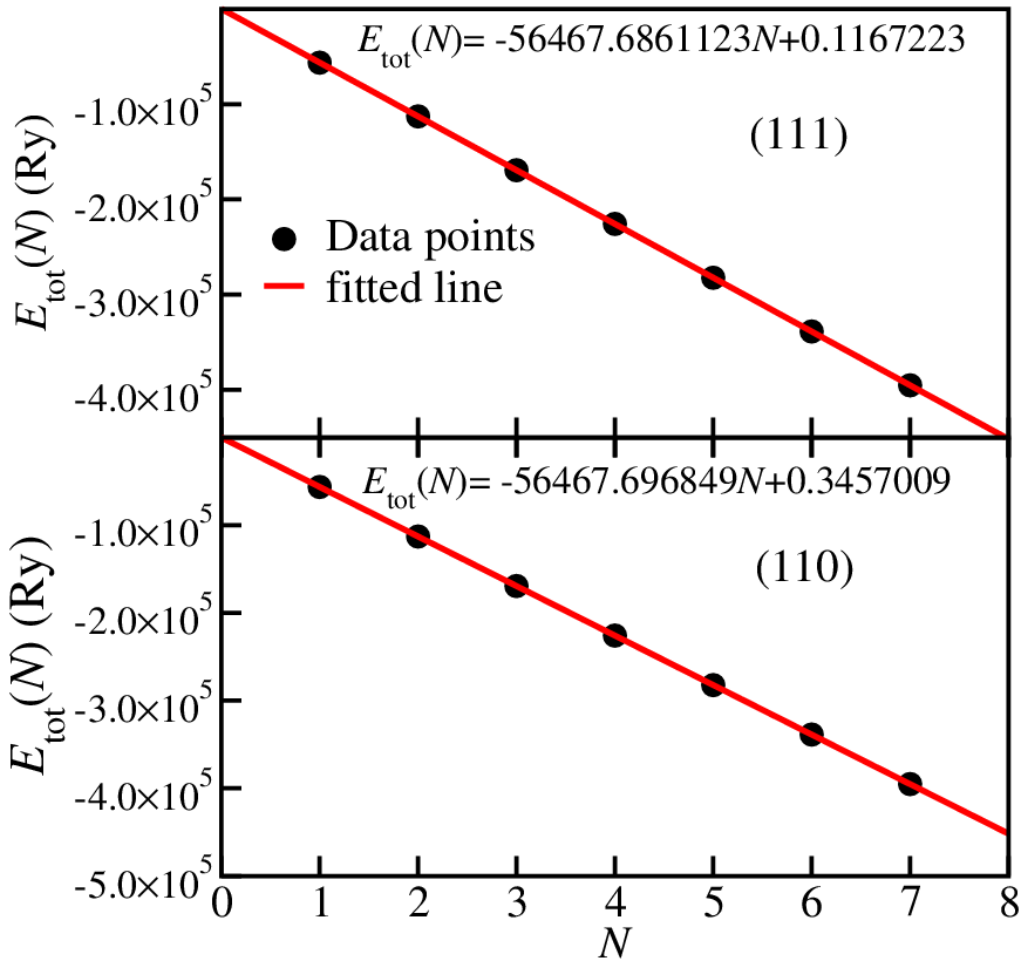


Figure 13: Linear least square fit with  $E_{\text{tot}}(N)$  as the dependent variable and  $N$  as the independent variable via equation (3.5) yields  $E_B$  as the slope and  $\ell$  as the intercept on

the  $E_{\text{tot}}(N)$  axis.

Reported in Table 1 and depicted in the bottom panel of Figure 14, the surface energies for each  $N$ -layer slab for the (110) surface along with the semi-infinite surface energy. The monolayer has the largest surface energy but as more layers are gradually added, the surface energies show convergence. At  $N=5$  and beyond, the variations in successive surface energies is quite small. Thus a slab of at least 5-layer thickness is sufficient for an accurate determination of the (110) surface energy. The semi-infinite surface energy is predicted to be  $1.76 \text{ J/m}^2$  (cf. Table 1). The (111) surface energies are reported in Table 2 and the associated plot in upper panel of Figure 14. The surface energies exhibit very small QSE for the few  $N$ -layer slabs up to  $N=4$ , and the oscillations are further reduced at  $N=5$  and beyond. As was the case for the (110) surface, a slab of at least 5-layer thickness is sufficient for the accurate determination of the surface energy. The semi-infinite surface energy is predicted to be  $0.97 \text{ J/m}^2$ . We have also compared our results to previous work<sup>88, 94-97</sup> in Table 1 and Table 2. For the (110) surface energies in Table 1, we note a disagreement between our results and prior works<sup>94, 97</sup>, particularly the work of Skomurski *et al.*<sup>94</sup>. The source of discrepancy could be due to the fact that (i) DFT-GGA, which cannot describe  $\text{UO}_2$ , was employed by Skomurski *et al.*<sup>94</sup>, while DFT+U was employed by Rák *et al.*<sup>97</sup> and (ii) the authors employed a ferromagnetic magnetic spin-configuration instead of an anti-ferromagnetic spin configurations. Regarding the (111) surface energies in Table 2, we see a good agreement of our results with that of Chaka *et al.*<sup>88</sup> and Evarestov *et al.*<sup>96</sup>, while they disagree with the other results (Skomurski *et al.*<sup>94</sup>, Weck *et al.*<sup>95</sup> and Rák *et al.*<sup>97</sup>). Evarestov *et al.*<sup>96</sup> make a good point that the rather low surface energies calculated by Skomurski *et al.*<sup>94</sup> are due to the fact that the proper bulk energy was not employed.

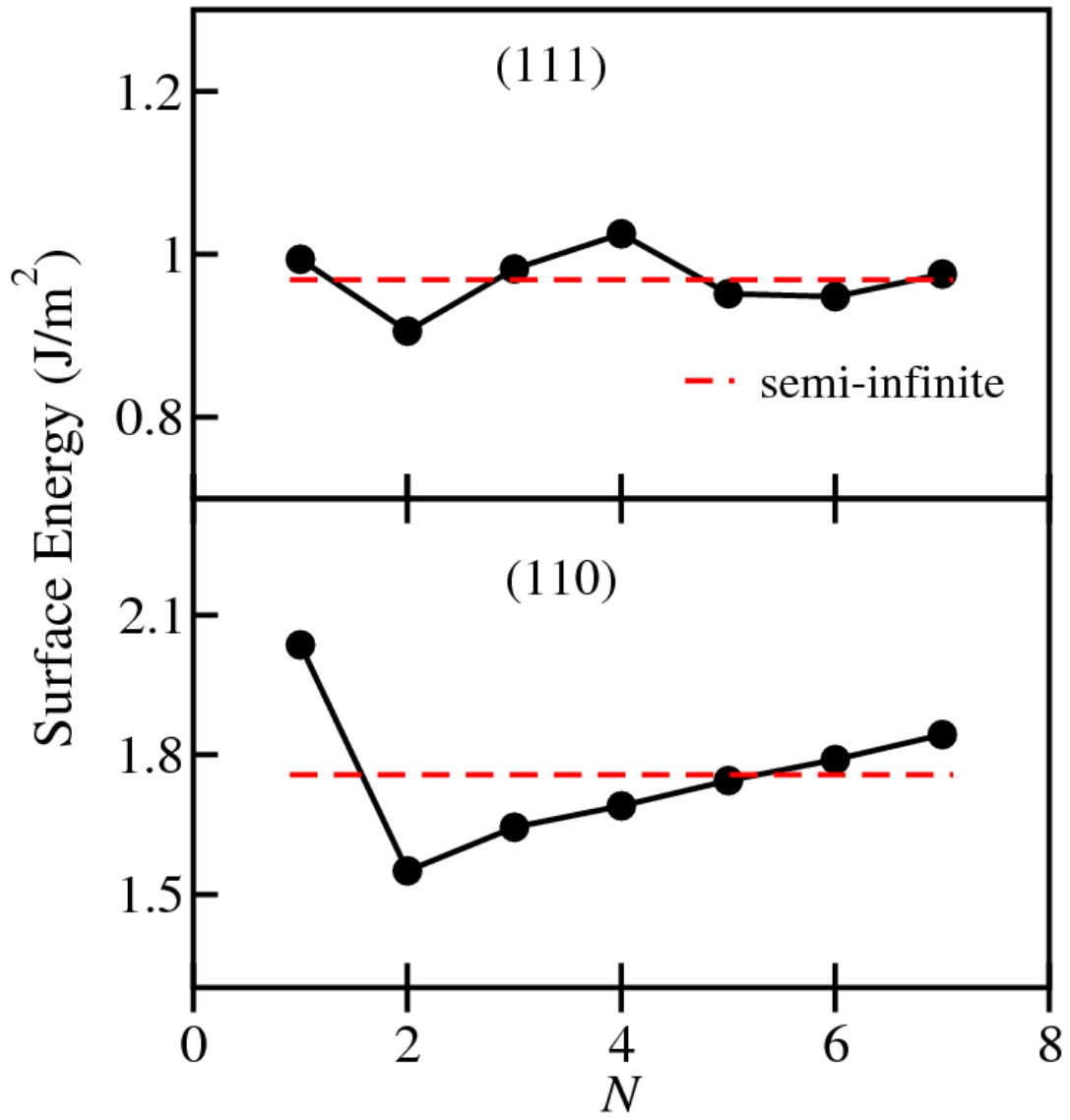


Figure 14: Variations of the surface energies of the (111) and (110) SO slabs as a function of slab thickness. The dashed line denotes the surface energy of a slab of semi-infinite thickness.

The work function,  $\Phi$ , is the smallest energy required to remove an electron deep inside the bulk crystal through the surface and far away from the surface on the microscopic scale but close to the macroscopic scale at temperature of 0 K.  $\Phi$  is computed as

$$\Phi = V_{vacuum} - E_F \quad (3.7)$$

where  $V_{vacuum}$  is the Coulomb electrostatic potential energy in the middle of vacuum and  $E_F$  is the Fermi level. In Table 1 the work functions for the (110) films are listed and the corresponding plot is presented in the bottom panel of Figure 15. Clearly, large QSE can be seen up to  $N=4$  followed by rapid convergence. A close examination of the actual values in Table 1 reveal that for  $N=4$  and beyond the work functions are all within hundredth of eV of each other. For the (111) film (cf. upper panel of Figure 15 and Table 2), a similar picture is seen. The average value of  $\Phi$  for  $N=4$  and beyond is used as the representative value for each surface. The average work function for (110) and (111) surfaces are 2.2 eV and 3.5 eV respectively, with the (111) surface work function being in good agreement with experimental measurements<sup>93</sup> and prior theoretical work.<sup>95</sup> To the best of our knowledge, our work is the first to provide information on the variations in the work function with respect to system size. Intuitively, the work function of (110) surface is expected to be lower than the (111) surface, due to the fact (110) surface is less stable. A low work function implies electrons can easily escape from the bulk region of  $UO_2$ , and react with impurities at the surface. To be more specific, the  $UO_2$  (110) surface will interact more strongly (high surface activity) with common environmental gases such oxygen gas and water than the (111) surface.

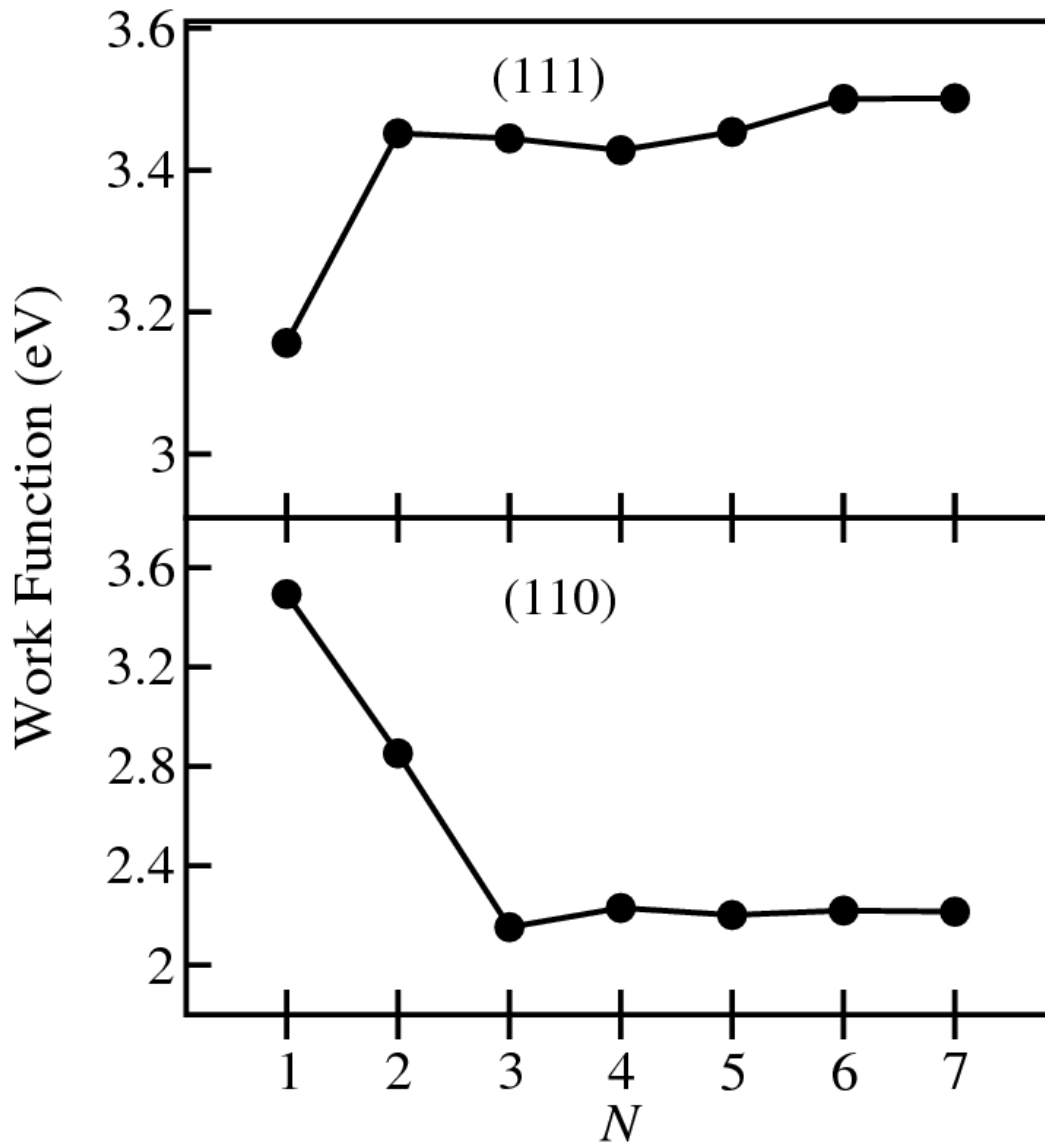


Figure 15: Variations of the electronic work function of the (111) and (110) SO slabs as a function of slab thickness.

The trends in the band gaps for each surface are depicted in Figure 16. It can be seen from the figure that the surface band gaps are smaller than the bulk band gap. This is expected due to incomplete atomic coordination at the surface. For both surfaces, the QSE in gap oscillations is reduced after  $N = 4$ . The estimated band gaps for (110) and (111) surfaces are 0.65 eV and 1.1 eV respectively.

The projected DOS was computed for each layer/formula unit of the thickest slab (seven-layer slab). The localization behavior of the 5f electron states at and away from the surface, retain a Mott-Hubbard insulating behavior. In Figure 17 and Figure 18, the layer-resolved projected density of states is shown for (110) and (111) surfaces respectively. Clearly the top layer plots in Figure 17 and Figure 18 show that the U 5f band becomes narrower and withdrawn from the Fermi level by  $\approx 1$  eV. Thus the U 5f electron states become localized at the surface, resulting in a larger band gap compared to the other layers. The O 2p bands in the top layer exhibit some localization as well. In both figures, we see that the second, third, and bulk layers mimic each other and collectively show the same behavior as the bulk crystal (cf. Figure 8). Except for the relatively small band gaps in comparison to the bulk band gap, we see that the slabs behave as a Mott-Hubbard insulator.

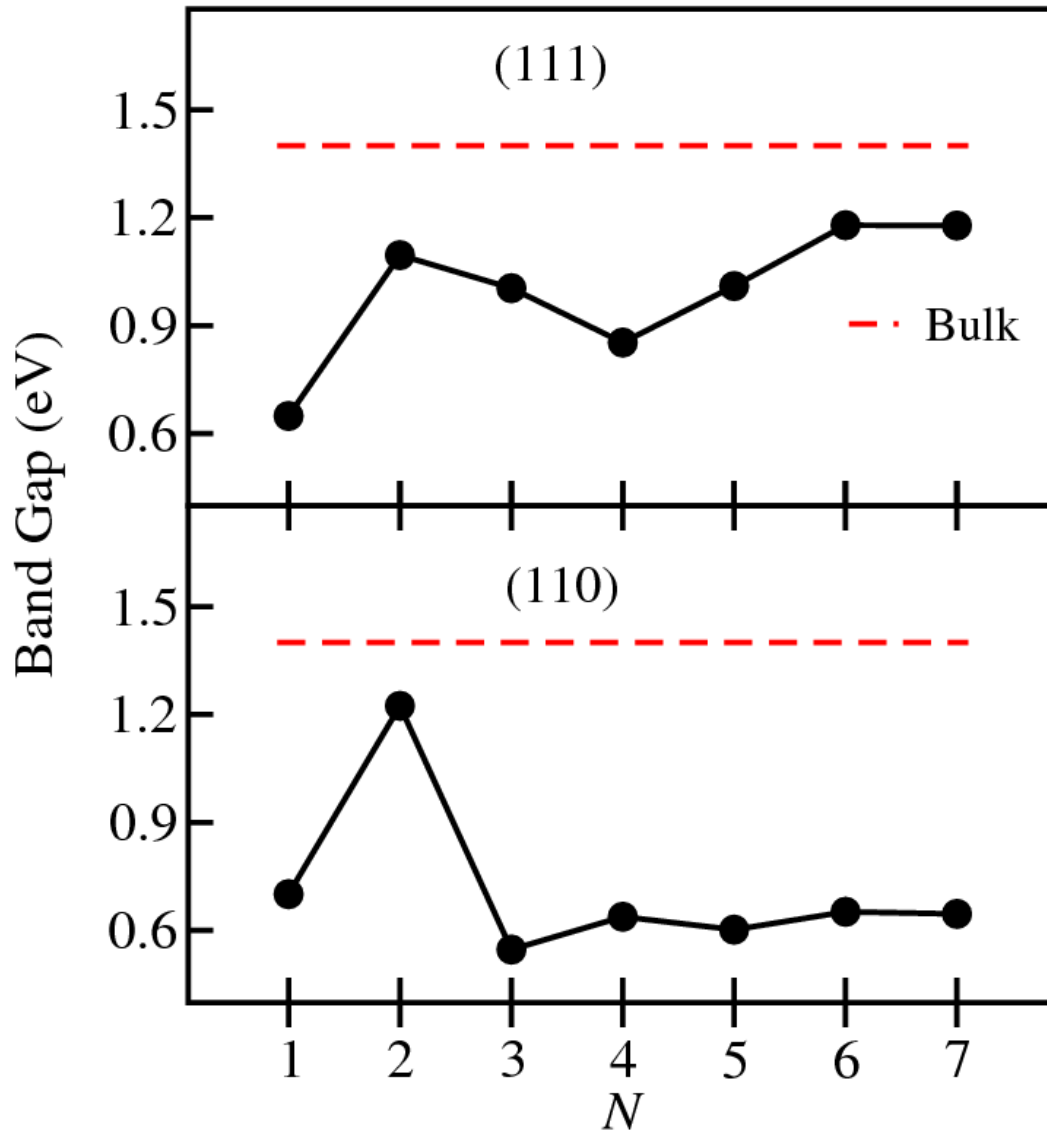


Figure 16: Plots of the SO surface electronic band gaps as a function of slab thickness.

The dashed horizontal line denotes the band gap of the bulk crystal.

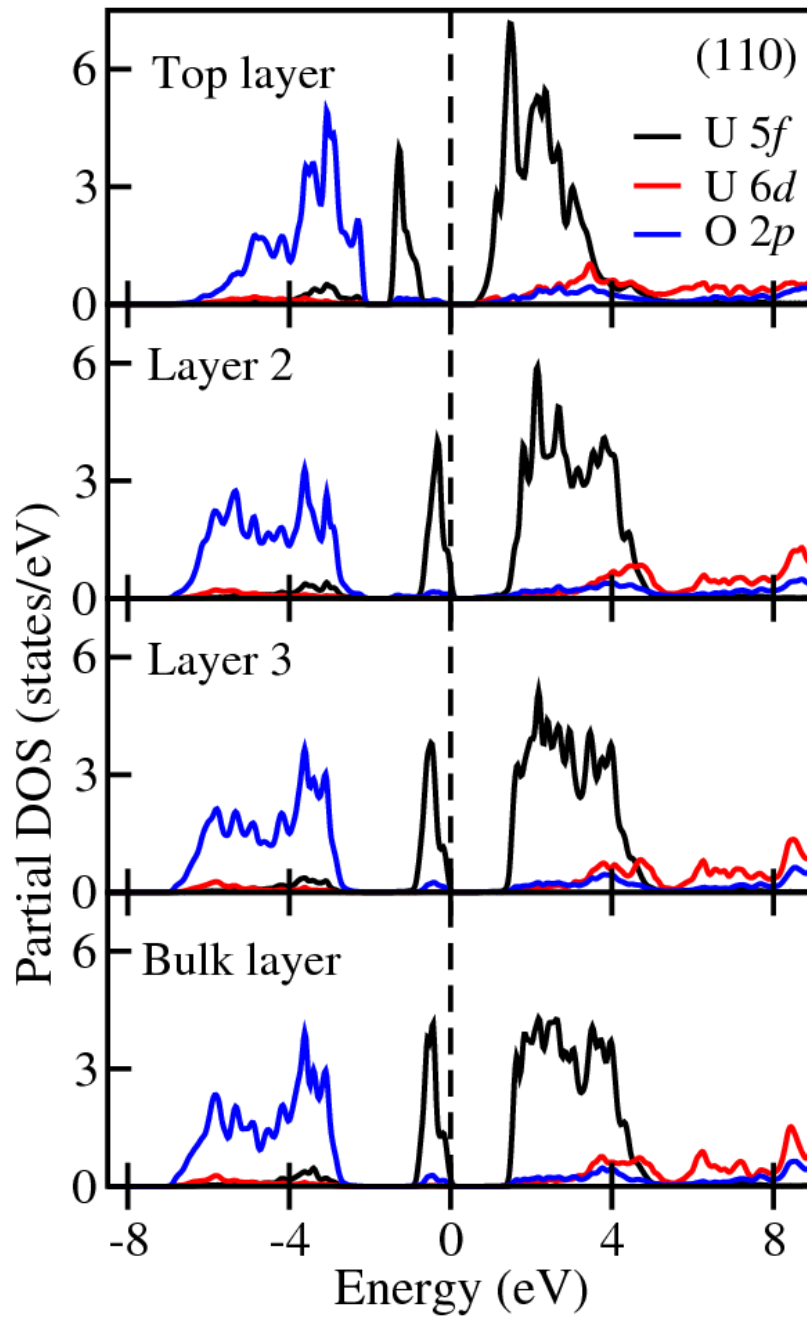


Figure 17: Angular-momentum resolved electronic density of states of each unique O-U-O formula unit of the (110) SO slab with 7 formula units (cf. Figure 10 (b) for the (110) surface).

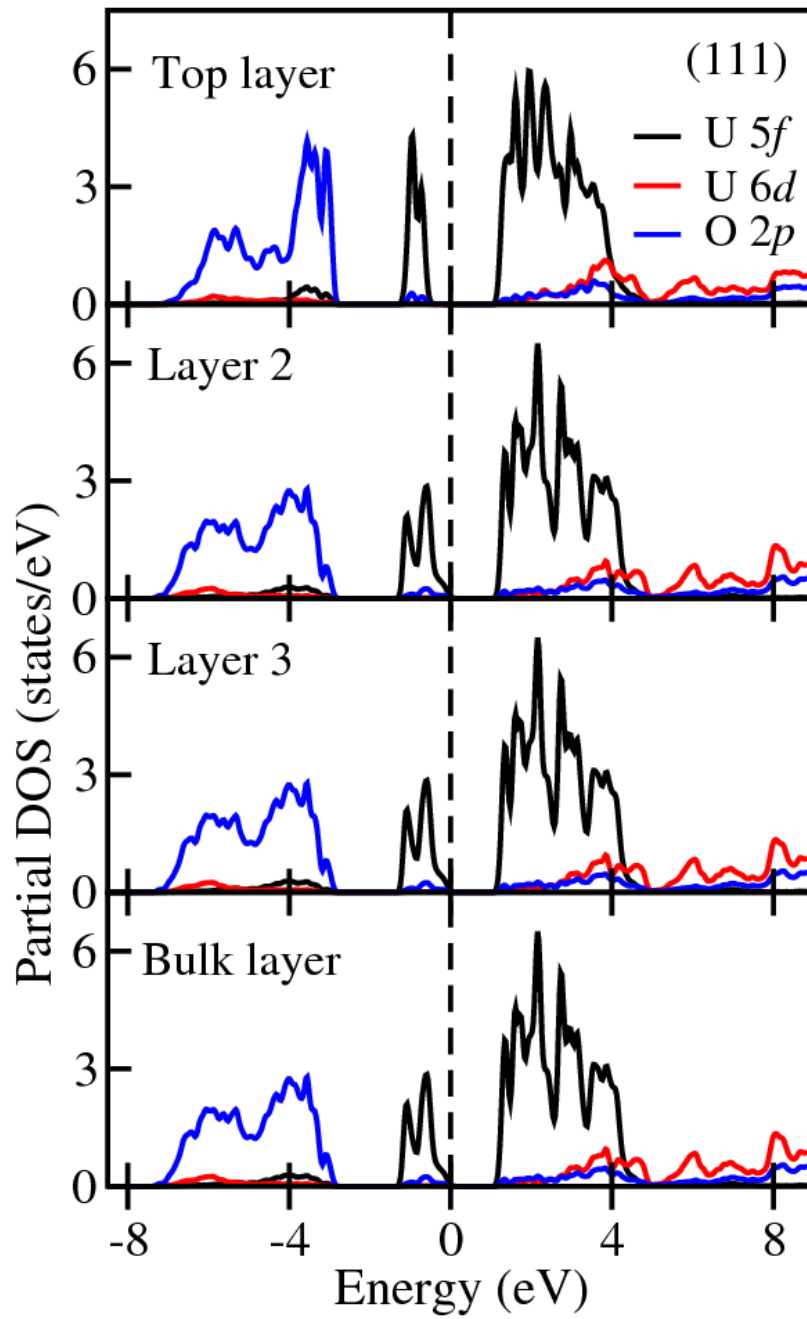


Figure 18: Angular-momentum resolved electronic density of states of each unique O-U-O formula unit of the (111) SO slab with 7 formula units (cf. Figure 10 (b) for the (111) surface).

Chapter 4  
Preliminary Oxygen Adsorption Calculations on the  
UO<sub>2</sub> (111) surface

This chapter is focused on the interaction of atomic oxygen with the UO<sub>2</sub> (111) surface. The (111) surface was used because, as shown in Chapter 3, it is the most stable UO<sub>2</sub> surface. In principle, different surfaces react differently towards the same adsorbate. Hence one can probe the adsorption of the adsorbate with different surfaces to fully access the interaction process. For UO<sub>2</sub> in particular, one has to probe the adsorbate interaction with flat surfaces such as (100), (110), and (111) and stepped-surfaces such as the (211) and (221) surfaces. Unfortunately, limited computational resources did not permit us to extensively probe the adsorbate interaction with the surfaces.

O adsorption on UO<sub>2</sub> (111) is a somewhat simplified version for probing UO<sub>2</sub> surface oxidation. Specifically, the attachment of O to the UO<sub>2</sub> surface stemming from O<sub>2</sub> or H<sub>2</sub>O dissociation is one of several intermediates steps in the UO<sub>2</sub> oxidation process. Our goal here is to use DFT and hybrid DFT to investigate the preferred adsorbate configuration, the nature of the binding of the adsorbate to the surface and the adsorbate-induced changes in the surface structural and electronic properties.

The remainder of this chapter is organized as follows. First, we will describe the computational scheme. As mentioned earlier, these studies are preliminary so we will highlight the key results and discuss them.

#### 4.1 Computational Details

All calculations were performed using WIEN2k.<sup>143</sup> The muffin tin radii ( $R_{MT}$ ) for O and U were 1.0 a.u. and 2.25 a.u. respectively. The  $R_{MT}$  used for the clean surface calculations in Chapter 3 were larger than the ones employed for the adsorption calculations. The reason being, the atoms tend to be closer than usual during the structural relaxation process. Therefore the  $R_{MT}$ 's were chosen to be small enough to avoid the spheres from overlapping during the relaxation process. A 4x4x1 k-point mesh was used to sample the Brillouin zone. The plane wave kinetic energy cutoff for the expansion of the wave function in the interstitial region was determined by  $R_{MT}K_{MAX} = 4$  ( $K_{MAX}^2$  is the plane-wave kinetic energy cutoff in Ry).

The adsorption calculations were carried out using the 5 layer UO<sub>2</sub> (111) surface with a  $\sqrt{3} \times \sqrt{3} - R30^\circ$  surface unit cell. This resulted in an O adsorbate coverage of 1/3 monolayer (ML). Three high symmetry initial adsorption sites we considered: (i) one-fold top site (refer to Figure 19); (ii) two-fold bridge site (refer to Figure 20); (iii) three-fold hollow site (refer to Figure 21) also known as the center site. To preserve inversion symmetry and therefore to avoid the creation of artificial dipoles, the adsorbate was placed on both faces of the slab. To save computational time the clean slab was fully relaxed. Then the adsorbate was initially placed at the fully relaxed slab. The slab atomic positions were then held fixed and only the adsorbate was allowed to relax. All structural relaxations were carried out at the DFT level and the optimized structures were used as an input for a single point hybrid DFT (with 25% HF exchange) run to account for the correlation effects in uranium oxide systems. The relaxations were terminated when the maximum Hellman-Feynman force on each atom along each coordinate direction was less than 2 mRy/a.u.. The adsorption energy per adsorbate was computed as:

$$E_{ads} = \frac{1}{2} [E_{slab} + 2E_{adsorbate} - E_{slab+2adsorbate}],$$

where  $E_{slab}$  is the total energy of the fully optimized clean slab,  $E_{adsorbate}$  is the atomic energy of the adsorbate,  $E_{slab+2adsorbate}$  is the total energy of the fully optimized slab-with-adsorbate. With this definition of the adsorption energy,  $E_{ads} > 0$  implies binding is favorable (i.e. the presence of the adsorbate results in a lower energy state), otherwise it is unstable.  $E_{adsorbate}$  was computed by placing the O atom in a big FCC cell of length 25 Bohr.

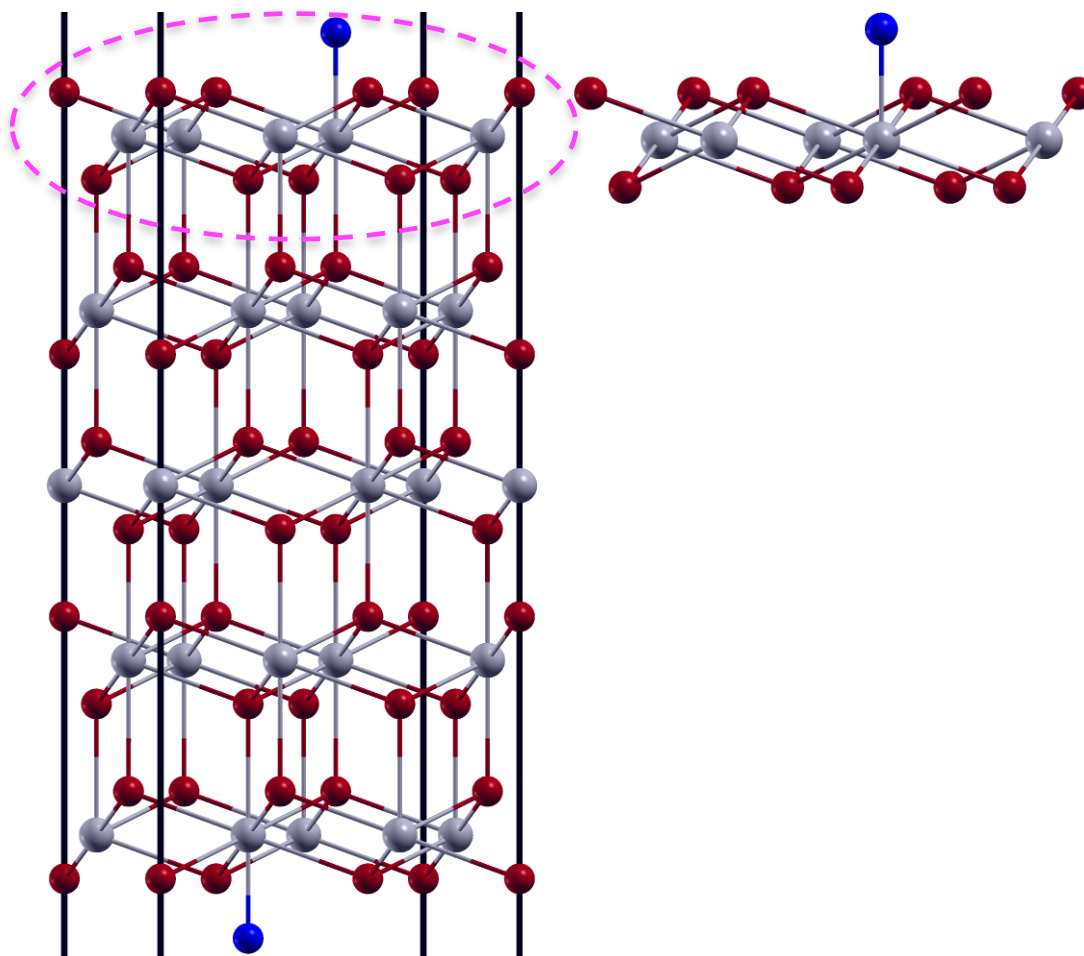


Figure 19: Atomic O initially placed at the top site of the 5 layer  $\text{UO}_2$  (111)

$\sqrt{3} \times \sqrt{3} - R30^\circ$  surface. The O adsorbate coverage is  $1/3$  ML.

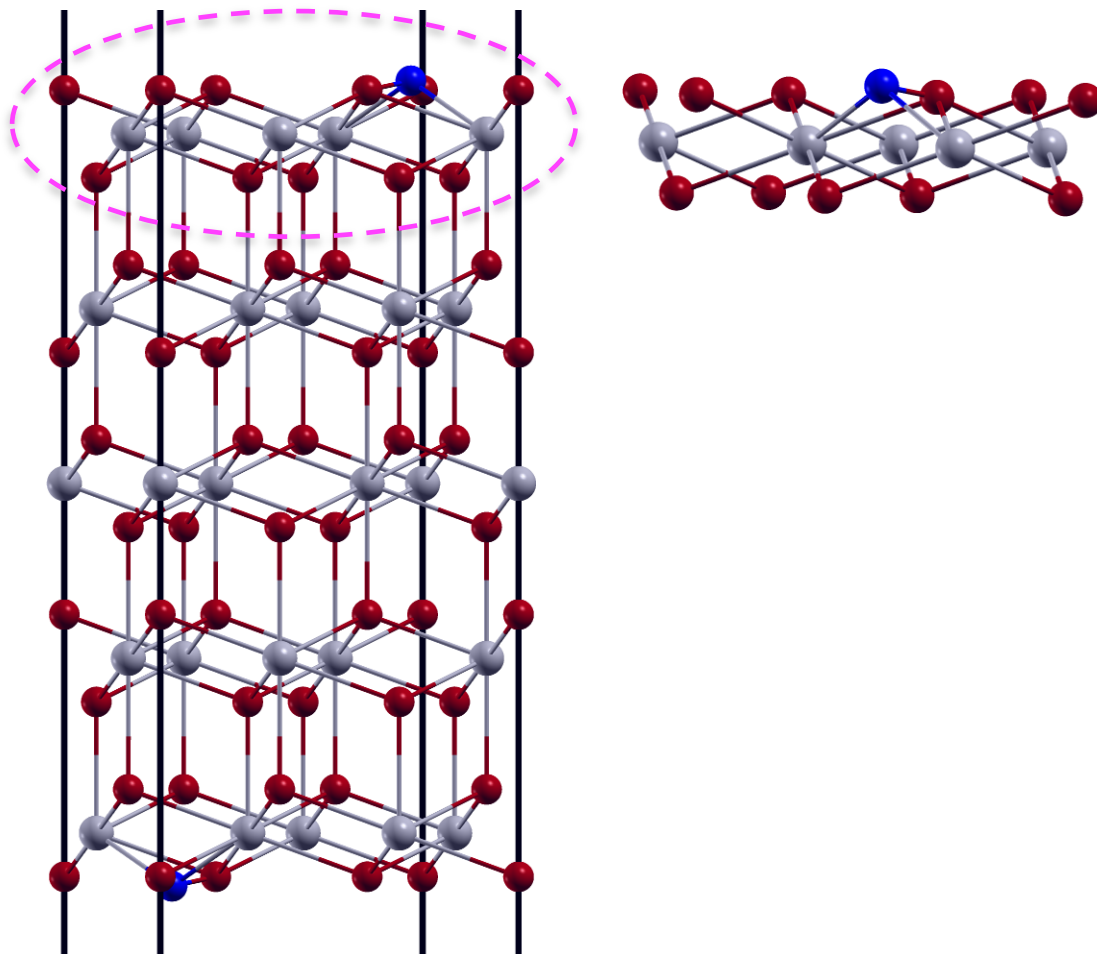


Figure 20: Atomic O initially placed at the two-fold bridge site of the 5 layer  $\text{UO}_2$  (111)

$\sqrt{3} \times \sqrt{3} - R30^\circ$  surface. The O adsorbate coverage is  $1/3$  ML.

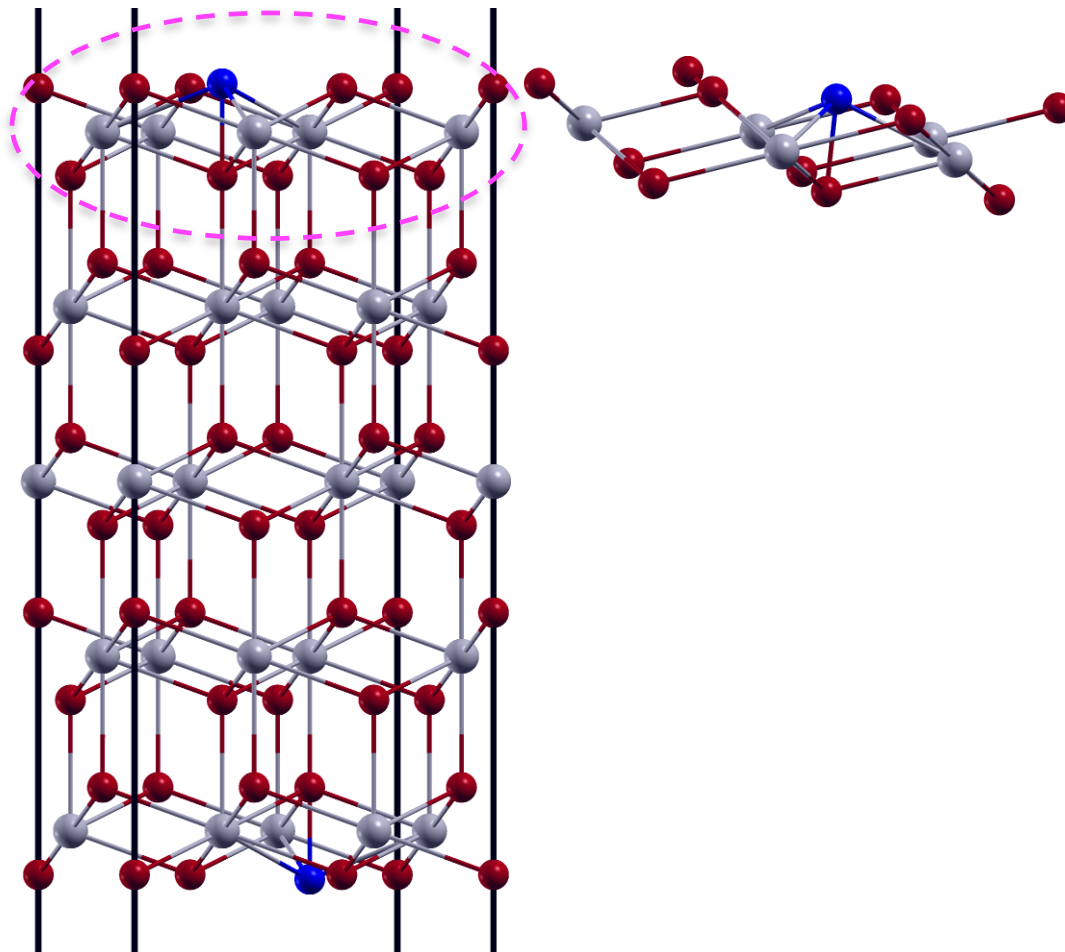


Figure 21: Atomic O initially placed at the three-fold hollow site of the 5 layer  $\text{UO}_2$  (111)

$\sqrt{3} \times \sqrt{3} - R30^\circ$  surface. The O adsorbate coverage is 1/3 ML.

## 4.2 Results and Discussion

Listed in Table 3 are the adsorption energies and equilibrium geometric parameters of the adsorbate relative to the surface. These adsorption energies were computed at the DFT level of theory. From the adsorption energies, we observe that the one-fold coordinated top site is preferred by the O adsorbate with an adsorption energy of 5.37 eV, followed by the two-fold bridge site (2.70 eV), with the three-fold hollow site having the least adsorption energy of 2.58 eV. These adsorption energies are indicative of chemical adsorption. The nature of the local one-fold coordinated structure at the top site closely resembles the uranyl di-oxo cation. The U-O bond distance for the bridge and hollow sites are longer than the bulk bond distance, while the top site U-O distance is shorter. The trend in the adsorption energy indicates that a high coordination number for the O adsorbate does not necessarily imply it is the most stable. The trend that we see here,  $E_{ads}(top) > E_{ads}(bridge) > E_{ads}(hollow)$ , is opposite the case of O adsorbed on pure U metal, where the higher coordinated sites are the most stable. The corresponding trend in the U-O adsorbate distances are,  $r_{U-O}(top) < r_{U-O}(bridge) < r_{U-O}(hollow)$ , which is opposite the adsorption energy trend.

Table 3: Equilibrium energetic and geometry parameters of the optimized slab adsorbate configurations.

Initial Site	$E_{ads}$ (eV)	Coord. #	U-O adsorbate distances (Å)
Top	5.37	1	1.86
Bridge	2.70	2	2.50, 2.60
Hollow	2.58	3	2.68, 2.71, 2.73

In Table 4 we have listed the U spin magnetic moments for each atomic layer for the clean and adsorbate covered slabs. For the bulk layer, minor changes in the spin moments in the adsorbate slab systems can be seen compared to the clean slab. For the subsurface layer moments ( $\mu_2$ ), we see sufficient changes for the bridge and hollow sites. This implies that some of the U 5f are transferred to the incoming adsorbate O and some of the local oxide O. For the top most layer ( $\mu_1$ ), a large reduction of  $1.73 \mu_B - 0.20 \mu_B = 1.53 \mu_B$  in one of the top site U atoms can be seen, while there is a small reduction in all the other U atoms at each site. The large moment reduction at the top site is a signature of significant electron transfer from U to the incoming O adsorbate.

Table 4: The U spin magnetic moments inside a muffin tin sphere for the bulk layer, subsurface layer ( $\mu_2$ ), and top layer ( $\mu_1$ ).  $\delta\phi = \phi_{slab+adsorbate} - \phi_{slab}$  is the change in work function due to adsorption, where the work function of the clean slab is  $\delta\phi = 3.46$  eV.

	Bulk Layer ( $\mu_B$ )	$\mu_2$ ( $\mu_B$ )	$\mu_1$ ( $\mu_B$ )	$\mu_{int}$ ( $\mu_B$ )	$\delta\phi$ (eV)
Bare	1.46, 1.46, 1.46	-1.52, -1.52, -1.52	1.73, 1.73, 1.73	0.76	
Top	1.54, 1.69, 1.69	-1.65, -1.72, -1.72	0.20, 1.61, 1.75	0.31	2.56
Bridge	1.50, 1.50, 1.50	-1.48, -1.48, -1.50	1.47, 1.52, 1.70	1.19	1.41
Hollow	1.48, 1.48, 1.65	-1.64, -1.65, -1.50	1.28, 1.33, 1.44	-0.41	1.86

To further probe the charge transfer process we examined the adsorbate induced changes in the electronic work function, and the difference charge density. The work function changes ( $\delta\phi = \phi_{slab+adsorbate} - \phi_{slab}$ ) are positive at all sites, implying the existence of a U-O dipole. The direction of the dipole will start from the O adsorbate and point inward into the surface. The existence of the dipole implies charge transfer from U to O.

Representative difference charge density plots are shown in Figure 22 and Figure 23 for the top site and bridge site respectively. We computed the difference charge density  $\Delta\rho(r)$ :

$$\Delta\rho(r) = \rho(\text{slab} + \text{ads}) - \rho(\text{slab}) - \rho(\text{ads}) \quad (4.1)$$

where  $\rho(\text{slab} + \text{ads})$  is the total electron charge density of the slab-with-adsorbate system,  $\rho(\text{slab})$  is the total charge density of the slab without the adsorbate, and  $\rho(\text{ads})$  is the total charge density of the O adsorbate without the slab. In the computation of  $\rho(\text{slab})$  and  $\rho(\text{ads})$ , the U and O atoms were kept at exactly the same positions as they were in the slab-with-adsorbate system. Clearly in Figure 22 (top site plot), there is excess charge build up (yellow region) around the O adsorbate (blue atom) and some charge depletion around the U atom. This is an indication of an ionic bond between U and O. There is also some charge build-up along the U- adsorbate O bond, implying some covalent bonding character. Figure 23, which depicts the adsorbate-U interaction at the bridge site, is similar to Figure 22 in the sense that the U- adsorbate O bond has significant covalent character.

The electronic spectrum was probed with the Gaussian-broadened single particle Kohn-Sham energy density of states (DOS). The energy eigenvalues correspond to a hybrid DFT Hamiltonian using the regular DFT. In Figure 24 we show the plot for the clean slab and the most stable top site. For each plot, we have shown the total DOS, U 5f partial DOS, U 6d partial DOS, and O 2p partial DOS. The nature of the gap for the clean slab indicates a Mott-Hubbard type insulating behavior since it is associated with a U 5f-5f transition and the valence O 2p band lies below the U 5f band. The computed band-gap for the clean slab was 1.1 eV, which is in agreement with the results for the

systematic slab calculations in Chapter 3. A couple of distinct features can be seen in the lower panel of the for the slab-adsorbate system at the top site. First, the presence of the adsorbate increases the valence electron population, and as a result, the band gap reduces to 0.7 eV. The reduction in the band gap is not surprising since the presence of the adsorbate increases the valence electron population, resulting in a shift of the Fermi level towards the unoccupied region. In comparison to the clean slab DOS, we see that the O adsorbate introduces impurity states which are in the -3 eV to -1 eV energy range; these states do overlap with the U 5f states. It is interesting, however, that even in the presence of the adsorbate the Mott-Hubbard type insulating behavior seen in the bulk and clean slab is still retained since the band gap is dictated by a U 5f—U 5f transition.

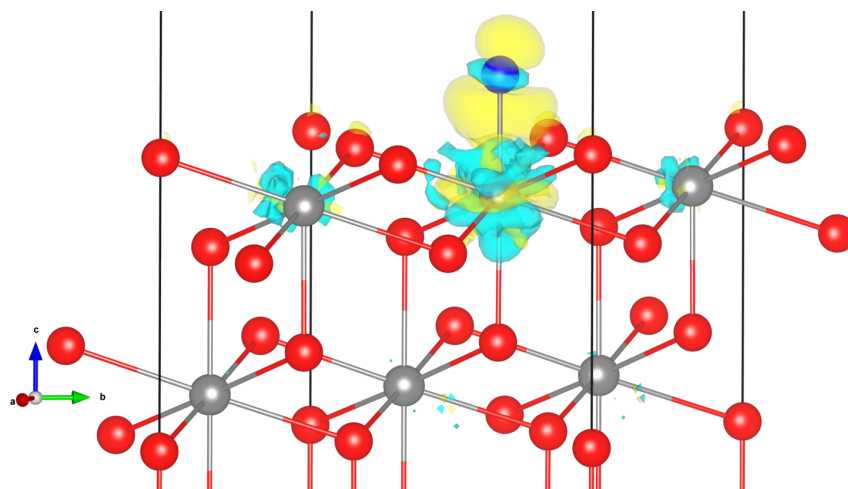


Figure 22: A depiction of the difference charge density plot,  $\Delta\rho(r)$ , for O top site. The yellow regions denote electron density build-up, while the cyan regions denote charge electron density deficiency. The U and O atoms are colored grey and red respectively; the O adsorbate is colored blue. The iso-level surface is  $0.01 \text{ e/a.u.}^3$ .

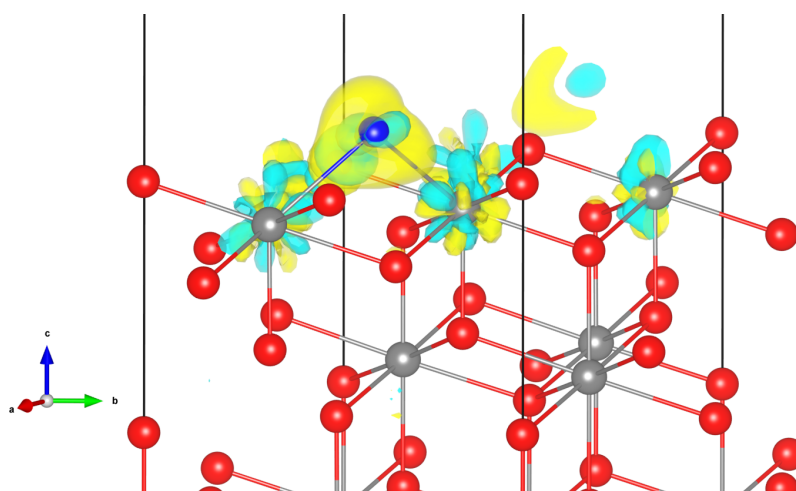


Figure 23: A depiction of the difference charge density plot,  $\Delta\rho(r)$ , for O bridge site. The atom color scheme and electron density color scheme is the same as in Figure 22.

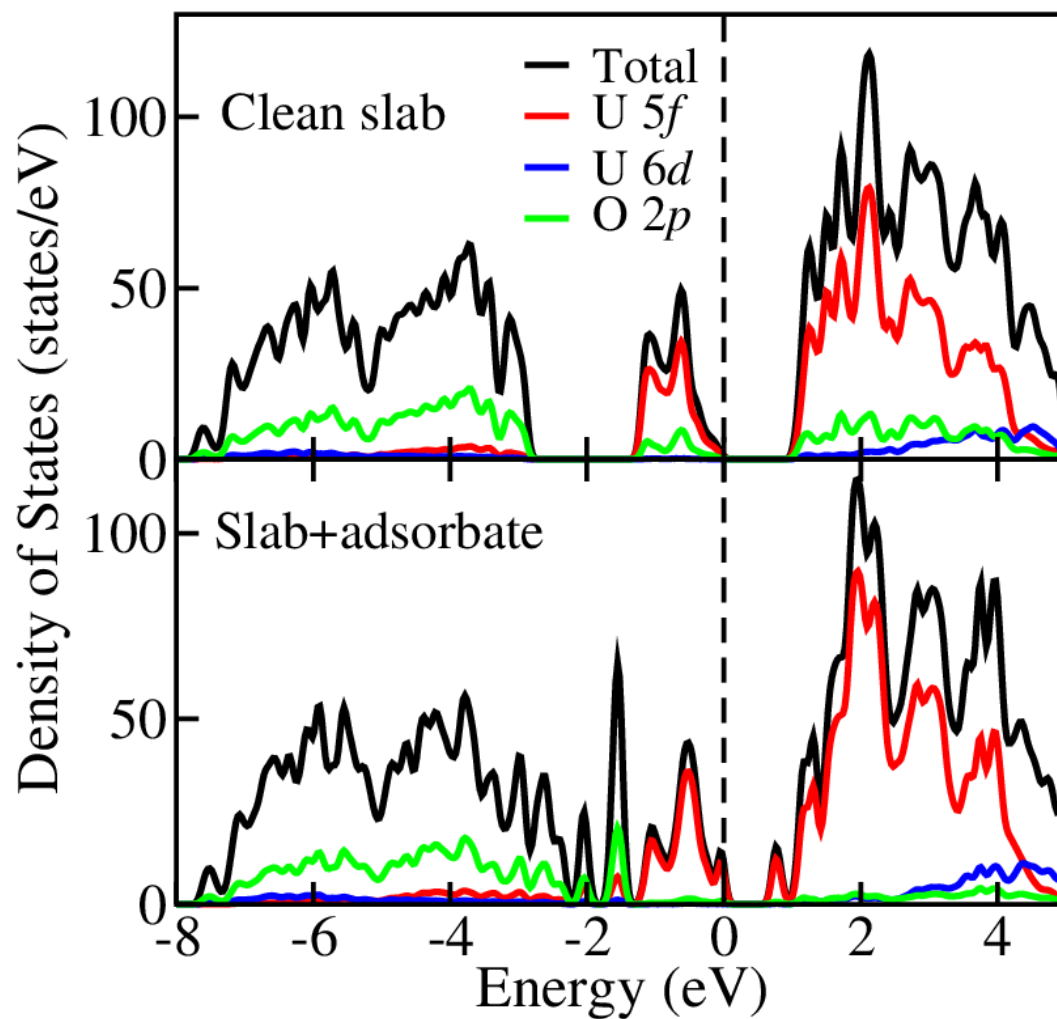


Figure 24: Electronic density of states of the top site and bare slab. The dash line denotes the Fermi level.

## Chapter 5

### Conclusion

Uranium dioxide ( $\text{UO}_2$ ) is well known for its importance as a nuclear fuel. The corrosion and weathering of  $\text{UO}_2$  upon the exposure to environmental elements can lead to undesirable scenarios. The oxidation of  $\text{UO}_2$  can result in a volume expansion up to 38%, implying that the corrosion of  $\text{UO}_2$  could impact the integrity of fuel rods in nuclear reactors and nuclear waste storage facilities. While uranium is barely radioactive, it is a nephrotoxic, that is, it has a toxic/poisonous effect on the kidneys when ingested. Therefore the release of uranium oxide particulates into the biosphere has non-trivial health consequences. Experimental studies of  $\text{UO}_2$ -based materials are difficult due to their hazardous nature. In this regard, theoretical studies can supplement experimental efforts to understand the mechanisms via which  $\text{UO}_2$  materials interact with the biosphere.

The interaction of  $\text{UO}_2$  with environmental elements occurs at its exposed surface. A fundamental understanding of this interaction process begins at the atomic scale. Computational modeling of the properties of clean uranium dioxide ( $\text{UO}_2$ ) surfaces is a necessary step to modeling and understanding  $\text{UO}_2$  surface mechanisms such as corrosion and the formation of complex species via environmental gas adsorption. In this thesis, structural and electronic properties of clean and adsorbate-covered low index  $\text{UO}_2$  surfaces were modeled using hybrid density functional theory. Specifically, the properties of the clean (111) and (110) surfaces and the interaction of atomic oxygen with the (111) surface were modeled. It was observed that spin-orbit coupling (SOC) was necessary to accurately describe the clean surface properties. Thus all clean surface calculations were done with SOC.

For the clean surface, the evolution of the work function, surface energy, incremental energy, and band gap with respect to the system size was studied. The computed surface properties are in good agreement with available theoretical and experimental data. We observed that at five formula units and beyond the surface properties of  $\text{UO}_2$  converge. The estimated work function, surface energy, and band gap of the (111) surface were 3.5 eV,  $0.97 \text{ J/m}^2$ , and 1.2 eV respectively; the corresponding values for the (110) surface were 2.2 eV,  $1.76 \text{ J/m}^2$ , and 0.65 eV respectively. The localization of the 5f electron states is pronounced at the top surface layer while bulk-like behavior is exhibited at and below the subsurface layer. The Mott-Hubbard type insulating behavior in the bulk is retained in the surfaces, albeit with a smaller band gap.

Preliminary adsorption studies of atomic oxygen on the  $\text{UO}_2$  (111) surface at a coverage of  $1/3 \text{ ML}$  indicates that the on-top site is the most preferred site with the adsorbate being closest to the surface. The adsorption was chemical in nature (chemisorption) with an adsorption energy of 5.37 eV and an equilibrium U-O bond distance of  $1.86 \text{ \AA}$ . The adsorption process resulted in significant electron transfer from the U substrate to the O adsorbate, and subsequently, the bond formation was ionic in nature. In turn, the ionic bond formation resulted in a surface dipole, which caused the electron work function to increase by 2.56 eV. Analysis of the electron density of states at the favorable top site indicates significant hybridization between the U 5f states and adsorbate O 2p states. Also, the presence of the adsorbate did not alter the Mott-Hubbard insulating behavior seen in the bulk crystal and clean surface. Overall, the presence of the O adsorbate on the  $\text{UO}_2$  (111) surface significantly stabilizes the surface, implying that higher oxide formation in  $\text{UO}_2$ , that is  $\text{UO}_{2+x}$ , is a stable process.

Appendix A

NSO (110) and (111) Surface Tables and Figures

Table 5: Surface properties of  $\text{UO}_2$  (110) NSO AFM films.  $E_{tot}(N)$  is the total energy,  $\Delta E_N$  is the slab incremental energy,  $\gamma$  is the surface energy,  $\Phi$  is the work function, and  $\Delta_{gap}$  is the band gap of the  $N$ -layer slab.  $E_{tot}(N)$  and  $\Delta E_N$  have been shifted by +56468 Ry.

N	$E_{tot}(N)$ (Ry/f.u.)	$\Delta E_N$ (Ry)	$\gamma$ (J/m <sup>2</sup> )	$\Phi$ (eV)	$\Delta_{gap}(N)$ (eV)
1	1.1533903		1.88	3.18	0.40
2	0.9272943	0.7011984	1.40	2.49	0.89
3	0.8828148	0.7938557	1.41	2.12	0.60
4	0.8625502	0.8017566	1.46	2.20	0.66
5	0.8531117	0.8153578	1.58	1.99	0.34
6	0.8456115	0.8081101	1.66	2.24	0.77
7	0.8378154	0.7910393	1.65	2.44	0.94
Bulk	0.8018765				1.62
Semi-infinite			1.57		

Table 6: Surface properties of  $\text{UO}_2$  (111) NSO AFM films.  $E_{tot}(N)$  is the total energy,  $\Delta E_N$  is the slab incremental energy,  $\gamma$  is the surface energy,  $\Phi$  is the work function, and  $\Delta_{gap}$  is the band gap of the  $N$ -layer slab.  $E_{tot}(N)$  and  $\Delta E_N$  have been shifted by +56468 Ry.

N	$E_{tot}(N)$ (Ry/f.u.)	$\Delta E_N$ (Ry)	$\gamma$ (J/m <sup>2</sup> )	$\Phi$ (eV)	$\Delta_{gap}(N)$ (eV)
1	0.8918656		0.75	4.00	1.8
2	0.8424611	0.7930567	0.66	3.78	1.5
3	0.8289645	0.8019713	0.64	3.51	1.1
4	0.8224022	0.8027154	0.63	3.41	1.0
5	0.8187016	0.8038992	0.64	3.56	1.0
6	0.8168832	0.8077910	0.67	3.73	1.2
7	0.8162231	0.8122627	0.74	3.59	1.2
Bulk	0.8018765				1.6
Semi-infinite			0.68		

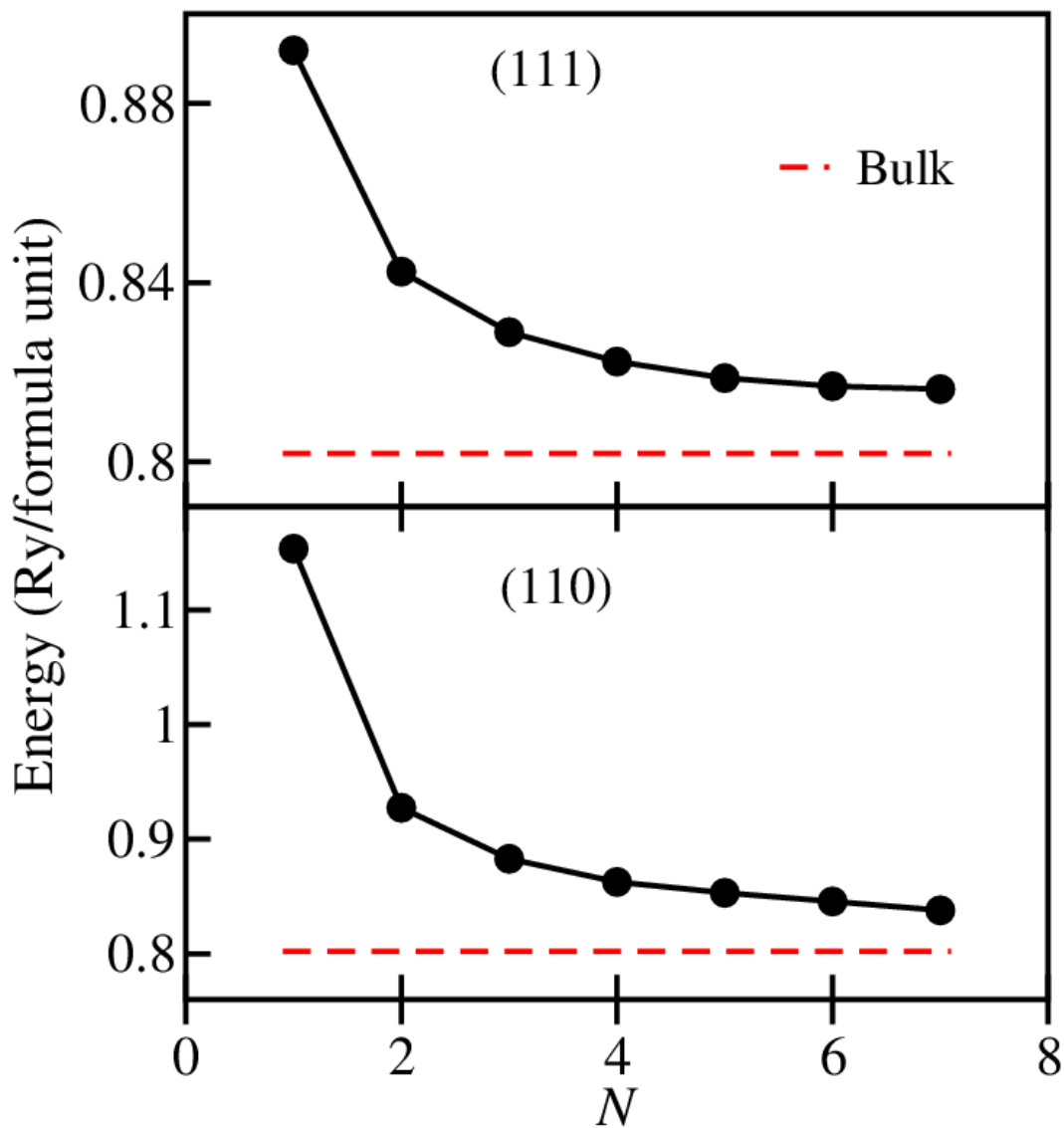


Figure 25: Variations of the energy per formula unit (that is, per  $\text{UO}_2$ ) of the (111) and (110) NSO surfaces as a function of slab thickness. The dashed line denotes the energy per formula unit for the bulk crystal.

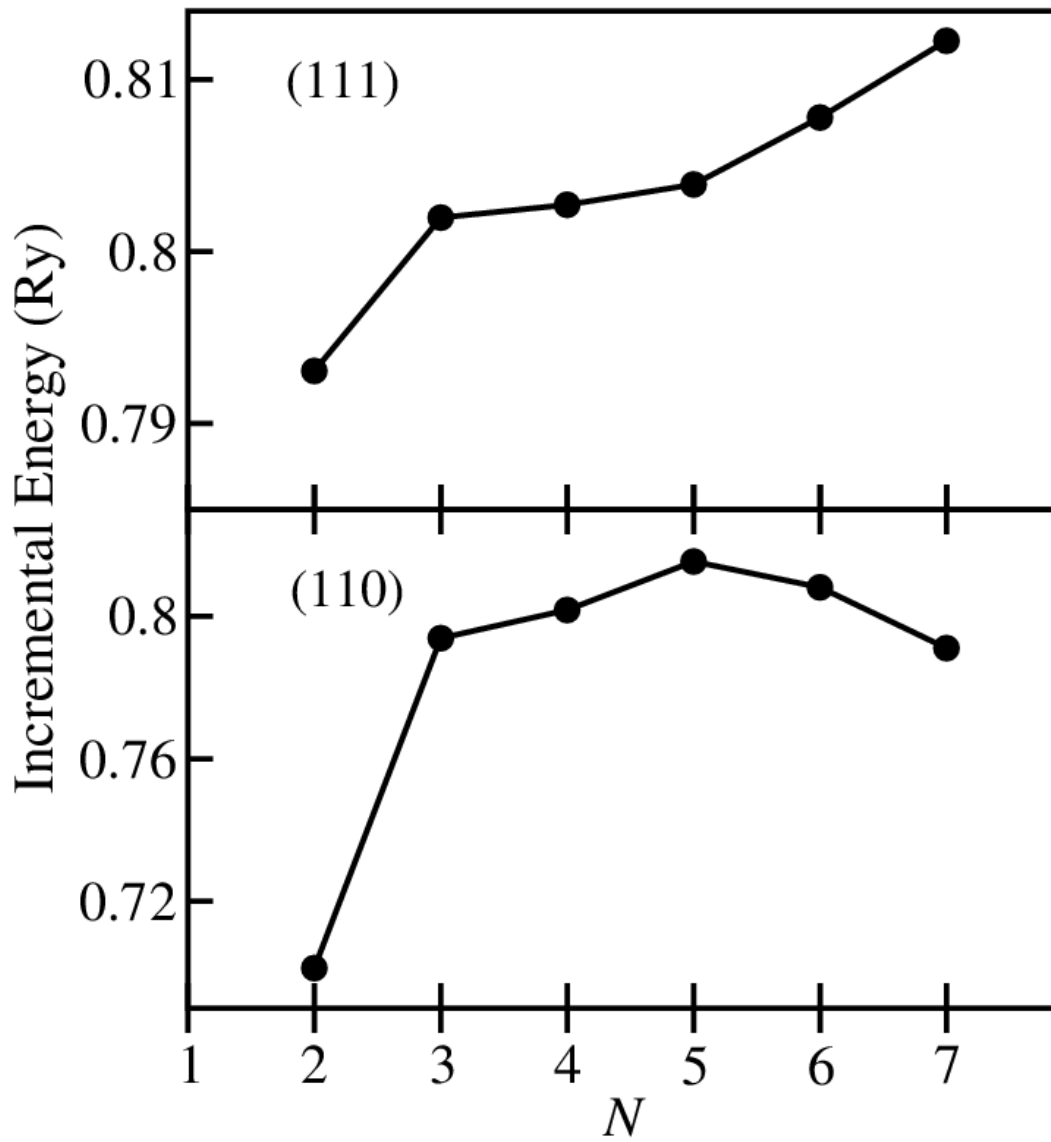


Figure 26: Variations of the incremental energies of the (111) and (110) NSO slabs as a function slab thickness.

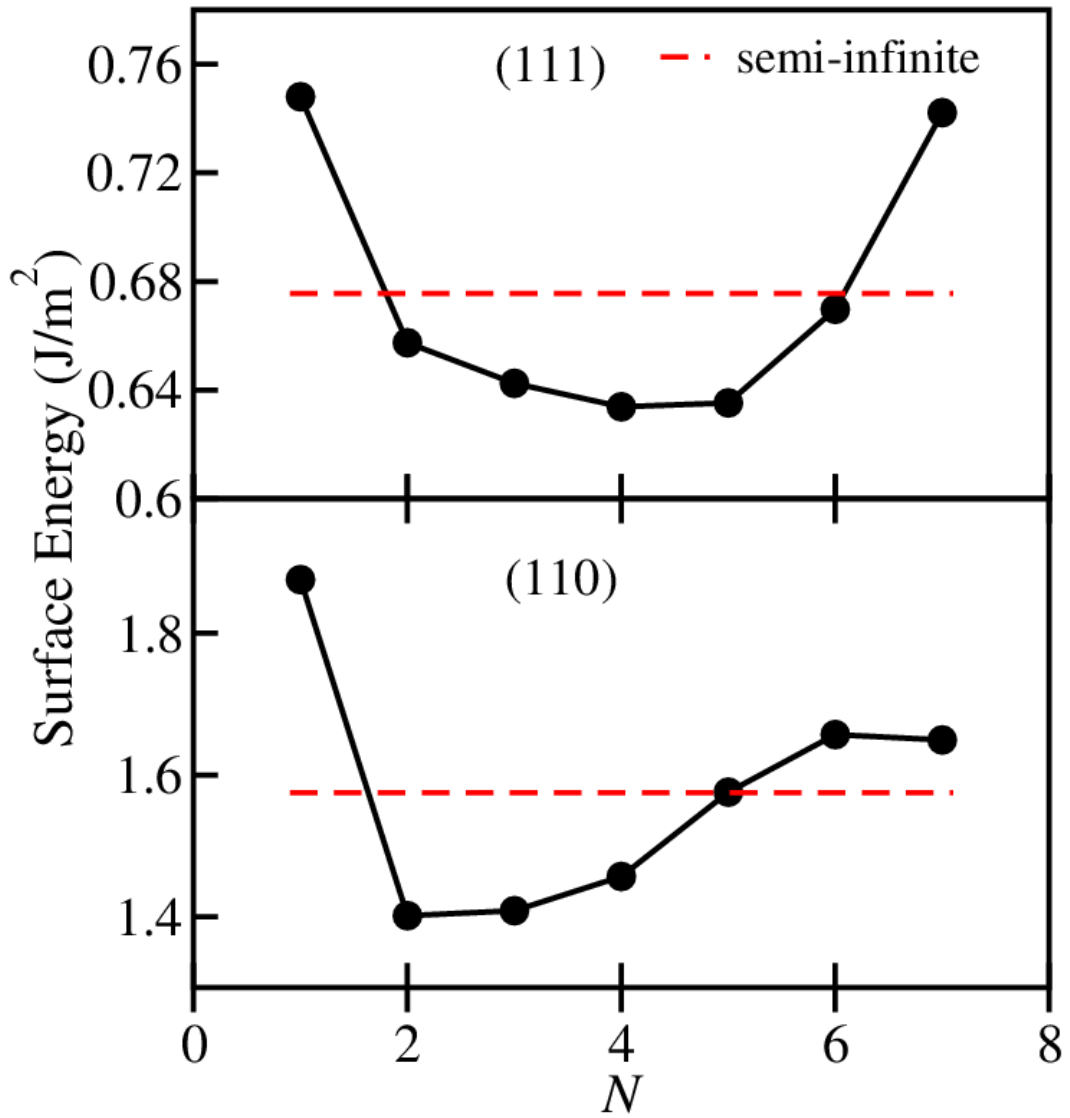


Figure 27: Variations of the surface energies of the (111) and (110) NSO slabs as a function of slab thickness. The dashed line denotes the surface energy of a slab of semi-infinite thickness.

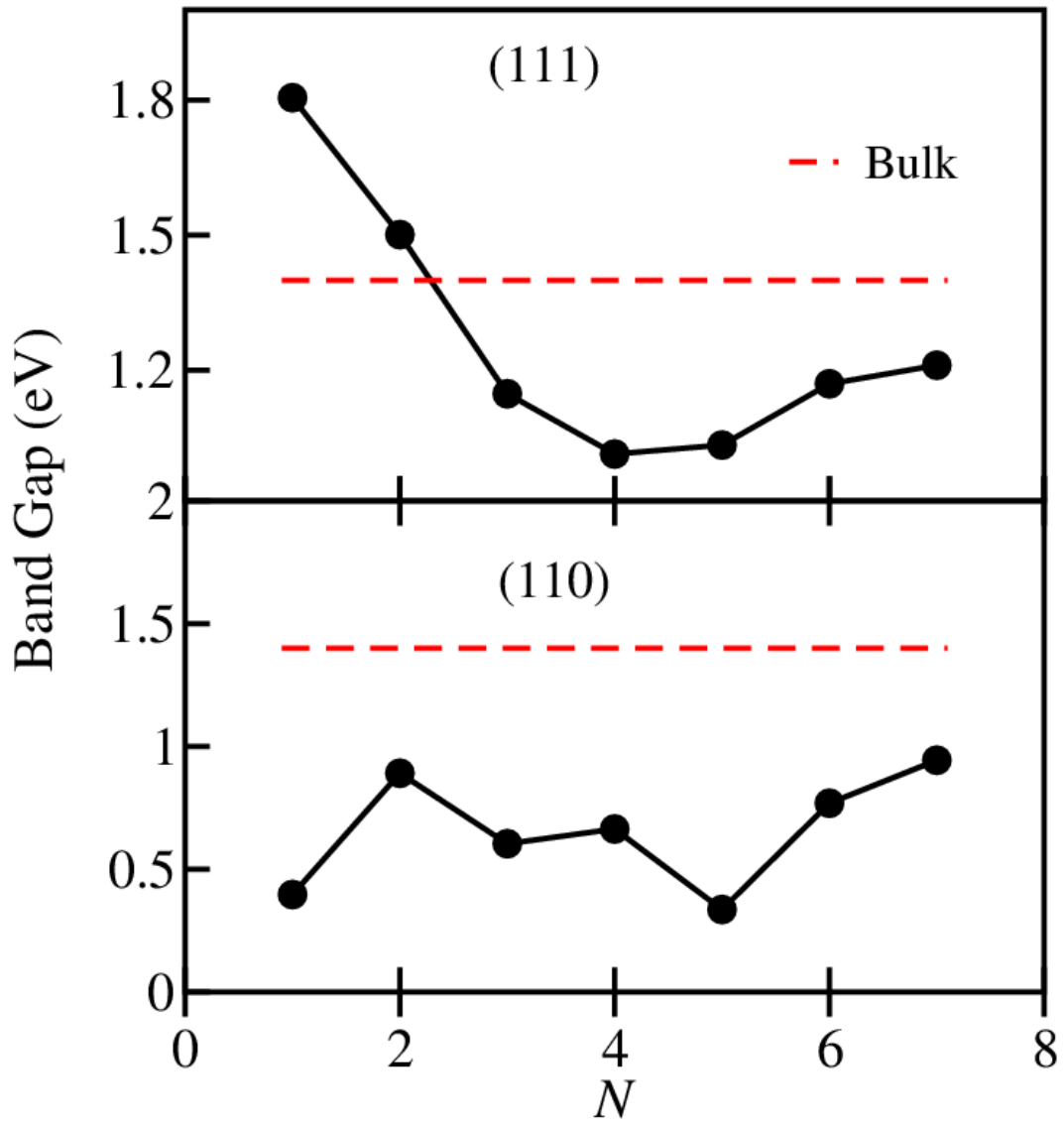


Figure 28: Plots of the NSO surface electronic band gaps as a function of slab thickness.

The dashed horizontal line denotes the band gap of the bulk crystal.

## References

1. R. J. McEachern and P. Taylor, Journal of Nuclear Materials **254** (2-3), 87-121 (1998).
2. K. M. Wasywich, W. H. Hocking, D. W. Shoesmith and P. Taylor, Nuclear technology **104** (3), 309-329 (1993).
3. G. Sattonnay, C. Ardois, C. Corbel, J. F. Lucchini, M. F. Barthe, F. Garrido and D. Gosset, Journal of Nuclear Materials **288** (1), 11-19 (2001).
4. R. A. Schueneman, A. I. Khaskelis, D. Eastwood, W. J. van Ooij and L. W. Burggraf, Journal of Nuclear Materials **323** (1), 8-17 (2003).
5. D. W. Shoesmith, Journal of Nuclear Materials **282** (1), 1-31 (2000).
6. M. J. Bannister, Journal of Nuclear Materials **26** (2), 174-184 (1968).
7. G. C. Allen, P. A. Tempest and J. W. Tyler, Philosophical Magazine Part B **54** (2), L67-L71 (1986).
8. P. Taylor, D. D. Wood, A. M. Duclos and D. G. Owen, Journal of Nuclear Materials **168** (1-2), 70-75 (1989).
9. O. C. Lind, B. Salbu, L. Skipperud, K. Janssens, J. Jaroszewicz and W. De Nolf, Journal of environmental radioactivity **100** (4), 301-307 (2009).
10. D. Barthelmy, [http://www.webmineral.com/chem/Chem-names-U.shtml -.UvWCtv33Dbw](http://www.webmineral.com/chem/Chem-names-U.shtml-.UvWCtv33Dbw).
11. C. N. Association, [http://www.cna.ca/nuclear\\_facts/uranium\\_canada/](http://www.cna.ca/nuclear_facts/uranium_canada/) (2011).
12. W. N. Association, <http://www.world-nuclear.org/info/Nuclear-Fuel-Cycle/Introduction/Nuclear-Fuel-Cycle-Overview/> (2012).
13. W. N. Association, <http://www.world-nuclear.org/info/Nuclear-Fuel-Cycle/Mining-of-Uranium/Uranium-Mining-Overview/> (2012).

14. I. A. E. Agency, [http://www.iaea.org/OurWork/ST/NE/NEFW/\\_nefw-documents/NuclearFuelCycle.pdf](http://www.iaea.org/OurWork/ST/NE/NEFW/_nefw-documents/NuclearFuelCycle.pdf).
15. W. N. Association, <http://www.world-nuclear.org/info/Nuclear-Fuel-Cycle/Mining-of-Uranium/In-Situ-Leach-Mining-of-Uranium/> (2014).
16. N. R. Commission, <http://www.nrc.gov/materials/fuel-cycle-fac/ur-enrichment.html> (2014).
17. W. N. Association, <http://www.world-nuclear.org/info/Nuclear-Fuel-Cycle/Conversion-Enrichment-and-Fabrication/Uranium-Enrichment/> (2013).
18. W. N. Association, <http://www.world-nuclear.org/info/Nuclear-Fuel-Cycle/Nuclear-Wastes/Radioactive-Waste-Management/> (2013).
19. I. A. E. Agency, [http://www.iaea.org/OurWork/ST/NE/NEFW/\\_nefw-documents/HLWaste2011.pdf](http://www.iaea.org/OurWork/ST/NE/NEFW/_nefw-documents/HLWaste2011.pdf) (2011).
20. W. N. Association, <http://www.world-nuclear.org/Nuclear-Basics/Global-number-of-nuclear-reactors/>.
21. W. N. Association, <http://www.world-nuclear.org/info/Facts-and-Figures/World-Nuclear-Power-Reactors-and-Uranium-Requirements/> (2014).
22. N. E. Institute, <http://www.nei.org/Knowledge-Center/Nuclear-Statistics/US-Nuclear-Power-Plants> (2013).
23. U. S. D. o. Energy, [http://energy.gov/sites/prod/files/Strategy\\_for\\_the\\_Management\\_and\\_Disposal\\_of\\_Used\\_Nuclear\\_Fuel\\_and\\_High\\_Level\\_Radioactive\\_Waste.pdf](http://energy.gov/sites/prod/files/Strategy_for_the_Management_and_Disposal_of_Used_Nuclear_Fuel_and_High_Level_Radioactive_Waste.pdf) (2013).

24. N. E. Institute, <http://www.nei.org/Knowledge-Center/Nuclear-Statistics/On-Site-Storage-of-Nuclear-Waste>.
25. N. R. Commission, <http://www.nrc.gov/waste/spent-fuel-storage/faqs.html> (2013).
26. N. R. Commission, <http://www.nrc.gov/reading-rm/doc-collections/factsheets/storage-spent-fuel-fs.html> (2013).
27. N. R. Commission, <http://www.nrc.gov/waste/spent-fuel-storage/dry-cask-storage.html> (2013).
28. N. R. Commission, Accession #ML072990220.
29. A. G. Ritchie, Journal of Nuclear Materials **102** (1-2), 170-182 (1981).
30. J. M. Haschke, Journal of Alloys and Compounds **278** (1-2), 149-160 (1998).
31. C. A. Colmenares, J. Solid State Chem. **15**, 257 (1984).
32. A. G. Ritchie, R. C. Greenwood and S. J. Randles, Journal of Nuclear Materials **139** (2), 121-136 (1986).
33. T. Gouder, C. Colmenares, J. R. Naegle and J. Verbist, Surface Science **235** (2-3), 280-286 (1990).
34. H. Idriss, Surface Science Reports **65** (3), 67-109 (2010).
35. S. D. Senanayake, R. Rousseau, D. Colegrave and H. Idriss, Journal of Nuclear Materials **342** (1-3), 179-187 (2005).
36. G. Amoretti, A. Blaise, R. Caciuffo, J. M. Fournier, M. T. Hutchings, R. Osborn and A. D. Taylor, Physical Review B **40** (3), 1856-1870 (1989).
37. R. Caciuffo, N. Magnani, P. Santini, S. Carretta, G. Amoretti, E. Blackburn, M. Enderle, P. J. Brown and G. H. Lander, Journal of Magnetism and Magnetic Materials **310** (2), 1698-1702 (2007).

38. P. Giannozzi and E. P., *J. Magn. Magn. Mater.* **67**, pp. 75–87 (1987).
39. S. B. Wilkins, R. Caciuffo, C. Detlefs, J. Rebizant, E. Colineau, F. Wastin and G. H. Lander, *Physical Review B* **73** (6), 060406 (2006).
40. W. M. Jones, J. Gordon and E. A. Long, *The Journal of Chemical Physics* **20** (4), 695-699 (1952).
41. A. Arrott and J. E. Goldman, *Physical Review* **108** (4), 948-953 (1957).
42. B. W. Veal and D. J. Lam, *Physical Review B* **10** (12), 4902-4908 (1974).
43. J. Verbist, J. Riga, J. J. Pireaux and R. Caudano, *Journal of Electron Spectroscopy and Related Phenomena* **5** (1), 193-205 (1974).
44. L. E. Cox, *Journal of Electron Spectroscopy and Related Phenomena* **26** (2), 167-171 (1982).
45. J. Schoenes, *Journal of Applied Physics* **49** (3), 1463-1465 (1978).
46. S. W. Yu, J. G. Tobin, J. C. Crowhurst, S. Sharma, J. K. Dewhurst, P. O. Velasco, W. L. Yang and W. J. Siekhaus, *Physical Review B* **83** (16), 165102 (2011).
47. Y. Baer and J. Schoenes, *Solid State Communications* **33** (8), 885-888 (1980).
48. P. Hohenberg and W. Kohn, *Physical Review B* **136** (3B), B864-+ (1964).
49. W. Kohn and L. J. Sham, *Physical Review* **140** (4A), 1133-1138 (1965).
50. D. M. Ceperley and B. J. Alder, *Physical Review Letters* **45** (7), 566-569 (1980).
51. S. H. Vosko, L. Wilk and M. Nusair, *Canadian Journal of Physics* **58** (8), 1200-1211 (1980).
52. J. P. Perdew, K. Burke and M. Ernzerhof, *Phys. Rev. Lett.* **77**, 3865 (1996).
53. K. N. Kudin, G. E. Scuseria and R. L. Martin, *Phys Rev Lett* **89** (26), 266402 (2002).
54. Y. Yun, H. Kim and K. Park, *Nucl. Eng. Tech.* **37**, 293 (2005).
55. P. J. Kelly and M. S. S. Brooks, *J. Chem. Soc. Faraday Trans. II* **83**, 1189 (1987).

56. J. C. Boettger and A. K. Ray, *International Journal of Quantum Chemistry* **80** (45), 824-830 (2000).
57. C. Adamo and V. Barone, *Journal of Chemical Physics* **110** (13), 6158-6170 (1999).
58. A. D. Becke, *The Journal of Chemical Physics* **98** (2), 1372 (1993).
59. J. Heyd, G. E. Scuseria and M. Ernzerhof, *Journal of Chemical Physics* **118** (18), 8207-8215 (2003).
60. V. I. Anisimov, J. Zaanen and O. K. Andersen, *Physical Review B* **44** (3), 943-954 (1991).
61. J. P. Perdew and A. Zunger, *Physical Review B* **23** (10), 5048-5079 (1981).
62. A. Georges, G. Kotliar, W. Krauth and M. J. Rozenberg, *Reviews of Modern Physics* **68** (1), 13-125 (1996).
63. G. Kotliar, S. Y. Savrasov, K. Haule, V. S. Oudovenko, O. Parcollet and C. A. Marianetti, *Reviews of Modern Physics* **78** (3), 865-951 (2006).
64. X. D. Wen, R. L. Martin, T. M. Henderson and G. E. Scuseria, *Chemical reviews* **113** (2), 1063-1096 (2013).
65. X.-D. Wen, R. L. Martin, L. E. Roy, G. E. Scuseria, S. P. Rudin, E. R. Batista, T. M. McCleskey, B. L. Scott, E. Bauer, J. J. Joyce and T. Durakiewicz, *The Journal of Chemical Physics* **137** (15), 154707 (2012).
66. I. D. Prodan, G. E. Scuseria and R. L. Martin, *Physical Review B* **73** (4), 045104-045104 (2006).
67. F. Gupta, G. Brillant and A. Pasturel, *Philosophical Magazine* **87** (16-17), 2561-2569 (2007).
68. H. Y. Geng, Y. Chen, Y. Kaneta and M. Kinoshita, *Physical Review B* **75** (5), 054111-054111 (2007).

69. P. Nerikar, T. Watanabe, J. S. Tulenko, S. R. Phillpot and S. B. Sinnott, *Journal of Nuclear Materials* **384** (1), 61-69 (2009).
70. D. Gryaznov, E. Heifets and E. Kotomin, *Physical chemistry chemical physics : PCCP* **11** (33), 7241-7247 (2009).
71. L. Ma, R. Atta-Fynn and A. K. Ray, *Journal of Theoretical and Computational Chemistry (JTCC)* **11** (03), 611-629 (2012).
72. S. L. Dudarev, D. N. Manh and A. P. Sutton, *Philosophical Magazine Part B* **75** (5), 613-628 (1997).
73. S. L. Dudarev, G. A. Botton, S. Y. Savrasov, Z. Szotek, W. M. Temmerman and A. P. Sutton, *Physica status solidi (a)* **166** (1), 429-443 (1998).
74. J. Yu, R. Devanathan and W. J. Weber, *Journal of physics. Condensed matter : an Institute of Physics journal* **21** (43), 435401 (2009).
75. B. Dorado, B. Amadon, M. Freyss and M. Bertolus, *Physical Review B* **79** (23), 235125 (2009).
76. L. Petit, A. Svane, Z. Szotek, W. M. Temmerman and G. M. Stocks, *Physical Review B* **81** (4), 045108 (2010).
77. A. J. Devey, *Journal of Nuclear Materials* **412** (3), 301-307 (2011).
78. M. Sanati, R. C. Albers, T. Lookman and A. Saxena, *Physical Review B* **84** (1), 014116 (2011).
79. F. Jollet, G. Jomard, B. Amadon, J. P. Crocombette and D. Torumba, *Physical Review B* **80** (23), 235109 (2009).
80. A. E. Thompson and C. Wolverton, *Physical Review B* **84** (13), 134111 (2011).
81. X. F. Tian, T. Gao, G. Jiang, D. W. He and H. X. Xiao, *Computational Materials Science* **54** (0), 188-194 (2012).
82. B. Dorado and P. Garcia, *Physical Review B* **87** (19), 195139 (2013).

83. M. Iwasawa, Y. Chen, Y. Kaneta, T. Ohnuma, H. Y. Geng and M. Kinoshita, *Materials Transactions* **47** (11), 2651-2657 (2006).
84. I. D. Prodan, G. E. Scuseria and R. L. Martin, *Physical Review B* **76** (3), 033101 (2007).
85. Q. Yin, A. Kutepov, K. Haule, G. Kotliar, S. Y. Savrasov and W. E. Pickett, *Physical Review B* **84** (19), 195111 (2011).
86. R. Laskowski, G. K. H. Madsen, P. Blaha and K. Schwarz, *Physical Review B* **69** (14), 140408 (2004).
87. P. Zhang, B. T. Wang and X. G. Zhao, *Physical Review B* **82** (14), 144110 (2010).
88. A. M. Chaka, G. A. E. Oxford, J. E. Stubbs, P. J. Eng and J. R. Bargar, *Computational and Theoretical Chemistry* **987** (0), 90-102 (2012).
89. B. Dorado, M. Freyss, B. Amadon, M. Bertolus, G. Jomard and P. Garcia, *Journal of physics. Condensed matter : an Institute of Physics journal* **25** (33), 333201 (2013).
90. R. O. A. Hall, M. J. Mortimer and D. A. Mortimer, *Journal of Nuclear Materials* **148** (3), 237-256 (1987).
91. E. N. Hodkin and M. G. Nicholas, *Journal of Nuclear Materials* **67** (1-2), 171-180 (1977).
92. P. Nikolopoulos, S. Nazare and F. Thummler, *Journal of Nuclear Materials* **71** (1), 89-94 (1977).
93. F. M. Page and D. E. Woolley, *Combustion and Flame* **23** (1), 121-127 (1974).
94. F. N. Skomurski, R. C. Ewing, A. L. Rohl, J. D. Gale and U. Becker, *American Mineralogist* **91** (11-12), 1761-1772 (2006).

95. P. F. Weck, E. Kim, C. F. Jove-Colon and D. C. Sassani, Dalton transactions **42** (13), 4570-4578 (2013).
96. R. Evarestov, A. Bandura and E. Blokhin, Acta Materialia **57** (2), 600-606 (2009).
97. Z. Rák, R. C. Ewing and U. Becker, Surface Science **608**, 180-187 (2013).
98. P. W. Tasker, Surface Science **87** (2), 315-324 (1979).
99. G. Sattonnay and R. Tetot, Journal of physics. Condensed matter : an Institute of Physics journal **26** (5), 055403 (2014).
100. J. Rabone and M. Krack, Computational Materials Science **71**, 157-164 (2013).
101. K. B. Alberman and J. S. Anderson, Journal of the Chemical Society (Resumed), S303 (1949).
102. G. C. Allen, Philosophical Magazine Part B **51** (4), 465-473 (1985).
103. G. C. Allen and N. R. Holmes, Journal of Nuclear Materials **223** (3), 231-237 (1995).
104. G. C. Allen, P. A. Tempest and J. W. Tyler, Nature **295** (5844), 48-49 (1982).
105. S. Aronson, R. B. Roof and J. Belle, Journal of Chemical Physics **27** (1), 137-144 (1957).
106. P. E. Blackburn, J. Weissbart and E. A. Gulbranson, Journal of Physical Chemistry **62** (8), 902-908 (1958).
107. M. E. Broczkowski, J. J. Noël and D. W. Shoesmith, Journal of Nuclear Materials **346** (1), 16-23 (2005).
108. M. E. Broczkowski, J. J. Noël and D. W. Shoesmith, Journal of Electroanalytical Chemistry **602** (1), 8-16 (2007).
109. P. Carbol, P. Fors, T. Gouder and K. Spahlu, Geochimica Et Cosmochimica Acta **73** (15), 4366-4375 (2009).
110. W. P. Ellis, The Journal of Chemical Physics **48** (12), 5695 (1968).

111. H. He and D. Shoesmith, *Physical chemistry chemical physics* : PCCP **12**, 8108-8117 (2010).
112. A. Leenaers, L. Sannen, S. Van den Berghe and M. Verwerft, *Journal of Nuclear Materials* **317** (2-3), 226-233 (2003).
113. O. Ménard, T. Advocat, J. P. Ambrosi and A. Michard, *Applied Geochemistry* **13** (1), 105-126 (1998).
114. C. Muggelberg, M. R. Castell, G. A. D. Briggs and D. T. Goddard, *Surface Science* **402** (1-3), 673-677 (1998).
115. L. E. J. Roberts, *Journal of the Chemical Society (Resumed)*, 3332 (1954).
116. G. Rousseau, L. Desgranges, F. Charlot, N. Millot, J. C. Niepce, M. Pijolat, F. Valdivieso, G. Baldinozzi and J. F. Berar, *Journal of Nuclear Materials* **355** (1-3), 10-20 (2006).
117. S. D. Senanayake and H. Idriss, *Surface Science* **563** (1-3), 135-144 (2004).
118. S. D. Senanayake, G. I. N. Waterhouse, A. S. Y. Chan, T. E. Madey, D. R. Mullins and H. Idriss, *Catalysis Today* **120** (2), 151-157 (2007).
119. D. W. Shoesmith, M. Kolar and F. King, *Corrosion* **59** (9), 802-816 (2003).
120. J. Stultz, M. T. Paffett and S. A. Joyce, *Journal of Physical Chemistry B* **108** (7), 2362-2364 (2004).
121. B. W. Veal, D. J. Lam, W. T. Carnall and H. R. Hoekstra, *Physical Review B* **12** (12), 5651-5663 (1975).
122. V. J. Wheeler, *Journal of Nuclear Materials* **40** (2), 189-194 (1971).
123. J. C. Boettger and A. K. Ray, *International Journal of Quantum Chemistry* **90** (4-5), 1470-1477 (2002).
124. F. N. Skomurski, L. C. Shuller, R. C. Ewing and U. Becker, *Journal of Nuclear Materials* **375** (3), 290-310 (2008).

125. A. H. H. Tan, R. W. Grimes and S. Owens, *Journal of Nuclear Materials* **344** (1-3), 13-16 (2005).
126. V. Fock, *Zeitschrift für Physik* **61** (1-2), 126-148 (1930).
127. J. C. Slater, *Physical Review* **36** (1), 57-64 (1930).
128. E. H. Lieb, *Physical Review Letters* **46** (7), 457-459 (1981).
129. R. G. Parr and W. T. Yang, *Journal of the American Chemical Society* **106** (14), 4049-4050 (1984).
130. R. G. Parr, *Density-functional theory of atoms and molecules*. (New York ; Oxford : Oxford University Press ; Oxford : Clarendon Press, New York ; Oxford : Oxford, 1989).
131. K. Capelle, *A Bird's-Eye View of Density-Functional Theory*. (2002).
132. A. Nagy, *Journal of Physics B-Atomic Molecular and Optical Physics* **24** (22), 4691-4694 (1991).
133. A. Nagy, *Journal of Physics B-Atomic Molecular and Optical Physics* **26** (1), 43-48 (1993).
134. A. Nagy and I. Andrejkovics, *Journal of Physics B-Atomic Molecular and Optical Physics* **27** (2), 233-240 (1994).
135. M. Born and R. Oppenheimer, *Annalen der Physik* **389** (20), 457-484 (1927).
136. P. A. M. Dirac, *Proc. Cambridge Philos. Soc.* **26**, 376 (1930).
137. J. P. Perdew and Y. Wang, *Phys Rev B Condens Matter* **45** (23), 13244-13249 (1992).
138. J. P. Perdew, K. Burke and M. Ernzerhof, *Physical Review Letters* **77** (18), 3865-3868 (1996).
139. J. P. Perdew, J. A. Chevary, S. H. Vosko, K. A. Jackson, M. R. Pederson, D. J. Singh and C. Fiolhais, *Phys Rev B Condens Matter* **48** (7), 4978 (1993).
140. R. Atta-Fynn and A. K. Ray, *Chemical Physics Letters* **482** (4-6), 223-227 (2009).

141. M. Ernzerhof and G. E. Scuseria, *The Journal of Chemical Physics* **110** (11), 5029 (1999).
142. A. D. Becke, *The Journal of Chemical Physics* **98** (7), 5648 (1993).
143. P. Blaha, K. Schwarz, G. H. K. Madsen, D. Kvasnicka and J. Luitz, (2001).
144. J. Slater, *Physical Review* **51** (10), 846-851 (1937).
145. O. K. Andersen, *Physical Review B* **12** (8), 3060-3083 (1975).
146. D. Singh, *Phys Rev B Condens Matter* **43** (8), 6388-6392 (1991).
147. G. K. H. Madsen, P. Blaha, K. Schwarz, E. Sjostedt and L. Nordstrom, *Physical Review B* **64** (19), art. no.-195134 (2001).
148. A. H. Macdonald, W. E. Pickett and D. D. Koelling, *Journal of Physics C-Solid State Physics* **13** (14), 2675-2683 (1980).
149. P. Novák, J. Kuneš, L. Chaput and W. E. Pickett, *physica status solidi (b)* **243** (3), 563-572 (2006).
150. F. Tran, P. Blaha, K. Schwarz and P. Novak, *Physical Review B* **74** (15), 155108 (2006).
151. M. Idiri, T. Le Bihan, S. Heathman and J. Rebizant, *Physical Review B* **70** (1), 014113 (2004).
152. K. Momma and F. Izumi, *Journal of Applied Crystallography* **41** (3), 653-658 (2008).
153. P. W. Tasker, *Journal of Physics C: Solid State Physics* **12** (22), 4977-4984 (1979).
154. J. C. Boettger, *Phys Rev B Condens Matter* **53** (19), 13133-13137 (1996).
155. J. G. Gay, J. R. Smith, R. Richter, F. J. Arlinghaus and R. H. Wagoner, *Journal of Vacuum Science & Technology A: Vacuum, Surfaces, and Films* **2** (2), 931-932 (1984).

156. V. Fiorentini and M. Methfessel, *Journal of Physics: Condensed Matter* **10** (4), 895 (1998).

## Biographical Information

Megan Hoover graduated in 2010 with a Bachelor's degree in Mathematics at the University of Texas at Arlington. The summer before graduation she did research on the Exact Solutions to the Camassa-Holm equation, mentored by Dr. Tuncay Aktosun. Megan started work with Dr. Asok Ray in 2011 for his Theoretical Condensed Matter Group. Her work in actinide oxides opened up a new passion in the study of nuclear energy and nuclear waste storage. It was not till the latter portion of her Master's thesis work that she realized the passion in this research area. Currently, she has a paper under review with Journal of Nuclear Materials for the research done with Dr. Raymond Atta-Fynn and Dr. Asok Ray titled "Surface properties of uranium dioxide from first principles." Her work in atomic oxygen adsorption is still ongoing, but she plans to continue the research and submit that work as well. As for the future, she hopes to continue doing research within the area of nuclear energy and/or nuclear waste storage. Sometime down the road she plans to go into Nuclear Energy Policy. Megan realizes the importance to educate people in the pros and cons of nuclear energy and make sure the right policies are in place for future generations.